Partially Premixed Combustion in Counterflow Flame and Dual Fuel Compression Ignition Engine

BY

XIAO FU
B.S., Tsinghua University, 2008

THESIS

Submitted as partial fulfillment of the requirements
for the degree of Doctor of Philosophy in Mechanical Engineering
in the Graduate College of the
University of Illinois at Chicago, 2015

Chicago, Illinois

Defense Committee:

Suresh Aggarwal,	Chair and Advisor
Kenneth Brezinsky,	Mechanical Engineering
Farzad Mashayek,	Mechanical Engineering
Sibendu Som,	Argonne National Laboratory
Peter Kelly Senecal,	Convergent Science, Inc

ACKNOWLEDGEMENTS

I want to give special thanks to my current advisor, Dr. Aggarwal, and previous advisor, Dr. Brezinsky. They have trained and taught me so well and opened my mind in various aspects. I would like to thank my thesis committee members, Dr. Mashayek, Dr. Som and Dr. Senecal for their kind support and assistance. Their guidance in all the research and academic activities that helped me progress to my research goals and explore the beauty of science in the process is valuable. I would also like to acknowledge my wonderful lab-mates, Xu Han, Cesare D'Ippolito, Saurabh Sharma, Abhijeet-Sanjay Badhe, Ramsey Basman Ibrahim, Amir Salarifard, Prithviraj Sabnis, Daniele Bongiovanni, Salvo Quattrocchi, Miroslaw Liszka, Dongru Li, Jon Komperda, Konrad Kuc, Mohsen Mohammed, Michelle Sentevski, Dr. Brad Culbertson, Arun Sebastian, Dylan Lawson, Dr. Hwansoo Chong, Alex Fridlyand, Dr. Stephen Garner, Dr. Soumya Gudiyela, Dr. Andrea Comandini, and Dr. Tomasz Malewicki. They have been always kind and helpful to me in the process of conducting research, learning materials and discuss science and technology. I also want to thank these very intelligent people, Dr. Daniel Lee, Dr. Jon Povich, Dr. Inkant Awasthi and Dr. Sameera Wijeyakulasuriya from Convergent Science, Inc. for providing technical support to me during all these years in a timely manner. I also enjoyed the internship and guest graduate research experience at Argonne National Lab and would like to thank Dr. Kyeong Lee, Dr. Hee Je Seong, Dr. Seungmok Choi, Dr. Hoon Lee, Dr. Sibendu Som, Zihan Wang and Dr. Yuanjiang Pei for their guidance on various of topic on the combustion research. Last but not the least, I want to thank my family for their understanding and support during my Ph.D study.

CONTRIBUTION OF AUTHORS

Chapter 1 is a literature review that places my dissertation topic in the context of the larger field and highlights the significance of my research. Chapter 2 covers the numerical methods used in this research. Chemkin and Converge are used in this work. The theory of these two simulation software are primarily summarized based on their theory manuals (Chemkin Theory Manual (CK-THE-10113-1209-UG-1 September 2012) and Converge TM 2.2.0 Theory Manual). Chapter 3 summarizes the validation of the computational models against experiments. I am the main contributor to the simulation work under the guidance of my advisor, Prof. Aggarwal. The experimental works are adopted from various published paper as cited. Chapter 4 represents two published manuscripts (Xiao Fu, Xu Han, Kenneth Brezinsky, Suresh Aggarwal, Effect of Fuel Molecular Structure and Premixing on Soot Emissions from n-Heptane and 1-Heptene Flames, Energy Fuels, 2013, 27 (10), pp 6262–6272, DOI: 10.1021/ef401409r; and Xiao Fu, Stephen Garner, Suresh Aggarwal, Kenneth Brezinsky, Numerical Study of NO_x Emissions from n-Heptane and 1-Heptene Counterflow Flames, Energy Fuels, 2012, 26 (2), pp 879–888, DOI: 10.1021/ef2014315) for which I was the first author. I generated all the results in both publications. My research mentor, Prof. Aggarwal played a large role in the writing of both the papers. Mr. Xu Han also helped a lot in writing the manuscript. Prof. Brezinsky and Dr. Garner provided valuable insights and idea to the research. Chapter 5 represents a published manuscript (Xiao Fu, Suresh Aggarwal, Fuel unsaturation effects on NO_x and PAH formation in spray flames, Fuel, 2015, 160, 1-15, DOI: 10.1016/j.fuel.2015.07.075) for which I was the first author. My research advisor contributed a lot in writing the manuscript. The first part of Chapter 6 represents a published work (Xiao Fu, Suresh Aggarwal, Two-stage ignition and NTC phenomenon in diesel engines, Fuel, 2015, 144, 188-196, DOI: 10.1016/j.fuel.2014.12.059) in

which I was the first author. The second part in Chapter 6 discussed about diesel/CNG dual fuel engine operation. I anticipate that this research will be published as a first authored manuscript in near future. In Chapter 7, it concludes my hypothesis and the research findings in this dissertation. The future directions of this field are discussed.

TABLE OF CONTENTS

TABLE OF CONTENTS (continued)

LIST OF TABLES

LIST OF FIGURES

LIST OF FIGURES (continued)

FIGURE PAGE

LIST OF FIGURES (continued)

FIGURE PAGE

LIST OF FIGURES (continued)

FIGURE PAGE

LIST OF FIGURES (continued)

FIGURE PAGE

LIST OF FIGURES (continued)

FIGURE PAGE

LIST OF ABBREVIATIONS

ATDC	After Top Dead Center
CNG	Compressed Natural Gas
CI	Compression Ignition
CFD	Computational Fluid Dynamics
ϕ	Equivalence Ratio
HCCI	Homogeneous Charge Compression Ignition
τ_{ig}	Ignition Delay
ICE	Internal Combustion Engine
LPZ	Lean Premixed Zone
LOL	Lift-off Length
MEP	Mean Effective Pressure
NO_x	Nitrogen Oxide
NPZ	Non-Premixed Zone
PM	Particulate Matter
PM	Particulate Matter
PAH	Polycyclic aromatic hydrocarbons
RPZ	Rich Premixed Zone
SOI	Start Of Injection
UHC	Unburned Hydrocarbon

SUMMARY

The overall objective of this research is to examine strategies for reducing NO_x and soot emissions in diesel engine. The thesis has two parts. In the first part, the effect of unsaturation or the presence of a double bond in the fuel molecular structure on NO_x and soot formation is investigated. Simulations have been performed for partially premixed flames burning n-heptane and 1-heptene fuels in a counterflow configuration and a constant volume diesel combustion vessel to examine the effect of unsaturation at different level of partial premixing and strain rate. A validated detailed kinetic model with 198 species and 4932 reactions has been used in the counterflow flame simulations. Results indicate that the presence of unsaturated bond leads to increased formation of acetylene and propargyl through β scission reactions, resulting in higher prompt NO, PAH and soot in 1-heptene flames than in n-heptane flames. Since these results are obtained in laminar flames, the study is extended to examine the effect of double bond in spray flames at diesel engine conditions. 3-D simulations are performed using CFD code (CONVERGE) to examine the structure and emission characteristics of n-heptane and 1-heptene spray flames in a constant-volume combustion vessel. The directed relation graph methodology is used to develop a reduced mechanism (207 species and 4094 reactions) starting from the detailed mechanism (482 species and 19072 reactions). Results indicate that the combustion under diesel engine conditions is characterized by a double-flame structure with a rich premixed reaction zone (RPZ) near the flame stabilization region and a non-premixed reaction zone (NPZ) further downstream. Most of NO_x is formed via thermal NO route in the NPZ, while PAH species are mainly formed in the RPZ. The presence of a double bond results in β scission reactions, leading to higher temperature and consequently higher NO in 1-heptene flame than that in n-heptane flame. It also leads to a significantly higher PAH species, implying increased soot

emission in 1-heptene flame than that in n-heptane flame. Reaction path analysis indicated that this is due to significantly higher amounts of 1,3-butadiene and allene formed from β scission reactions due to the presence of double bond.

In the second part of this research, a dual-fuel strategy for reducing emissions in a diesel engine has been examined. N-heptane and methane have been used as surrogates for diesel (pilot fuel) and natural gas (main fuel), respectively. The physical and chemical processes of dual-fuel combustion are simulated using CONVERGE and a reduced reaction mechanism (42 species, 168 reactions). The mechanism is validated against the experimental data for ignition and flame speed at engine relevant conditions. In engine simulations, methane is premixed with air during the intake, and then ignited by the n-heptane pilot injection. The heat release for the single-fuel case involves a hybrid combustion mode, characterized by rich premixed combustion and diffusion combustion, whereas for the dual-fuel combustion cases it also involves lean premixed combustion with a propagating flame. In addition, simulations focus on the effect of injection timing and the amount of n-heptane injection on the ignition, combustion and emissions in diesel engine. The minimum amount of n-heptane in terms of fractional energy required to ignite the methane/air mixture is analyzed at medium and high engine load conditions. The optimum injection timing is also determined considering engine thermal efficiency and soot/NO_x emissions by sweeping through a range of start of injections (SOI) for each engine load and n-heptane injection quantity. The effects of SOI and the amount of n-heptane on emissions are analyzed. Results indicate high UHC emissions due to unburned methane in the crevice region at medium load, and high CO emissions in the n-heptane spray region at high load. The present results can provide guidaselines for the dual-fuel engine development.

1 INTRODUCTION

1.1 MOTIVATION

Conventional liquid fossil fuels have been utilized for decades as the major energy sources for transportation. Though the traditional diesel and gasoline engines have been proven practical and efficient, the sustainability of diesel and gasoline fuels and regulations on the emission of particulate matter (PM), nitrogen oxides (NO_x) and greenhouse gases (GHG, mainly CO_2) have become increasingly more challenging. There is a clear need to utilize alternative fuels in order to reduce the dependence on crude oil. However, due to the relative low cost, high durability and power density, the reciprocating internal combustion engine (ICE) will still remain the dominant choice of motor for light-duty vehicles for the foreseeable future. Thus, it is important to pursue research and development efforts to provide a better understanding of the fundamental processes affecting engine efficiency and emissions[1]. In this context, current engine research has focused on two aspects, developing alternative fuels and investigating new combustion strategies in engines.

1.1.1 Unsaturation in Alternative Fuels

During the last decade, there has been significant effort on finding alternatives to the traditional fuels. In this context, two promising alternative fuels are the bio-fuels and natural gas. Bio-fuels can be further categorized into biodiesel fuels and syngas. Biodiesel fuels, which are produced via the esterification process, have been proven to represent a cleaner alternative to conventional diesel[2]. Esterification using methanol (or ethanol) in the presence of an acid or a base catalyst can convert the vegetable oil such as canola, coconut, palm, peanut, soy and rapeseed oil into methyl esters, which are characterized by a wide range of chemical composition and properties. Consequently, these fuels have significantly different atomization, combustion and emission

characteristics compared to diesel[3]. In general, there is a reduction in PM, unburned hydrocarbon and CO from the of biodiesel combustion compared to those from conventional diesel[4]. However, a number of studies have observed noticeable increase in NO_x with biodiesels compared to diesel depending upon engine load, fuel, and diesel-biodiesel blending ratios[4,5,6,7,8]. A correlation between the formation of NO_x and the iodine number, which is a measure of the degree of unsaturation, has been observed. It has been suggested that the increased NO_x production is due to the chemical consequences and not simply the physical effects of the double bonds in higher iodine number biodiesel fuels[9]. Moreover, most biodiesel chemical compounds contain one or more unsaturated C=C bonds, which can have strong influence on the formation of PM due to the presence and number of double bonds in the fuel molecular structure [10,11,12,13,14].

Since bio-diesels are blends of several components, previous studies have utilized different surrogates for examining their combustion and emission characteristics. Studies dealing with short chain biodiesel surrogates, such as methyl butyrate and methyl butenoate, indicated that the saturated hydrocarbon, ethane, produces more NO_x than does the ethylene, implying that short chain biodiesel fuels may not be a good choice to study the reason of increased NO_x from unsaturated fuels[15,16,17,18]. Long change hydrocarbons such as n-heptane and 1-heptene have been examined in shock tube pyrolysis experiments as the saturated and unsaturated hydrocarbon side chains of C_8 methyl esters by Garner et al. Results have shown increased acetylene (C_2H_2) production from 1-heptene compared to n-heptane over intermediate temperature[19]. Acetylene provides major routes for NO formation through prompt NO mechanisms within intermediate temperature regime (1100-1600K)[16,20] and soot formation through H-abstraction-C_2H_2-addition (HACA) mechanism[21,22]. With this background, it is important to analyze the effect of fuel molecular structure on emission characteristics using n-heptane and 1-heptene as the surrogates of

saturated and unsaturated bio-diesel side chains in flame environment. This is one major motivation for this research.

1.1.2 Diesel NG Dual-Fuel Combustion

There is considerable interest in using natural gas (NG) because of its abundant supply and economical and environmental advantages. NG has a high octane number and thus has been used in spark-ignited (SI) engines. But since the NG displaces air in the cylinder, NG engines have less peak power than gasoline engines. A better approach utilizing NG is through ignition assistant in compression ignition engines and is becoming more accepted recently. The ignition assistant system is necessary for NG utilized in compression ignition engines because the cetane number of NG is zero, which means impossible to compress ignite. Generally two ignition assistant approaches have been examined, spark assisted and pilot fuel assisted. The spark assisted NG engine has been proven practical[23,24,25] but has not received much attention due to difficulties in diesel engines modifications. The viability of a dual-fuel strategy using blends of various liquid and gaseous fuels has been examined by numerous researchers. Such blends include bio/petroleum[26], H_2-gasoline[27], H_2-NG[28,29,30,31,32,33], H_2-CH_4[34,35], H_2-diesel[36] and syngas-diesel[37,38]. The use of NG and biogas in dual-fuel mode has also been investigated using CI[39,40], and HCCI[41] engines.

For diesel-NG dual-fuel engines, a gaseous fuel-air mixture is introduced through the intake valve, while diesel is injected and compression ignited. The effects of various parameters, such as fuel composition, blending ratio, injection timing, EGR, and gaseous fuel-air ratio have been characterized at different loads. While a number of aspects have been examined[42,43,44,45], a common observation is that a dual-fuel strategy at high loads leads to lower PM, CO_2, and VOC (volatile organic compounds) emissions while maintaining thermal efficiency, but higher CO and

UHC emissions compared to single diesel fuel. However, the benefits of dual-fuel operation become less clear at low loads, and issues concerning reduced engine power and higher UHC emission need to be addressed by optimizing other parameters, i.e., injection timing, EGR, amount of liquid (pilot) fuel injected, gaseous fuel-air equivalence ratio[46,47,48], etc. Our literature review indicates extensive experimental research dealing with dual-fuel (diesel-NG) CI engines. However, relatively few computational studies have been reported on this topic[49,44]. In particular, details of the two-stage ignition, combustion modes, and emission characteristics in dual-fuel engines have not been investigated. For instance, the heat release in a diesel engine generally goes through a hybrid combustion mode, involving rich premixed combustion, followed by diffusion combustion[50,51]. In contrast, depending upon the load and other conditions, the heat release in a dual-fuel engine involves a lean combustion mode with a propagating flame[38]. With this motivation, the present research also aims to perform a fundamental investigation on the effect of using dual fuels on the ignition, combustion, and emissions characteristics in a diesel engine.

1.1.3 Partially Premixed Combustion

The combustion behavior in a dual fuel engine is significantly different compared to that in a single fuel CI engine. Typically, the diesel engine combustion can be summarized through Figure 1, describing the "conceptual model" of Dec[50] based on laser-sheet imaging and optical data. The cold liquid fuel jet and a rich fuel vapor/air mixture produce a fuel-rich premixed flame (thin, light blue layer), while a diffusion flame (thin orange layer) occurs between products from rich premixed zone (RPZ) and ambient air. The combustion products from RPZ such as CO and H2 are consumed in the diffusion flame or non-premixed zone (NPZ). Large amount of NO_x is generated through thermo NO route due to the high temperature in this zone. This combustion model provides a good reference to qualitatively examine the combustion process of diesel spray.

The detailed structure of this PPF and its emission characteristics strongly depend upon the partial premixing level, i.e., the fuel-air mixing level within the RPZ because most PM and prompt NO are generated in this region. However, PPF in engine is coupled with liquid fuel atomization and vaporization, temporal and spatial inhomogeneities, cylinder gas motions and turbulence, therefore a fundamental understanding on the PPF itself as well as these couplings are necessary. The counterflow flame configuration is commonly used to study the diesel surrogate (n-heptane) PPF. A schematic is shown in Figure 2. It consists of two opposing jets issuing from two coaxial nozzles that are placed one above the other. A rich fuel-air mixture flows from the lower nozzle and air from the upper nozzle. This configuration provides a practical way to analyze the combustion in both RPZ and NPZ without considering the complex physical phenomena.

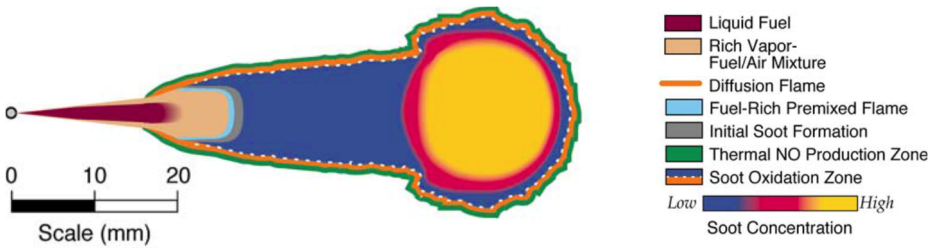

Figure 1. The schematic of conceptual combustion model from Dec[50].

In a dual fuel engine, depending on how the gaseous fuel is introduced, the dominant combustion modes may be significantly modified. A common way to introduce the gaseous fuel is to place one or more gas (NG) injectors in the intake manifold close to the intake ports and let NG and air premix during the intake stroke. Therefore, when the pilot fuel is injected, the gas inside the cylinder is a lean NG/air mixture. Consequently, in addition to RPZ and NPZ, the heat

release may also involve a lean premixed combustion zone (LPZ), when the NG/air mixture is ignited by the pilot fuel.

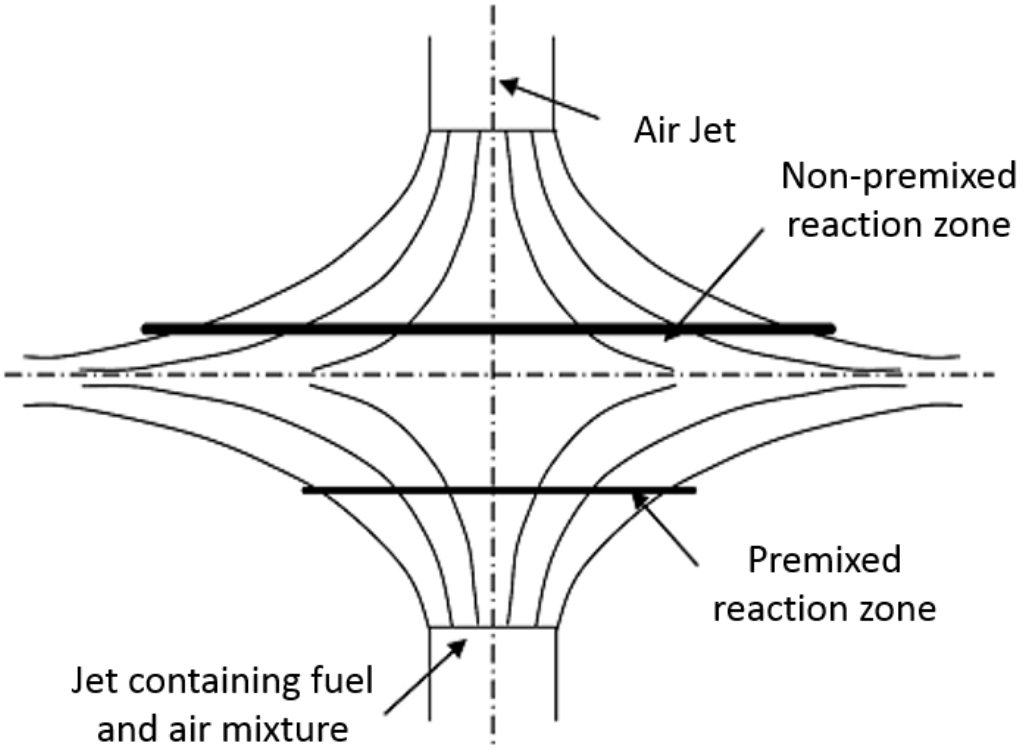

Figure 2. The schematic of the counterflow partially premixed flame configuration.

1.2 OBJECTIVES

Two objectives are proposed based on the above considerations. The first objective is to employ a realistic flame environment and examine the hypothesis that the oxidation of unsaturated long chain hydrocarbons results in increased acetylene and propargyl, and consequently, increased NO, PAH and soot formation. The second objective is to analyze how natural gas affects the diesel spray combustion thus results in changes in engine raw emissions from a diesel/NG dual-fuel engine. Numerical calculations are performed in both partially premixed flame and compression ignition (CI) engine using n-heptane, 1-heptene and methane as the fuels.

The numerical investigation is divided into two sections, as summarized below.

1.2.1 Counterflow Flame Simulations

The partially premixed flame simulations have been performed in an opposed jet flow configuration because of its simple flow field and its relevance to diesel engine combustion. 1-D Opposed Flow Flame model (Oppdif) provided in CHEMKIN software package has been utilized in the first section. Detailed chemistry mechanism (197 species and 4931 reactions) developed by Ranzi et al. at Politecnico di Milano is used for the fuel oxidation, NO formation and PAH formation. N-heptane and 1-heptene are used as the fuels to represent the hydrocarbon side chains of the saturated and unsaturated methyl esters, namely methyl octanoate and methyl trans-2-octenoate.

The detailed structures of the diffusion flame and partially premixed flame burning n-heptane and 1-heptene have been examined to understand the combustion and emission processes. A parametric study has been performed by varying strain rate and partial premixing level for both the fuels. Through these comparisons, the effect of fuel molecular structure is identified. The chemical consequences of the double bond to the increased NO and PAH formation are discussed. Contributions of the various NO formation routes, such as thermal, prompt, intermediate N_2O and NNH routes, to the total NO formation are also characterized.

1.2.2 Diesel Spray Combustion Simulations

The simulations of the combustion of diesel spray is always challenging due to the need to consider many physical and chemical phenomena, such as spray breakup, droplet dynamics and atomization, vaporization, burning chemistry and turbulence, as well as the interaction among all these phenomena. In the second part of this research, a 3D CFD code, CONVERGE is used to model the physical-chemical interaction process in a CI engine. A reduce chemistry mechanism

developed at Chalmers University of Technology (42 species, 168 reactions) is used. Extensive validations of the mechanism and the code using the data available from other research facilities are performed. The predicted liquid and vapor penetration distance for non-reacting n-heptane spray and the ignition delay (τ_{ig}) and flame lift off length (LOL) for reacting n-heptane sprays have been compared with the experimental data provided by Sandia National Laboratory. Engine simulation result for a light duty GM diesel engine has been validated against the data from Argonne National Laboratory.

In dual-fuel engine simulation, methane is introduced in the intake manifold. N-heptane is injected into the cylinder as the pilot fuel to ignite the methane air mixture. Single fuel case and dual-fuel cases are set up based on these configurations. Effects of the presence of methane on the ignition, combustion and emissions have been analyzed. Results confirm the presence of a lean partially premixed combustion zone burning methane besides the rich combustion zone burning n-heptane and diffusion zone burning the products from rich zone. NO, soot and UHC emissions from the engine are compared for various methane - n-heptane blending cases.

To verify the conclusion of the first section regarding the effect of double bond on emissions, n-heptane and 1-heptene spray flames are simulated in a constant-volume combustion vessel at diesel engine conditions using the CFD code (CONVERGE). A more detailed mechanism, which considers 1-heptene oxidation and various NO PAH formation routes, is validated and utilized. Detailed flame structures and NO_x and PAH formation processes in these flames are analyzed.

2 NUMERICAL MODEL AND VALIDATION

For this section, three parts will be discussed. Chemistry mechanism for the fuel oxidation, NO_x formation, and soot formation is very important in combustion simulations. Therefore, the chemistry mechanisms are discussed at the beginning. Then a brief introduction of the counterflow flame code are presented, followed by the models and validations of the CONVERGE code.

2.1 COUNTERFLOW FLAME SIMULATION

Simulations are performed using the Oppdif in CHEMKIN packages[52,53]. "Oppdif is a Fortran program that computes the diffusion flame between two opposing nozzles. A similarity transformation reduces the two-dimensional axisymmetric flow field to a one-dimensional problem. Assuming that the radial component of velocity is linear in radius, the dependent variables become functions of the axial direction only. Oppdif solves for the temperature, species mass fractions, axial and radial velocity components, and radial pressure gradient, which is an eigenvalue in the problem."[52]

The governing equations for the fluid dynamics of counter-flow flame are presented as followed. At steady sate, the mass conservation equation in cylindrical coordinate can be written as:

$$\frac{\partial(\rho u)}{\partial x}+\frac{1}{r}\frac{\partial(\rho v_r r)}{\partial r}=0 \qquad (1)$$

where ρ, u, v_r, x, and r are the density of the gas, axial velocity, radial velocity, axial position, and radial position. According to von Karman, it can be assumed that ρ and v_r/r are both independent of the radial position r. Thus, if we define

$$G(x) = -\frac{(\rho v_r)}{r}, F(x) = \frac{\rho u}{2} \tag{2}$$

Then the following equation can be obtained:

$$G(x) = \frac{dF(x)}{dx} \tag{3}$$

If we also define

$$H = \frac{1}{r}\frac{\partial p}{\partial r} \tag{4}$$

the momentum conservation equation can be written as:

$$H - (n-1)\frac{d}{dx}\left(\frac{FG}{\rho}\right) + \frac{nG^2}{\rho} + \frac{d}{dx}\left[\mu\frac{d}{dx}\left(\frac{G}{\rho}\right)\right] = 0 \tag{5}$$

Similarly, the energy conservation equation is

$$\rho u\frac{dT}{dx} - \frac{1}{c_p}\frac{d}{dx}\left(\lambda\frac{dT}{dx}\right) + \frac{\rho}{c_p}\sum_k c_{p,k}Y_k V_k\frac{dT}{dx} + \frac{1}{c_p}\sum_k h_k\dot{\omega}_k + \frac{1}{c_p}\dot{Q}_{rad} = 0 \tag{6}$$

where Y, c_p, h, $\dot{\omega}$, V, and $\dot{Q}_{rad}$ are the mass fraction, specific heat, absolute enthalpy, species production rate, diffusivity, and heat loss due to radiation.

Also, the species conservation equation is

$$\rho u\frac{dY_k}{dx} + \frac{d}{dx}(\rho Y_k V_k) - \dot{\omega}_k W_k = 0 \qquad k = 1,...,K \tag{7}$$

"The Twopnt software solves the two-point boundary value problem for the steady-state form of the discretized equations."[52] For the 1D simulation along the center axis, the boundary conditions can be expressed as

$$x = 0: \quad F = \frac{\rho_F u_F}{2}, \; G = 0, \; T = T_F, \; \rho u Y_k + \rho Y_k V_k = (\rho u Y_k)_F \tag{8}$$

$$x = L: \quad F = \frac{\rho_O u_O}{2}, \; G = 0, \; T = T_O, \; \rho u Y_k + \rho Y_k V_k = (\rho u Y_k)_O \tag{9}$$

where subscript F and O represents the fuel nozzle and oxidizer nozzle in the diffusion flame case, respectively. The variables c_p, μ, $\dot{\omega}$, V, and $\dot{Q}_{rad}$ are obtained by thermodynamic data and transport data. Thermodynamic data is supplied for each species in the chemistry system such as species' name, its elemental composition, its electronic charge, an indication of its phase and fourteen polynomial fitting coefficients to calculate species enthalpy, entropy, and specific heat capacity.

The CHEMKIN package evaluates chemical reaction rates, thermodynamic properties and transport properties provided through the mechanism. Mixture averaged formulation for the diffusivity V is used:

$$V_k = -\frac{1}{X_k} D_{km} \frac{dX_k}{dx} - \frac{D_k^T}{\rho Y_k} \frac{1}{T} \frac{dT}{dx} \tag{10}$$

where

$$D_{km} = \frac{1 - Y_k}{\sum_{j \neq k}^{K} \frac{X_j}{D_{jk}}} \tag{11}$$

D_{km}, D_{jk}, and D_k^T are the mixture-averaged, binary, and thermal diffusion coefficients, respectively. In this research, the thermal diffusion is neglected.

The reaction rate is expressed by

$$\omega_k = \sum_{i=1}^{I} v_{ki} q_i \quad (k = 1,...K) \tag{12}$$

where

$$\begin{aligned} v_{ki} &= v''_{ki} - v'_{ki} \\ q_i &= k_{fi} \prod_{k=1}^{K} [X_k]^{v'_{ki}} - k_{ri} \prod_{k=1}^{K} [X_k]^{v''_{ki}} \end{aligned} \tag{13}$$

k_f and k_r are the forward reaction rate and reverse reaction rate of a reaction, respectively. The rate constants k_f for forward reactions are assumed to have the following Arrhenius temperature dependence:

$$k_{fi} = A_i T^{\beta_i} \exp\left(\frac{-E_i}{R_c T}\right) \tag{14}$$

where the pre-exponential factor A, the temperature exponent β, and the activation energy E are specified through gas-phase kinetics data for each reaction. Reversed reaction rate constant can be calculated using the following equation:

$$k_{ri} = \frac{k_{fi}}{K_{ci}} \tag{15}$$

where K_{ci} is the equilibrium constant of the reaction in concentration units, and can be determined more easily from the thermodynamic properties in pressure units:

$$K_{ci} = K_{pi} \left(\frac{P}{RT}\right)^{\sum_{k=1}^{K} v_{ki}} \tag{16}$$

The equilibrium constants K_{pi} are obtained with the relationship:

$$K_{pi} = \exp\left(\frac{\Delta S_i^0}{R} - \frac{\Delta H_i^0}{RT}\right) \quad (17)$$

The Δ refers to the change that occurs in passing completely from reactants to products in the i th reaction. ΔS_i^0 is the total entropy change through the reaction, and ΔH_i^0 is the total enthalpy change through the reaction. Molar entropy and enthalpy of species can be achieved from the thermodynamic properties.

In order to establish a grid independence, solutions are obtained on increasingly finer grids, and by changing GRAD and CURV parameters, until no variation is observed between two grid systems. The kinetic mechanism used to model n-heptane and 1-heptene flames will be discussed in Section 2.3 [71,72].

2.2 3D CFD SIMULATIONS USING CONVERGE

The simulations of the combustion of diesel spray is always challenging since it should consider many physical and chemical phenomena, such as fuel injection, spray breakup, droplet dynamics and atomization, vaporization, ignition and burning chemistry, turbulence, heat transfer by convection and radiation, as well as the interaction among all these phenomena. The current status of CPU speed and model development have made multi-dimensional diesel spray simulations a possible tool to understand the complex combustion and emissions processes that occur in engines. In the second part of the thesis, the simulations are performed using a commercially available CFD code called CONVERGE [54, 55] to model the physical-chemical interaction process in a CI engine. The CONVERGE software incorporates several models for turbulence, spray injection, atomization and breakup, droplet collision and coalescence, and vaporization.

The 3D computational model is based on an Eulerian-Lagrangian formulation for the two-phase turbulent reacting flow in the engine. The simulation uses finite volume to solve the gas-phase governing partial differential equations on the Eulerian grid including velocity, temperature or internal energy, gas pressure, species concentrations and turbulence kinetic energy. The Eulerian phase is described using the Navier-Stokes equations and the k-ε turbulence model. "The length and time scales associated with the spray processes are too small to be resolved computationally, necessitating the use of sub-grid scale models to describe the spray physics. The spray is represented by a stochastic system of a discrete number of parcels, which are tracked computationally using a Lagrangian scheme. The two phases are coupled through the mass, momentum, and energy exchange terms, which are present in both the liquid- and gas-phase equations. Liquid-gas coupling is performed using the nearest node approach."[56]

With this general background of the 3D CFD modeling approach, the governing equations are presented as follows.

2.2.1 Governing Equations

The fluid dynamics are governed by equations that calculate the conservation of mass, momentum, and energy. To derive the Reynolds Averaged Navier-Stokes (RANS) transport equations and averaging, the RANS decomposition is substituted into the Navier-Stokes equations. The compressible RANS equations for mass and momentum transport are given by:

$$\frac{\partial \overline{\rho}}{\partial t} + \frac{\partial \rho \widetilde{u}_j}{\partial x_j} = S \tag{18}$$

and

$$\frac{\partial \bar{\rho}\tilde{u}_i}{\partial t} + \frac{\partial}{\partial x_j}\left(\bar{\rho}\tilde{u}_i\tilde{u}_j\right) = -\frac{\partial \bar{p}}{\partial x_i} + \frac{\partial}{\partial x_j}\left[\bar{\sigma}_{ji} - \bar{\rho}\widetilde{u_i''u_j''}\right] + F_s + \bar{\rho}g \tag{19}$$

where the Favre averaged, ~, is defined for velocity as:

$$\tilde{u} = \frac{\int_T \rho u dt}{\int_T \rho dt} = \frac{\overline{\rho u}}{\bar{\rho}}$$

and

$$\bar{\sigma}_{ij} = \mu\left(\frac{\partial \tilde{u}_i}{\partial x_j} + \frac{\partial \tilde{u}_j}{\partial x_i}\right) - \frac{2}{3}\delta_{ij}\mu\frac{\partial \tilde{u}_k}{\partial x_k} \tag{20}$$

The species and energy equations can be derived as

$$\frac{\partial \bar{\rho}\tilde{Y}_m}{\partial t} + \frac{\partial \bar{\rho}\tilde{Y}_m\tilde{u}_j}{\partial x_j} = \frac{\partial}{\partial x_j}\left(\bar{\rho}D_m\frac{\partial \tilde{Y}_m}{\partial x_j} - \bar{\rho}\widetilde{Y_m''u_j''}\right) + \dot{\bar{\rho}}_{m,s} + \dot{\bar{\rho}}_{m,ch} \tag{21}$$

$$\begin{aligned}\frac{\partial \bar{\rho}\tilde{e}}{\partial t} + \frac{\partial \bar{\rho}\tilde{e}\tilde{u}_i}{\partial x_i} = -\bar{p}\frac{\partial \tilde{u}_i}{\partial x_i} + \tilde{\sigma}_{ij}\frac{\partial \tilde{u}_i}{\partial x_i} + \frac{\partial}{\partial x_i}\left(K\frac{\partial \tilde{T}}{\partial x_i} - \bar{\rho}\widetilde{e''u_i''}\right) + \\ \frac{\partial}{\partial x_i}\left(\bar{\rho}D\sum_m \bar{h}_m\frac{\partial \tilde{Y}_m}{\partial x_i} - \sum_m \bar{h}_m\bar{\rho}\widetilde{Y_m''u_i''}\right) + \dot{\bar{Q}}_{ch} + \dot{Q}_S\end{aligned} \tag{22}$$

In the above equations, u is velocity, ρ is density, S and S_i are the source terms, P is pressure, μ is viscosity, and t is the time. For the mass conservation equation, the source term may arise from evaporation process. For the momentum conservation equation, the source term is due to the force transmitted to the gas phase through droplet drag, body forces and momentum exchange due to evaporation. Note that the ensemble averaging of the equations introduces additional terms called the Reynolds stresses that represent the effects of turbulence. The Reynolds stress τ_{ij} is given by

$$\tau_{ij} = -\overline{\rho}\widetilde{u_i' u_j'}$$

$$\tau_{ij} = -\overline{\rho}\, u_i' u_j' \tag{23}$$

which is included in the last term on the right side of Equation (19). The Reynolds stress must be modeled to obtain closure for Equation (19). Traditionally, in RANS models, an effective turbulent viscosity is used to model the Reynolds stress term. Thus, the turbulent convective mixing is modeled by additional turbulent diffusion (i.e., diffusive mixing). The modeled Reynolds stress for the Standard k-ε and RNG models is given by

$$\tau_{ij} = -\overline{\rho}\widetilde{u_i' u_j'} = 2\mu_t S_{ij}\left(\rho k + \mu_t \frac{\partial \widetilde{u_i}}{\partial x_i}\right) \tag{24}$$

where the turbulent viscosity, μ_t , is given by

$$\mu_t = c_\mu \rho \frac{k^2}{\varepsilon} \tag{25}$$

k is the turbulent kinetic energy, which is defined by one half of the trace of the stress tensor, or

$$k = \frac{1}{2}\widetilde{u_i' u_j'} \tag{26}$$

c_μ is a model constant that can be tuned for a particular flow, and ε is the dissipation of turbulent kinetic energy. The mean strain rate tensor S_{ij} is given by

$$S_{ij} = \frac{1}{2}\left(\frac{\partial \widetilde{u}_i}{\partial x_j} + \frac{\partial \widetilde{u}_j}{\partial x_i}\right) \tag{27}$$

To account for the presence of turbulence in mass transport and energy transport, turbulent diffusion and turbulent conductivity terms are used. The turbulent diffusion and conductivity terms are given by

$$D_t = \left(\frac{1}{Sc_t}\right)\mu_t \ , \quad K_t = \left(\frac{1}{\mathrm{Pr}_t}\right)\mu_t c_p \tag{28}$$

where Sc_t is the turbulent Schmidt number, Pr_t is the turbulent Prandtl number, D_t is the turbulent diffusion, and K_t is the turbulent conductivity.

So the turbulent transport for diffusivity and conductivity can be expressed as

$$-\rho\widetilde{Y_m''u_i''} = \bar{\rho}D_{m,t}\frac{\partial \tilde{Y}_m}{\partial x_i}$$

$$-\bar{\rho}\widetilde{e''u_i''} = K_t\frac{\partial \tilde{T}}{\partial x_i}$$

The k transport equation is given by

$$\frac{\partial \rho k}{\partial t} + \frac{\partial \rho u_i k}{\partial x_i} = \tau_{ij}\frac{\partial u_i}{\partial x_j} + \frac{\partial}{\partial x_j}\frac{\mu}{\mathrm{Pr}_k}\frac{\partial k}{\partial x_j} - \rho\varepsilon + S_s \tag{29}$$

The Rapid Distortion RNG k-ε model uses the transport equation for ε given by

$$\begin{aligned}\frac{\partial \rho\varepsilon}{\partial t} + \frac{\partial\left(\rho u_i \varepsilon\right)}{\partial x_i} = \frac{\partial}{\partial x_j}\left(\frac{\mu}{\mathrm{Pr}_\varepsilon}\frac{\partial \varepsilon}{\partial x_j}\right) - \left[\frac{2}{3}c_{\varepsilon 1} - c_{\varepsilon 3} + \frac{2}{3}c_\mu c_\eta \frac{k}{\varepsilon}\frac{\partial u_k}{\partial x_k}\right]\rho\varepsilon\frac{\partial u_i}{\partial x_i} \\ + \left[\left(c_{\varepsilon 1} - c_\eta\right)\frac{\partial u_i}{\partial x_j}\tau_{ij}^* - c_{\varepsilon 2}\rho\varepsilon + c_s S_s\right]\frac{\varepsilon}{k}\end{aligned} \tag{30}$$

where

$$c_\eta = \frac{\eta\left(1-\eta/\eta_0\right)}{1+\beta\eta^3} \tag{31}$$

and

$$\tau_{ij}^* = \tau_{ij} - \frac{1}{3}\delta_{ij}\tau_{kk} = 2\mu_t\left(S_{ij} - \frac{1}{3}\delta_{ij}\frac{\partial u_k}{\partial x_k}\right) \tag{32}$$

The source term, S_s is included to account for the interactions of turbulence with the discrete phase. This term is modeled as

$$S_s = -\frac{\sum_p N_P\left(F'_{drag,i}u'_i\right)_p}{V} \tag{33}$$

This summation is carried out for all the parcels in a computational cell. Also V is the cell volume. N_p is the number of droplets in a parcel. u_i' is the fluctuating component of the gas-phase velocity, and $F_{drag,i}$ is the drag force.

Redlich-Kwong (RK) Equation of State is calculated as

$$P = \frac{RT}{v-b} - \frac{a}{v^2+bv}\ ,\quad b = \beta_{rk}v_c\ ,\quad a = \alpha_{rk}\frac{P_c v_c^2}{\sqrt{T_r}} \tag{34}$$

where v_c is the critical volume, T_c is the critical temperature, P_c is the critical pressure, $\alpha_{rk} = 0.42748$ represents the attractive forces between molecules and $\beta_{rk} = 0.08664$ represents the volume of the molecules.

More detail describing the turbulence modeling is included in the Appendix A.

2.2.2 Discrete Phase Modeling

To calculate the spray in a simulation, drop parcels are introduced into the domain at the injector location at a rate specified by the injection profile. Parcels represent a group of identical drops (i.e., same radius, velocity, temperature, etc.) and are used to statistically represent the entire spray field. Spray droplets are subject to several processes from the time of injection until the time of vaporization. Table 1 below is a summary of the main physical droplet processes that are considered in this study. Detailed descriptions are as followed.

Table 1. Summary of key spray processes used in the CFD code.

Physical Process	Spray Model
Liquid injection	Blob injection model, discharge coefficient model
Drop drag	Dynamic drop drag model
Spray breakup	Modified KH-RT model
Drop collision	NTC collision
Drop turbulent dispersion	TKE preserving model
Drop/wall interaction	Wall film model
Evaporation model	Multi-component vaporization

The injection process is simulated using a blob injection model. In blob injection model, injects liquid droplet parcels injected is considered to have a diameter equal to the effective nozzle diameter. To characterize the nozzle flow, the contraction effects of the nozzle in the injector are accounted, based on the user inputs for discharge coefficient (C_d), nozzle diameter, liquid density, injection rate shape, mass of injection and duration of injection. The velocity coefficient (C_v) is

dynamically calculated based on injection pressure to update the actual injection velocity. The area contraction coefficient (C_a) can be obtained from the relationship:

$$C_a = \frac{C_d}{C_v} \tag{35}$$

C_a is use to characterize cavitation. The area contraction coefficient is directly influenced by the amount of vapor presented near the nozzle exit.

A drop's velocity, v_i , is obtained from its equation of motion:

$$\rho_l V_d \frac{dv}{dt} = F_{d,i} \tag{36}$$

where ρ_l is the liquid density, V_d is the drop volume, and $F_{d,i}$ is given by the sum of the drag force and the gravitational body force as:

$$F_{d,i} = F_{drag,i} + F_{g,i} = C_D A_f \frac{\rho_g |U_i|}{2} U_i + \rho_l V_d g_i \tag{37}$$

$A_f = \pi r^2$ is the drop's frontal area, ρ_g is the gas density, U_i is the drop-gas relative velocity given by

$$U_i = u_i + u_i' - v_i \tag{38}$$

where u_i and u_i' are the local mean and turbulent fluctuating gas velocities, respectively, and g_i is the gravitational acceleration.

The drag coefficient, C_D , is important for spray modeling and two approaches are well explored and utilized: perfect spherical and dynamic drag accounting for the distortion of droplet. The later one is considered in this research. Under the assumption of a spherical droplet the drag coefficient C_D is determined as[57]:

$$C_{D,sphere} = 0.424 \qquad \mathrm{Re} > 1000$$
$$= \frac{24}{\mathrm{Re}}\left(1 + \frac{1}{6}\mathrm{Re}^{2/3}\right) \qquad \mathrm{Re} \le 1000 \tag{39}$$

where Re is the drop Reynolds number based on the drop's spherical diameter, the fluid phase density and laminar viscosity, and the relative velocity between the drop and the gas. Dynamic drag model[58] considers that "the drag coefficient is dependent on the shape of the droplet. An initially spherical shape of the droplet distorts significantly when the Weber number is large." The shape can vary between a sphere and a disk in two extreme cases. Drag coefficient for a sphere is significantly smaller than that for a disk. This dynamic drop model considers the effects of drop distortion. It accounts for linearly varying the drag between that of a disk and a sphere. Therefore, the dynamic drag coefficient can be calculated as

$$C_D = C_{D,sphere}\left(1 + 2.632y\right) \tag{40}$$

where y is the drop distortion factor, varies from 0 (sphere) to 1 (disk).

Next, the breakup process is calculated by using the Kelvin-Helmholtz (KH) and Rayleigh-Taylor (RT) instabilities[59] models. The Kelvin-Helmholtz instability[60] is a consequence of disturbances of the relative motion between the liquid and gas phases while the Rayleigh-Taylor instability is caused by the rapid deceleration of the drops the drag force. Figure 3 presents the spray break-up schematics. The liquid blobs are injected with a diameter equal to that of the injector nozzle. In addition, the KH breakup mechanism is applied to a droplet throughout its lifetime, while the RT mechanism is only initiated once the drop reaches a characteristic distance, L_b, from the injector. The model assumes that only KH instabilities are important for droplet breakup inside of L_b, while both KH and RT breakup mechanisms are used beyond the breakup length.

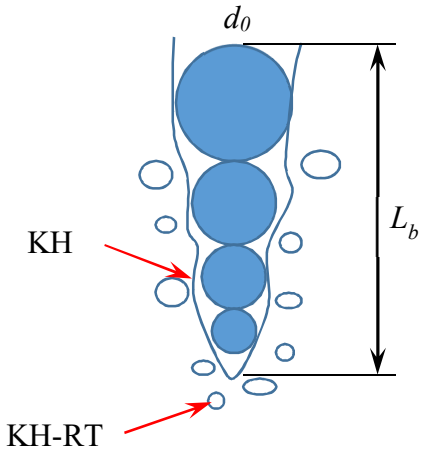

Figure 3. Schematic of the KH-RT spray breakup model.

Droplet collisions are based on the NTC (No Time Counter) algorithm[61], and the outcome of each collision is predicted as bouncing stretching, reflexive separation, or coalescence[62]. Direct Simulation Monte Carlo (DSMC) calculations which is used for gas dynamics employs the NTC method. The NTC method involves stochastic (randomly determined) sub-sampling of the parcels within each cell. This potentially results a very fast collision calculations. The NTC method is derived, without assumptions, from the basic probability model for stochastic collision. The basic probability model requires that the cell size is sufficiently small such that spatial variations in spray quantities can be neglected. The NTC method first sorts the parcels into groups that reside in the same cell. This requires only 2N operations, where N is the number of droplets in a cell. "Next, the NTC method picks a stochastic sub-sample from all of the possible pairs in a cell. The number of picked pairs does not affect the final average answer, as long as the number meets constraints derived in Schmidt and Rutland (2000). The probabilities for the sub-sample pairs are multiplied by the reciprocal of this fraction, increasing the probability of collision. Sampling is done with replacement so that multiple collisions for a pair can be correctly calculated. The resulting method

incurs a cost that is linearly proportional to the number of parcels, as opposed to the N-squared cost of many existing methods."[63]

The droplet evaporation model uses Chiang correlation[64]. Once the liquid spray is injected into the computational domain, a model is needed to convert the liquid into gaseous vapor. Chiang correlation is used to determine the time rate of change of droplet size:

$$\frac{dr_0}{dt} = -\frac{\rho_g D}{2\rho_l r_0} B_d Sh_d \left(Y_1^* - Y_1\right) \tag{41}$$

where D is the mass diffusivity of liquid vapor in air,

$$B_d = \frac{Y_1^* - Y_1}{1 - Y_1^*} \tag{42}$$

Y_1^* is the vapor mass fraction at the drop's surface, Y_1 is the vapor mass fraction, and Sh_D is the Sherwood number given by:

$$Sh_d = 1.224\left(1 + B_d\right)^{-0.568} \mathrm{Re}_d^{0.365}\, Sc_d^{0.492} \tag{43}$$

where

$$\mathrm{Re}_d = \frac{\rho_{gas}\left|u_i + u_i - v_i'\right| d}{\mu_{air}} \tag{44}$$

d is the drop diameter and μ_{air} is the air viscosity which is evaluated at the temperature $\hat{T}$ given by

$$\widehat{T} = \frac{T_{gas} + 2T_d}{3} \tag{45}$$

where T_{gas} is the gas temperature and T_d is the drop temperature. Furthermore, the Schmidt number of air is $Sc = \mu_{air} / \rho_{gas} D$ and D is determined from the correlation:

$$\rho_{gas} D = 1.293 D_0 \left(\widehat{T} / 273 \right)^{n_0 - 1} \tag{46}$$

In addition, Y_1^* is determined from the expression:

$$Y_1^* = \frac{M_{C_n H_{2m}}}{M_{C_n H_{2m}} + M_{mix} \left(\frac{p_{gas}}{p_v} - 1 \right)} \tag{47}$$

where M_{mix} is the molecular weight of the mixture (not including vapor from the liquid species), p_{gas} is the gas pressure, and p_v is the vapor pressure at the current droplet temperature.

A stochastic turbulent dispersion model is used to represent the effect of turbulence on the droplet. CONVERGE models the effects of the turbulent flow on spray drops by adding a fluctuating velocity u_i' to the gas velocity u_i using the RANS (Reynolds Averaged Navier-Stokes) turbulence model.

The source term in Equation (29) accounts for the turbulent kinetic energy reduction due to turbulent eddies when dispersing the droplets of liquid spray as described below:

$$S_s = -\frac{\sum_p N_p \left(F'_{drag,i} u'_i \right)_p}{V} \tag{48}$$

where the summation is over all parcels in the cell, N_p is the number of drops in a parcel, V is the cell volume and

$$F'_{drag,i} = \frac{F_{drag,i}}{\left(u_i + u'_i - v_i\right)} u'_i \tag{49}$$

where $F_{drag,i}$ is the drag force on a drop. Each component of u_i' follows a Gaussian distribution given by:

$$G(u'_i) = \frac{1}{\sqrt{2\pi\sigma}} \exp\left(\frac{-(u')^2}{2\sigma^2}\right) \tag{50}$$

with a variance σ^2 given by 2/(3k). Again k is the turbulent kinetic energy. Then the cumulative distribution function is given by

$$\widetilde{G}(u_i') = erf\left(\frac{u_i'}{\sqrt{2\sigma^2}}\right) = erf(\zeta) \quad 0 < \zeta < 2 \tag{51}$$

where

$$\zeta = \frac{u'_i}{\sqrt{(4/3)k}} \tag{52}$$

2.2.3 Combustion Modeling and Well Mixed Turbulent Chemistry Interaction

SAGE detailed chemistry solver[65] is used to model the combustion process. The SAGE chemistry solver uses CHEMKIN formatted chemical reaction mechanisms[66]. At the beginning of each time-step, the chemical reactions are solved in each cell based on the cell temperature, pressure, and species mass fractions calculated from the RANS conservation equation. Based on the reaction rates, the species mass fractions are then updated accordingly. The turbulence combustion interaction modeling (TCI) was not considered in the present study. As discussed by Pomraning et al. [67], an appropriate TCI model will reveal more small-scale details of flame structure compared to the well-mixed models. However, such models are much more

computationally expensive when implemented with detailed mechanisms in engine-type simulations. On the other hand, the well-mixed models have been shown to be accurate enough for predicting the basic two-phase flow properties, i.e., spray and vapor penetration, temperature profile, ignition delay, and flame lift-off length, etc. Moreover, previous studies have demonstrated the validity of such models for predicting combustion processes in both gasoline and compression ignition engines. In particular, Pomraning et al.[68] have provided a detailed assessment of the unsteady RANS-based approach, and demonstrated that for well-resolved computations, the effects of mixing are accounted for using the RANS turbulence model. Detailed description of the well-mixed turbulence-chemistry interaction approach are included in Appendix B. To reduce chemistry computational time, the multi-zone method is employed[69].

The CFD solver uses an innovative modified cut-cell Cartesian method for grid generation[70]. Moving boundaries are specified automatically generated. The mesh of grid is also redrawn at every time step. The adaptive mesh resolution (AMR) technique enables mesh refinement in regions of high curvatures for temperature, velocity and important species mass fraction. For the results presented here, the base (largest) grid size is fixed at 2mm. In order to resolve the flow near the injector, a local refinement area with 0.125mm grid sizes are used, along with AMR based on the curvature in the velocity and temperature fields. These grid sizes have been determined to be sufficient to capture the spray droplet break up, vaporization, and combustion processes since the RANS computational field can be well resolved. Note that the simulation in this work only focuses on the subsonic cases. Sample calculations regarding the Mach number are included in Appendix C.

2.3 CHEMISTRY KINETICS

2.3.1 Gas Phase Chemistry

A detailed mechanism for counterflow flame simulation has been used in this research. For the detailed mechanism to model n-heptane and 1-heptene flames, it has been developed by extending a detailed oxidation scheme for several fuels[71,72]. This chemistry model is based on a detailed submechanism of C_1–C_4 species. "Assuming analogy rules for similar reactions, only a few fundamental kinetic parameters are required for the progressive extension of the scheme toward heavier species. It consists both the NO_x and PAH formation kinetics."[53] The NO_x mechanism is adopted from various sources. The thermal NO formation is modeled using the extended Zeldovich mechanism[73]. The prompt NO mechanism is that proposed by Glarborg et al.[74] , while the intermediate N_2O mechanism is that reported by Malte and Pratt[75]. The NNH mechanism is adopted from the study of Smallwood et al.[76,77]. Validation of the NO_x mechanism can be found in publications reported by Shimizu et al.[78] and Frassoldati et al.[79] The kinetic model used for fuel oxidation is also capable of simulating the formation of PAHs up to pyrene ($C_{16}H_{10}$). The resulting kinetic model of hydrocarbon oxidation from methane up to n-octane consists of 198 species and 4932 reactions.

2.3.2 Soot Formation and Oxidation Chemistry

Figure 4 presents a schematic of the soot formation processes[80]. As fuel molecules begin to decompose, intermediate hydrocarbon species are formed in fuel rich regions, which undergo further reactions to form PAHs. Once the primary particle is formed through nucleation and polymerization, it can grow through surface reactions and coagulation, and also undergo oxidation. Particle inception is modeled by a nucleation reaction with two pyrene molecules as the reactants. The nucleation reaction is an irreversible reaction which provides the particle inception rate and

defines the size and the surface coverage of the particle (or nucleus). The nuclei start to interact with each other through coagulation as well as with the gaseous species on its surface. The dynamics of coagulation can be modeled by solving particle size distribution functions (PSDFs). To solve PSDFs, either a discrete-sectional method[81] or the method of moments[82] can be used. Although reasonably accurate, discrete methods are known to be computationally very expensive and are not considered here. Instead, the method of moment employed by Frenklach[82,83] is used to describe the moments of the PSDFs. The results reflect the average properties of soot population without a priori knowledge of PSDF; therefore require dramatically less computational resources. The soot formation model also includes surface reactions with gaseous species to determine the surface growth and oxidation rates[82]. The soot aggregation process is not considered in the present study.

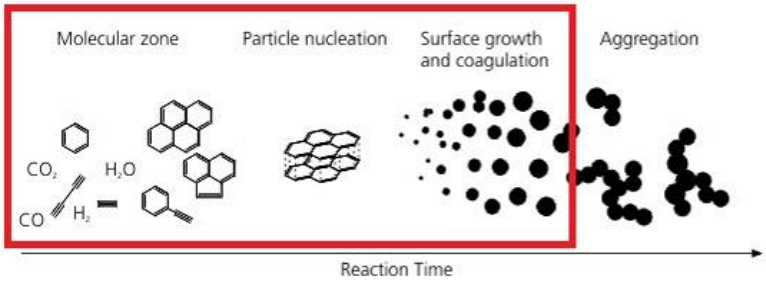

Figure 4. Soot formation process. Red box indicates the formation processes considered in current model.

In this study, the method of moment (MOM) developed by Appel et. al.[84], is used to solve the moments of the PSDF. The results only reflect the average soot characteristics, but cost dramatically less computation resource. The soot formation model includes nucleation, surface

growth, coagulation and aggregation. The Smoluchowski model[85] describes the time evolution of particle population by an infinite set of differential equations

$$\frac{\mathrm{d}N_1}{\mathrm{d}t} = -\sum_{j=1}^{\infty} \beta_{1,j} N_1 N_j$$

$$\frac{\mathrm{d}N_i}{\mathrm{d}t} = \frac{1}{2}\sum_{j=1}^{i-1} \beta_{j,i-j} N_j N_{i-j} - \sum_{j=1}^{\infty} \beta_{i,j} N_i N_j \qquad (53)$$

$$i = 2,...,\infty$$

$\beta_{i,j}$ is the collision coefficient.

In the MOM, Eq. (53) can be rewritten as

$$\frac{\mathrm{d}M_0}{\mathrm{d}t} = -\frac{1}{2}\sum_{i=1}^{\infty}\sum_{j=1}^{\infty} \beta_{i,j} N_i N_j$$

$$\frac{\mathrm{d}M_1}{\mathrm{d}t} = 0$$

$$\frac{\mathrm{d}M_2}{\mathrm{d}t} = \sum_{i=1}^{\infty}\sum_{j=1}^{\infty} ij\,\beta_{i,j} N_i N_j \qquad (54)$$

$$\frac{\mathrm{d}M_3}{\mathrm{d}t} = 3\sum_{i=1}^{\infty}\sum_{j=1}^{\infty} ij^2\,\beta_{i,j} N_i N_j$$

"Where $M_r = \sum_{i=1}^{\infty} m_i^r N_i$ is the r th moment. m_i is the mass of the soot particle of size class i. N_i is the soot number density of size class i, which is defined by the number of soot particles per unit volume. M_0 represents soot number density, N_s per unit volume. M_1 represents average total mass of soot particles, m_s, per unit volume. Thus, the soot mass fraction is $Y_s = \frac{M_1}{\rho}$, where

ρ is the mixture density. The soot volume fraction is $f_V = \frac{\rho Y_s}{\rho_{soot}}$, where $\rho_{soot} = 1.8\text{g/cm}^3$ is the soot density. Finally, the average particle diameter is $d_p = \left(\frac{6.0 M_2}{\pi \rho_{soot} M_1} \right)^{1/3}$."[86]

So the infinite number of PSDF is replaced by a small number of equations for the corresponding moments, which results in an advantage in numerical economy.

In the coalescent limit, where the soot particles still form the spherical shape after collision. The r th moment M_r can be calculated using the following equation:

$$\frac{\partial M_r}{\partial t} = R_r + C_r + S_r + F_{M_r}, \; r = 0,1,2,3,... \tag{55}$$

The terms R_r, C_r, and S_r are nucleation, coagulation and surface growth effect on the r-moment equation, respectively. The coagulation is considered in the coalescent limit. Whenever the soot particle exceeds a critical diameter, the particles start to aggregate to form an aggregate structure. However, the aggregation process F_{M_r} is not included in this work.

The nucleation effect is modeled as

$$R_r = N_{avo} k_n M_c^r / C_{\in} \tag{56}$$

The $C_{\in}$ is the minimum number of 2C molecules to form an initial soot nucleus. N_{avo} is Avogadro's number. k_n is the rate constant for nucleation, calculated through Arrhenius equation:

$$k_n = A_{nuc} \times T^{B_{nuc}} \times \exp\left(-\frac{E_{nuc}}{RT} \right) \times \prod_k [\chi_k]^{\nu_k} \tag{57}$$

A_{nuc}, B_{nuc}, and E_{nuc} are the Arrhenius coefficients from nucleation mechanism. χ_k and v_k are the chemical symbols and the stoichiometric coefficient of the k-th gas reactant in the nucleation reaction, respectively. Also the calculation in Frenklach and Harris [87] shows:

$$A_{nuc} = \beta \times \sqrt{\frac{4\pi\kappa_B}{j_{PAH} \times m_0}} \times N_{avo} \times d_{PAH}^2$$

$$B_{nuc} = 1/2 \tag{58}$$

$$E_{nuc} = 0$$

The nucleation process affects only the number density of class j_{PAH} particle. m_0 is the mass of a bulk species molecule and is constant. d_{PAH} is the diameter of the PAH precursor pyrene. The nucleation mechanism is assumed based on the reaction between two pyrene molecules:

2 A_4 => 32 C bulk + 20 H site+ 28.74877 open site

A = 9.0E+09, B = 0.5, E = 0

The surface growth term in Eqn. (55) is computed as

$$S_r = \pi \left(\frac{6}{\pi\rho} \right)^{2/3} \frac{k_S - k_{OX}}{\Delta m} M_0 \sum_{k=0}^{r-1} \Delta m^{r-k} \mu_{r+2/3} \tag{59}$$

r = 1, 2, 3,…

Here, $\mu_r = \frac{M_r}{M_0}$, Δm represents the mass increment from one size class to another due to addition or abstraction of species to or from the soot particle surface. When a particle of size m_i is increased by Δm, it will be transferred to the size class i + 1. The rate constants for surface

growth and oxidation, k_S and k_{OX}, are calculated through Arrhenius Equations for the pseudo surface reactions mechanism provided separately. Take a sample pseudo surface reaction for deposition of gas species:

$$\chi + < surface\_reactants > \Rightarrow \Delta j_\chi C\_bulk + < gas\_products >$$

A_S, B_S, E_S should be provided

The frequency coefficient for collisions between two particles of sizes i and j due to Brownian motion in the free-molecular regime, is given by

$$C_0 = \frac{1}{2}\sum_{i=1}^{\infty}\sum_{j=1}^{\infty}\beta_{i,j}N_iN_j$$

$$C_r = \frac{1}{2}\sum_{k=1}^{r-1}\binom{r}{k}\left(\sum_{i=1}^{\infty}\sum_{j=1}^{\infty}m_i^k m_j^{r-k}\beta_{i,j}N_iN_j\right) \tag{60}$$

r = 2, 3, …

β represents the collision coefficient in Eqn. (58). However, the form of β depends on coagulation regime, classified based on the Knudsen number, $Kn = \frac{2\lambda_f}{d}$. λ_f is the gas mean free path and d the particle diameter. Three specific regimes are considered in MOM, which are continuum regime, free-molecular regime and transition regime.

a) Continuum regime

The continuum regime of coagulation is characterized by Kn << 1. The final form of collision coefficient is:

$$\beta_{ij}^{c} = K_c \left(\frac{C_i}{m_i^{1/3}} + \frac{C_j}{m_j^{1/3}} \right) \left(m_i^{1/3} + m_j^{1/3} \right) \tag{61}$$

where $K_c = \frac{2k_B T}{3\eta}$, and C the Cunningham slip correction factor. $C = 1 + 1.257 Kn$. So Eqn. (60) becomes:

$$C_0^c = K_c \left[M_0^2 + M_{1/3} M_{-1/3} + K_c' \left(M_{-1/3} M_0 + M_{1/3} M_{-2/3} \right) \right]$$

$$C_r^c = \frac{1}{2} K_c \sum_{k=1}^{r-1} \binom{r}{k} \left[\begin{array}{l} 2M_k M_{r-k} + M_{k-1/3} M_{r-k+1/3} + M_{k+1/3} M_{r-k-1/3} + \\ K_c' \left(M_{k-1/3} N_{r-k} + M_k M_{r-k-1/3} + M_{k-2/3} M_{r-k+1/3} + M_{k+1/3} M_{r-k-2/3} \right) \end{array} \right] \tag{62}$$

where $K_c' = 2.514 \lambda \left(\frac{\pi \rho}{6} \right)^{1/3}$, ρ is the particle material density. The fractional order moments is determined by interpolation among whole-order moments.

b) Free-molecular regime

The free-molecular regime is chosen when Kn >> 1. In this limit, the collision coefficient for coalescent collisions of spherical particles is given by

$$\beta_{ij}^{f} = K_f \sqrt{\frac{1}{m_i} + \frac{1}{m_j}} \left(m_i^{1/3} + m_j^{1/3} \right)^2$$

$$K_f = \varepsilon \sqrt{\frac{6k_B T}{\rho}} \left(\frac{3}{4} \pi \rho \right)^{1/6} \tag{63}$$

The coagulation term in Eqn. (55) becomes:

$$C_0^f = \frac{1}{2} K_f M_0^2 f_{1/2}^{(0,0)} \tag{64}$$

$$C_r^f = \frac{1}{2} K_f M_0^2 \sum_{k=1}^{r-1} \binom{r}{k} f_{1/2}^{(k,r-k)} \text{ , r = 2, 3, …}$$

where f_l is a grid function:

$$f_l = \sum_{i=1}^{\infty} \sum_{j=1}^{\infty} \left(m_i + m_j \right)^l m_i^{1/2} m_j^{1/2} \left(m_i^{1/3} + m_j^{1/3} \right)^2 N_i N_j \text{ , 1 = 0, 1, 2,…} \tag{65}$$

And $f_{1/2}$ is obtained by interpolation among f_0, f_1 and f_2. It can be expressed in exact terms, using fractional-order moments. For example:

$$\begin{gathered} f_1 = 2\mu_{13/6}\mu_{1/2} + 4\mu_{11/6}\mu_{5/6} + 2\mu_{3/2}\mu_{7/6} \\ \mu_r = M_r / M_0 \end{gathered} \tag{66}$$

In such way, we can get the coagulation term in free-molecular regime.

c) Transition regime

The transition regime is between the two limits, the continuum regime and the free-molecular regime. The calculation for the coagulation rate is the harmonic mean of the limit values due to the complexity of the functional form. A harmonic mean is shown:

$$C_r = \frac{C_r^f C_r^c}{C_r^f + C_r^c}, \ r = 0, 2, 3, ... \tag{67}$$

Numerical simulations are performed to examine the effects of strain rate, equivalence ratio and fuel molecular structure on PAH and soot emissions.

2.3.3 Mechanism Reduction

To verify the conclusion of the first part in this study, 1-heptene will be used as the liquid fuel in spray combustion simulations. A more detailed chemistry mechanism which considers both

(a) methane and 1-heptene as the fuel, (b) all the NO formation routes and (c) all the PAH formation routes is developed and implemented into CFD simulation. The new mechanism is a semi-reduced mechanism to maintain reasonable computational cost. A skeletal mechanism has been developed based on Directed Relation Graph with Error Propagation and Sensitivity Analysis (DRGEPSA). This skeletal mechanism (207 species and 4094 reactions) is reduced from the CRECK mechanism developed at Polytechnic University of Milan (482 species and 19072 reactions). This detailed mechanism is adopted from the newest version of the complete mechanism (low and high temperature) by Ranzi et al[88, 89,90,91,92].

The DRGEPSA algorithm consists of two phases: (1) Directed Relation Graph Error Propagation (DRGEP) and (2) Sensitivity Analysis (SA). The directed relation graph (DRG) mechanism reduction procedure is developed by Lu and Law[93]. Due to the complicity in the coupling of the species when identifying the species that is not important and removing it, the following rule is specified to determine whether a species can be removed. Considering species A directly forms species B, Species B can be removed when the removal of B will not introduce a significant error to the rate of production for species A. This error is determined by a normalized contribution of reaction A->B among all the reactions depend on species A. In this study, the normalized error criteria is set at 0.15. Also the key species can be specified to keep certain important reaction routes such as the detailed PAH and NO_x formation routes. CH_3, C_2H_2, C_6H_6, $C_{16}H_{10}$, C_2H_4, C_3H_3, CYC_5H_6, $C_{10}H_8$, $C_6H_5C_2H_3$, NO, N_2O, NNH, CH, CO, OH, HO_2, H_2O_2 and NC_7-QOOH are specified to be kept in this work. The resulting reduced mechanism also contains all the species related to these key species. Once the optimal mechanism is obtained from the DRGEP step, sensitivity analysis is performed to further reduce the size of the mechanism. All the species after DRGEP step are arranged in ascending order based on the error in ignition delay

induced by removing this species. The sensitivity analysis removes the species identified from the top of the list one by one until the error generated by the resulting skeletal mechanism with the remaining species reaches the user-defined tolerance for ignition delay.

The resulting reduced CRECK mechanism contains oxidation for n-heptane, 1-heptene and methane and emission formation routes for thermal, prompt, N_2O and NNH intermediate NO routes and PAH formation routes up to pyrene. The reduced CRECK mechanism contains 207 species and 4094. Validations are provided in the following chapter.

3 VALIDATION AND DISCUSSION

In this chapter, both the numerical simulations and reduced/semi-detailed reactions mechanisms kinetics are validated with experimental data adopted from literature.

3.1 IGNITION DELAY

The reduced CRECK mechanism was validated against the shock tube ignition data for n-heptane and 1-heptene, as well as the non-reacting and reacting spray data from ECN. Figure 5 presents a comparison of the predicted ignition delays against the measurements of Gauthier et al.[94] for n-heptane/air mixtures. Simulations were performed in constant-pressure, homogeneous reactor using the CHEMKIN software and four different mechanisms, namely, the reduced CRECK mechanism, Chalmers mechanism[95, 96], detailed CRECK mechanism (482 species and 19072 reactions) [97,98], and detailed Lawrence Livermore National Laboratory (LLNL) mechanism [99]. Overall, there is good agreement between the various predictions and measurements. At high temperatures (T>1100 K), all the four mechanisms slightly overpredict ignition delays. However, at lower temperatures, relevant for ignition in diesel engines, there is reasonably good agreement. Moreover, the reduced mechanism reproduces the experimentally observed negative temperature coefficient (NTC) regime, wherein the ignition delay increases with temperature. Figure 6 compares the ignition delays for 1-heptene/air mixtures predicted using the reduced and detailed CRECK mechanisms against the measurements of Garner et al.[100]. Both the mechanisms are able to reproduce the experimental data, although the values are somewhat overpredicted. Note that due to limited experimental data, simulations only considered temperatures greater than 1300K.

Moreover, for temperatures below 1300, the ignition delays for 1-heptene become significantly higher compared to those for n-heptane.

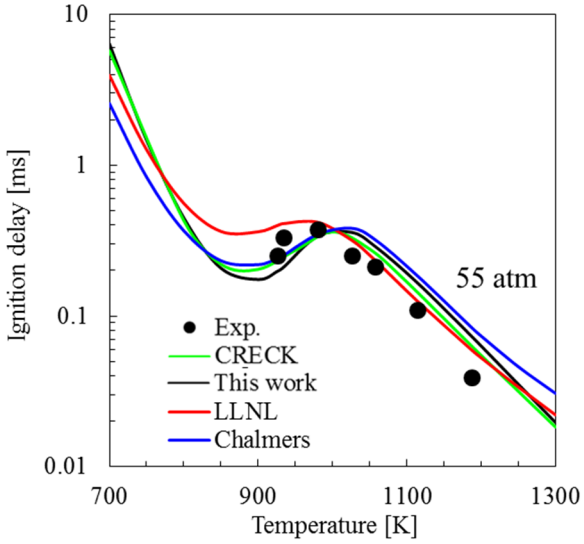

Figure 5. Predicted and measured ignition delays for n-heptane/air at p = 55 atm and ϕ = 1. Black line represents the reduced CRECK mechanism developed in this work.

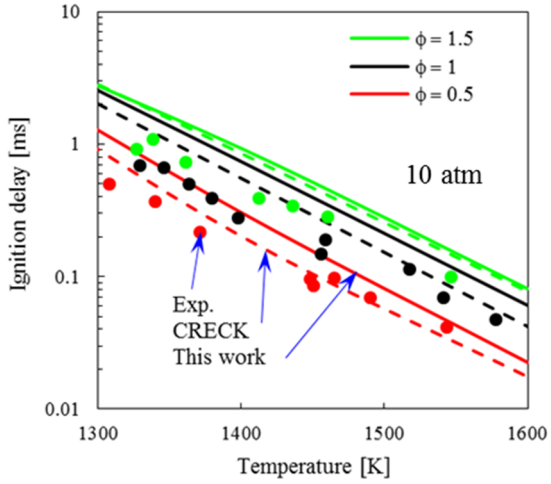

Figure 6. Predicted and measured ignition delays for 1-heptene/air mixtures at p = 10 atm, and three equivalence ratios, ϕ = 1.5, [C_7H_{14}] =1248 ppm, ϕ = 1, [C_7H_{14}] = 873.3 ppm,

and ϕ = 0.5, [C_7H_{14}] = 447.6 ppm. Solid and dashed lines in Fig. 1b indicate simulation results with the reduced and detailed CRECK mechanisms, respectively.

Since the oxidation of a long chain hydrocarbon is highly dependent on the oxidation of C1-C4 hydrocarbons, additional validation for the reduced mechanism is provided for methane/air ignition delay calculations. Figure 7 compares the simulated results using the reduce mechanism, the detailed CRECK mechanism, the Chalmers mechanism[101,102] (42 species and 168 reactions), the mechanism from Lu et. al.[103], the LLNL mechanism, the Mechanism developed by Metcalfe et. al.[104], and the GRI mechanism[105] against the shock tube measurements of Huang et al.[106] for methane/air mixtures. Overall, there is good agreement between the predictions and measurements at a range of equivalence ratios. The ignition delays calculated using this reduced mechanism and the CRECK mechanism are closer to the experimental results compared to other mechanisms.

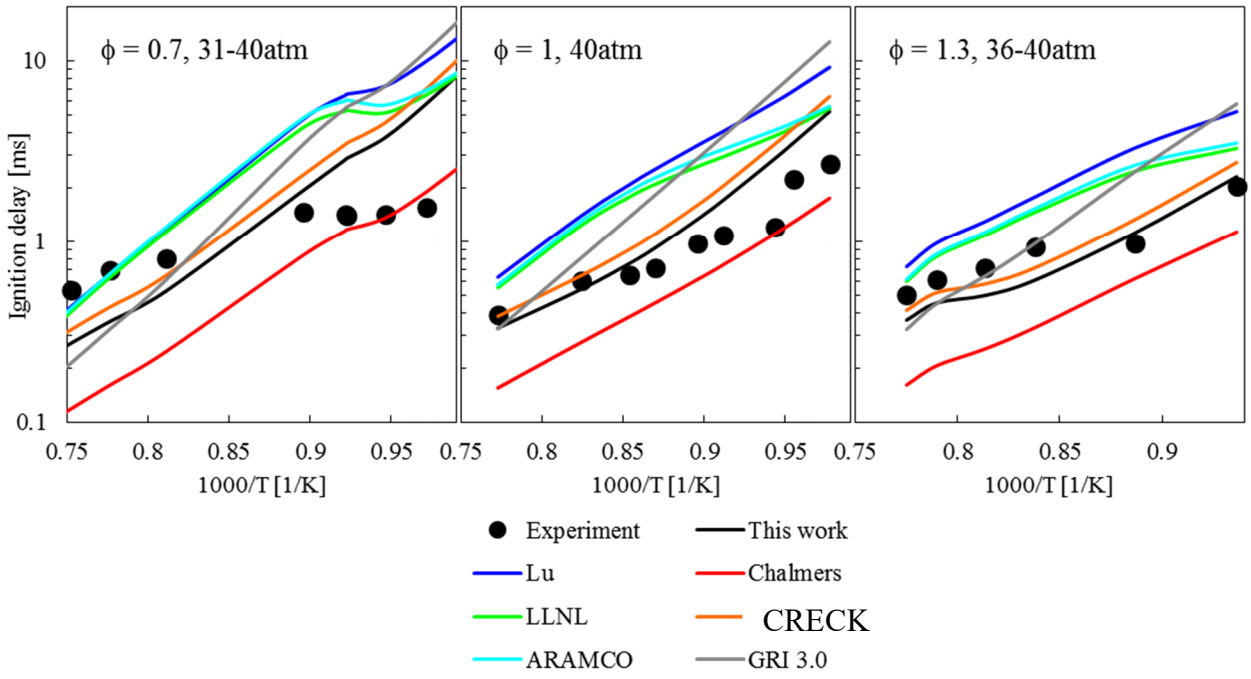

Figure 7. Predicted and measured ignition delays for methane/air at p = 40 atm and ϕ = 0.7, 1 and 1.3.

3.2 LAMINAR FLAME SPEED

Since the laminar flame speed is an important parameter for the propagation of methane/air premixed flame in the dual-fuel engine, flame speed validations for methane/air mixtures are presented in Figure 8. The calculated flame speeds using both the Chalmers and GRI (53 species and 325 reactions) mechanisms agree with the experiments for various pressure conditions. However, the values using the Chalmers mechanism are somewhat underpredicted at 10 atm which is not typical of the engine operating conditions. At pressures from 20 to 60 atm, Chalmers mechanisms over-predicts the flame speed for lean methane/air mixtures. So the n-heptane ignition delay and methane flame speed results using the Chalmers mechanism are acceptable for the dual-fuel combustion application. And considering the relative smaller number of species and reactions for Chalmers mechanism compared to other two comprehensive mechanism, the Chalmers mechanism is employed in the current study to reduce the computational cost.

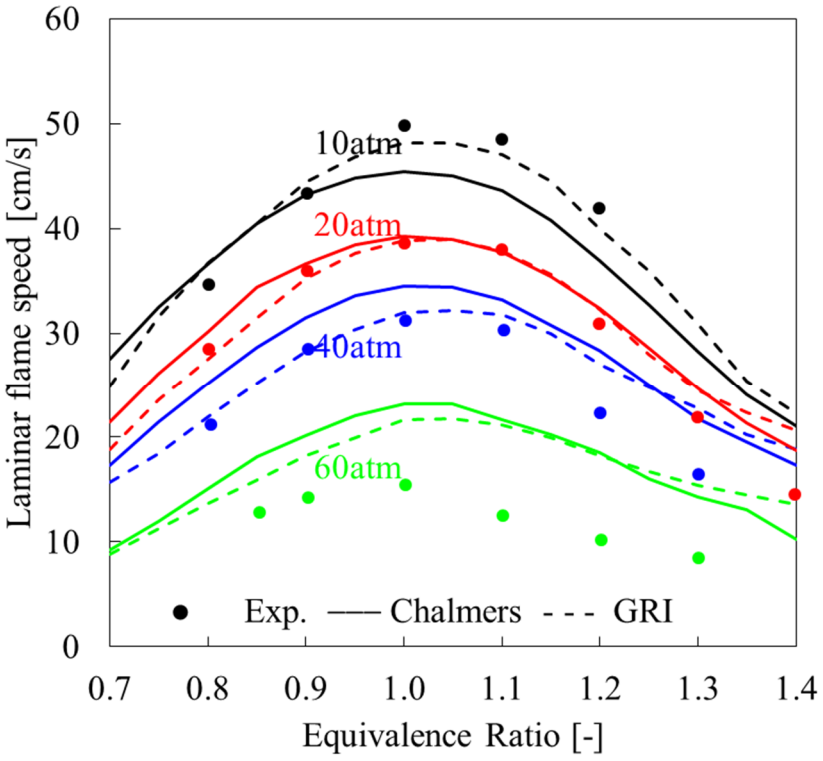

Figure 8. Predicted and measured flame speed of methane/air mixtures at various pressure from 10 to 60 atm. Simulations are performed with Chalmers and GRI mechanisms.

3.3 COUNTERFLOW FLAME

While the kinetic mechanism has been extensively validated in previous studies[53], we provide an additional validation here for an n-heptane PPF established at $\phi = 4.27$, $a_G = 100s^{-1}$, and nitrogen dilution of 17%. Figure 9 presents the predicted and measured mole fraction profiles for several hydrocarbon species including a PAH species, benzene. There is a good qualitative agreement between predictions and measurements, especially with respect to intermediate hydrocarbon (C_2H_2, C_2H_4 and CH_4) species profiles. However, the peak benzene mole fraction is over-predicted by about 25% compared to measurements.

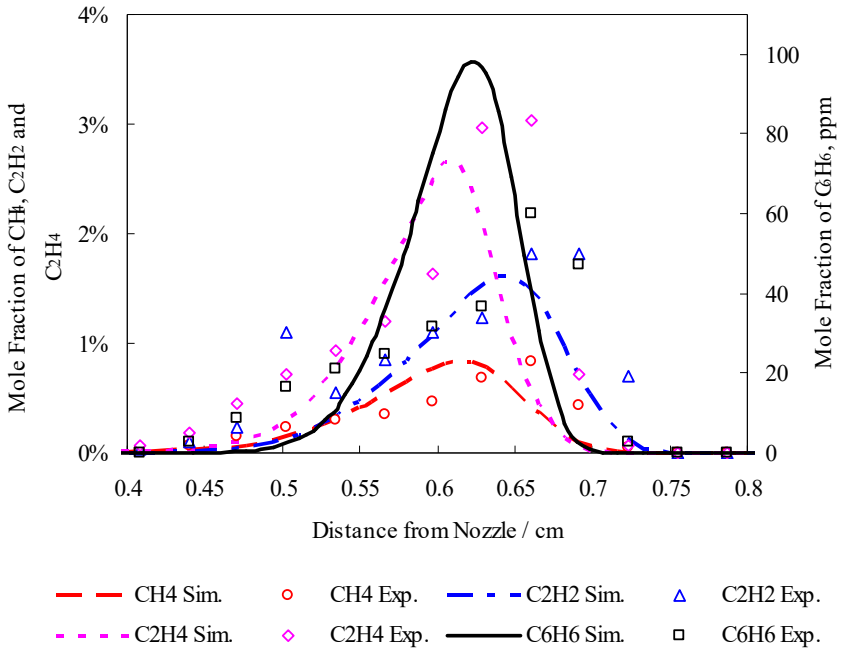

Figure 9. Predicted (lines) and measured (symbols) flame structures in terms of species mole fraction profiles for n-heptane partially premixed flame at $\phi = 4.27$, $a_G = 100\ s^{-1}$, and nitrogen dilution of 17%, which contains CH_4 (O), C_2H_2 (Δ), C_2H_4 (◊) and C_6H_6 (□) profiles.

A validation of the soot model is presented in Figure 10, which presents a comparison of the predicted soot volume fraction profiles with the measurements of Hwang and Chung[107] and Vansburger et al.[108] in a counterflow ethylene diffusion flame. For these results, the separation distance between the fuel and oxidizer nozzles was 1.42cm, and the exit velocities of both fuel and oxidizer streams were 19.5cm/s. Results are shown for two compositions of the oxidizer stream, namely 20% O_2 + 80% N_2 and 24% O_2 + 76% N_2 by volume. There is generally good agreement between the predictions and measurements for both the cases, with the numerical model under-predicting soot volume fractions by about 20% to 30%. In addition, the soot inception seems to occur earlier and the soot volume fraction profiles are wider in the experimental study. This may

be attributed to the fact that soot aggregation is not included in our soot model. However, similar discrepancies between predictions and measurements have been reported by Liu et al.[109], who attributed them to the lack of information on experimental conditions including boundary conditions. Consequently, they adjusted the separation distance between the two nozzles, and the surface growth rate in their model in order to achieve better agreement with the measurements of Hwang and Chung[107]. Moreover, there are also differences between the two sets of measurements apparently for the same conditions. In view of these factors, the prediction of soot emission using the present model is deemed acceptable.

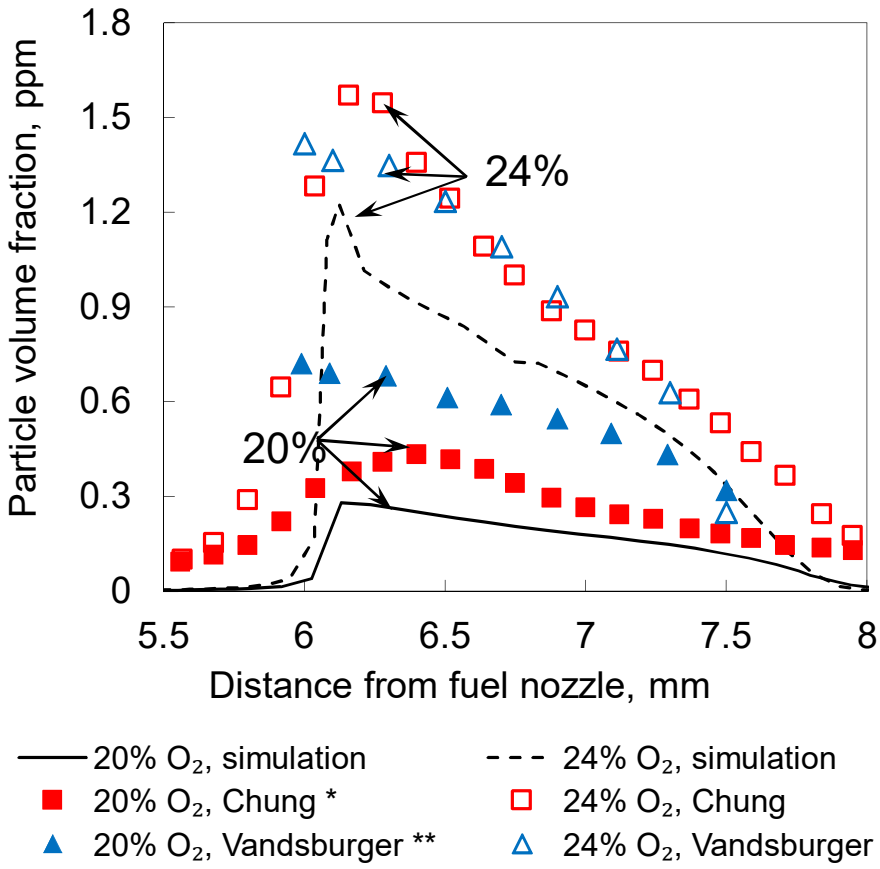

Figure 10. Predicted (lines) and measured (symbols) soot volume fraction profiles for pure C_2H_4 diffusion flame. Fuel and oxidizer nozzle exit velocities are both 19.5 cm/s. Nozzle separation length is 1.42 cm. (Δ) symbol is experimental data from Vansburger et al. 108 (□) symbol is experimental data from Hwang and Chung107. The mole fraction of O_2 in oxidizer stream is 24% and 20% for the two cases. Vertical line represents the stagnation plane.

3.4 NON-REACTING SPRAY

Investigating the engine combustion processes is always challenging due to the many factors. Because the flow and thermal conditions in a cylinder can vary when fuel / air mixing started after liquid fuel is injected. Therefore, the liquid fuel injection and combustion processes are simulated or the Spray Combustion Vessel in the Collaborative Research Facility at Sandia National Laboratory at different ambient conditions when fuel injection starts. The detailed effects of each variable for the spray combustion can be studied systematically. Different composition of the in-cylinder gases, ambient temperature/pressure/gas density and fuel injector parameters can are used to analyze the effect on combustion and emission-formation processes. The schematic of the combustion vessel is depicted in Figure 11. An extensive dataset from for this kind of combustion vessel is available to download at the Engine Combustion Network (ECN). For the CONVERGE simulations in this study, n-heptane is used as the liquid fuel. Results are compared with ECN data in two categories, non-reacting and reacting n-heptane sprays.

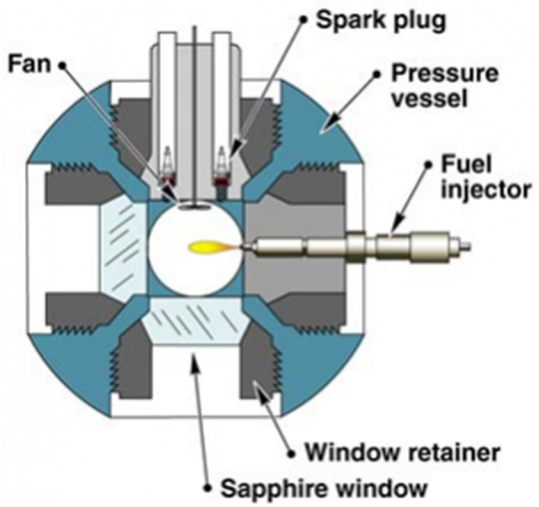

Figure 11. Schematic of the spray combustion vessel in the collaborative research facility at Sandia National Laboratory.

Figure 12 presents the liquid (a) and vapor (b) penetrations for the base n-heptane non-reacting case (ambient temperature 1000K, initial density 14.8kg/m^3, injection pressure 150MPa, nozzle diameter 0.1mm). Three simulation results are reported, which uses the same injection profile as experiment and 0.125mm as the smallest grid size. Different turbulence models are used for the flow field. Two Reynolds Averaged Navier-Stokes (RANS) turbulence models include the standard k-ε and Renormalization Group (RNG) k-ε models. One Large Eddie Simulation (LES) model used is Dynamic Smagorinsky model[110] (DS LES). The grid size 0.125mm is small enough to obtain grid convergence on vapor penetration for all these models which will be explained in next figure. These simulations can all give relatively good prediction on both vapor and liquid penetrations except RNG k-ε model. The best match in vapor penetration can be obtained by using DS LES turbulence model, which is plotted using black line. However, the liquid penetration over predicts before 0.5ms.

As indicated in Figure 13, the predicted liquid and spray penetrations are generally in good agreement with measurements. The liquid penetration increases with time, and then stabilizes to a

quasi-steady value. While the qualitative trends are captured with all the three grid sizes, the quantitative agreement improves as the grid size is reduced, except for the initial liquid penetration (for time below 0.5ms), which is overpredicted by the model. As discussed by Som et al.[111], such differences may be attributed to several factors, including experimental uncertainties in near-nozzle measurements, under-resolution of flow in the near-nozzle region, and inability to capture the effect of cavitation and turbulence in the injector flow. It is also important to note that the predicted results are fairly grid-independent for the grid sizes of 0.25 and 0.125mm, and the spray development and vaporization processes are fairly well resolved using the k-ε turbulence model with the minimum grid size of 0.125mm. These results are consistent with previous studies concerning grid convergence. Som et al.[111] performed computations of non-reacting and reacting sprays for n-heptane and n-dodecane fuels, and observed good agreement between measurements and predictions using the RNG k-ε turbulence model with minimum grid size of 0.25mm. Xue et al.[112] also performed simulations for the same two fuels using the RANS and LES turbulence models, and reported grid convergence with grid sizes of 0.25mm and 0.125mm. Thus, the simulations in the present study were performed using the minimum grid size of 0.125mm and four levels of adaptive mesh refinement (AMR) based on the velocity and temperature fields, but a fixed grid embedding near the nozzle.

Figure 14 presents one validation of the mixture fraction on radial direction at 40mm axial location at 1.1ms after start of injection. The experiment data from ECN n-heptane non-reacting spray is compared with the result using standard k-ε model. The simulation generally under-predicts the mixture fraction values. But the Gaussian nature of the mixture fraction distribution is well captured qualitatively.

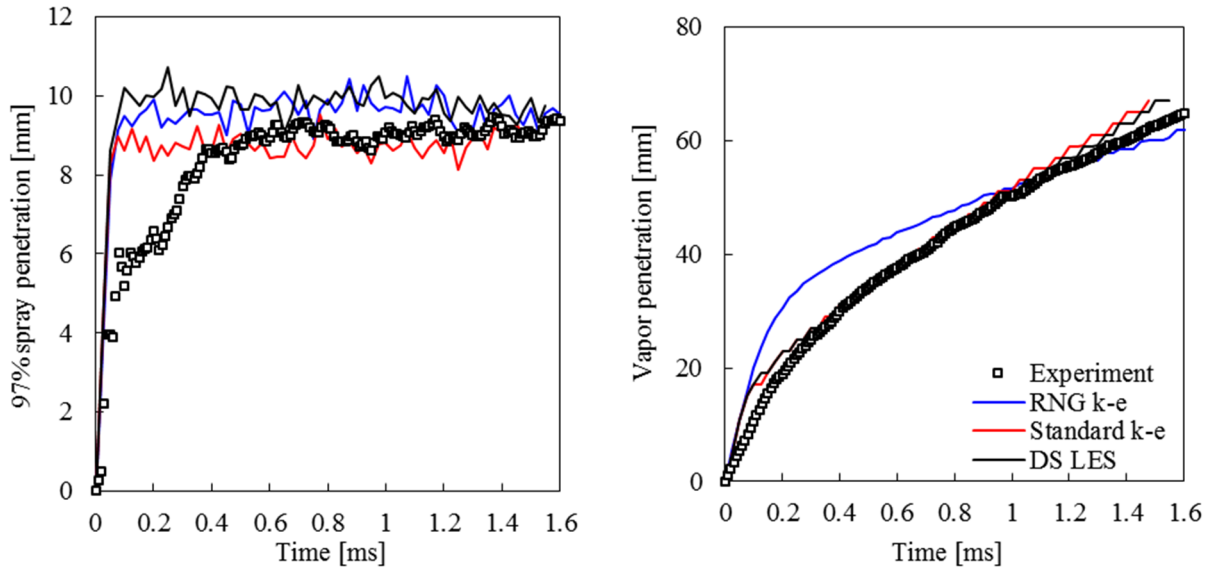

(a) (b)

Figure 12. Vapor and liquid penetration comparisons for n-heptane non-reacting spray using 0.125mm as the smallest grid size. Experimental data is taken from ECN database.

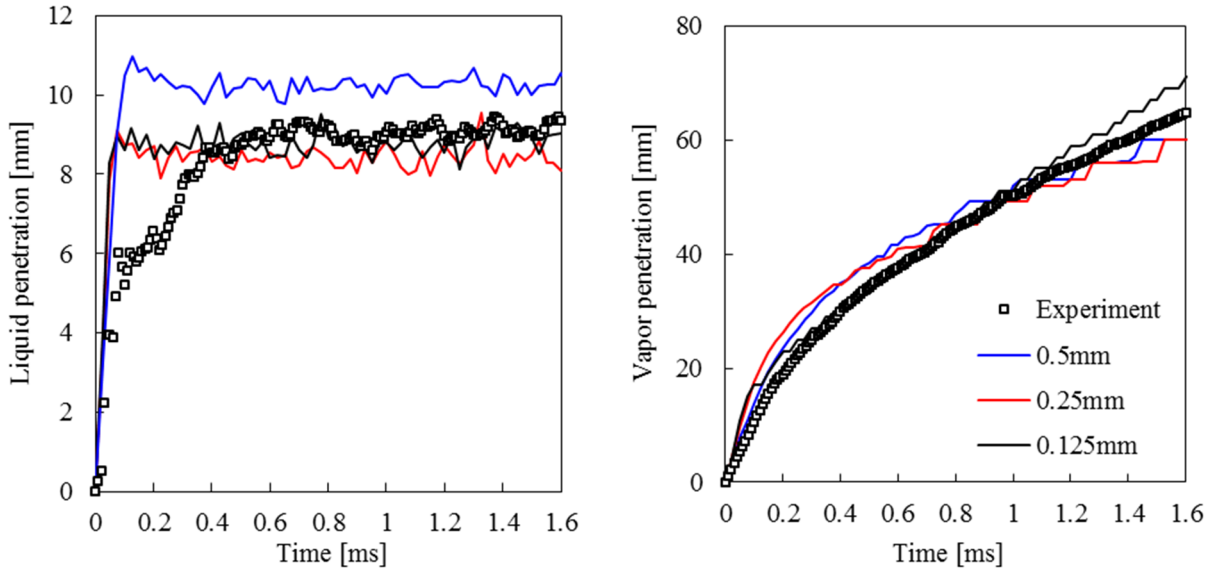

(a) (b)

Figure 13. Measured and predicted liquid penetration (a) and vapor penetration (b) distances for n-heptane non-reacting spray. Predictions are shown for three grid sizes of 0.5mm, 0.25mm and 0.125mm using standard k-ε model.

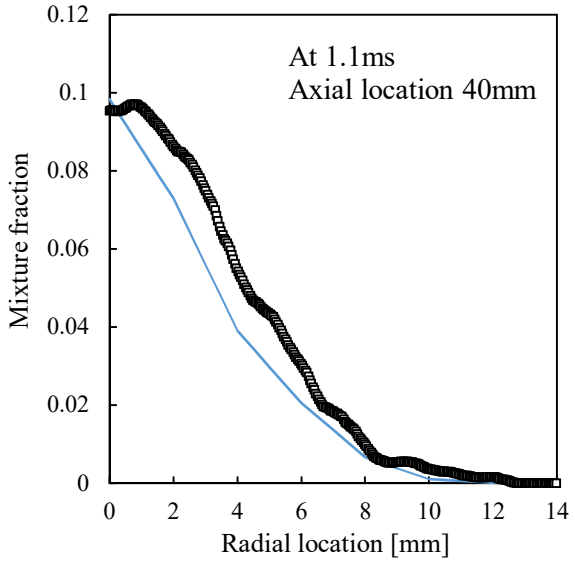

Figure 14. Mixture fraction on radial direction at 40mm downstream from nozzle 1.1ms after start of injection. Black symbols is experimental data. Blue line is simulation result using standard k-ε turbulence model.

3.5 REACTING SPRAY

Figure 15 presents the comparison of predictions in soot mass fraction with the measurement of high speed soot luminosity image from ECN experiment. The soot model used in CONVERGE is adopted from Hiroyasu and Kadota[113]. This soot model assumes spherical particles formed by acetylene and uniform in size, thus can be used for qualitative comparison with luminosity images. With adaptive mesh refinement (AMR), the smallest grid size reaches 0.125mm based on the change in velocity, temperature and fuel mass fraction. Moreover, the grid size is fixed at 0.125mm near the nozzle. Good agreement can be obtained qualitatively and quantitatively. The OH mass fraction contour is used to identify the flame LOL. A specific OH mass fraction contour was used to determine the LOL in simulations, while it was measured using

an intensified CCD camera with a 310nm band-pass filter (10 nm FWHM) [114],[115] in experiments. "A major source of light emission at 310 nm is chemiluminescence from excited-state OH (OH*), which is short-lived and results from chemical reactions in near-stoichiometric, high-heat-release regions." [116,63] The criteria of 2% of the maximum OH mass fraction from simulation is found to be accurate to compare with the experiment. The LOL using this criteria gives accurate prediction with error less than 2.0%. The ignition delay time (τ_{ig}) can be determined using peak temperature and/or OH profiles. The result obtained is also acceptable, with an error of 10% below experiment value. Note that the pressure rise in the reactor is used to determine the τ_{ig} experimentally.

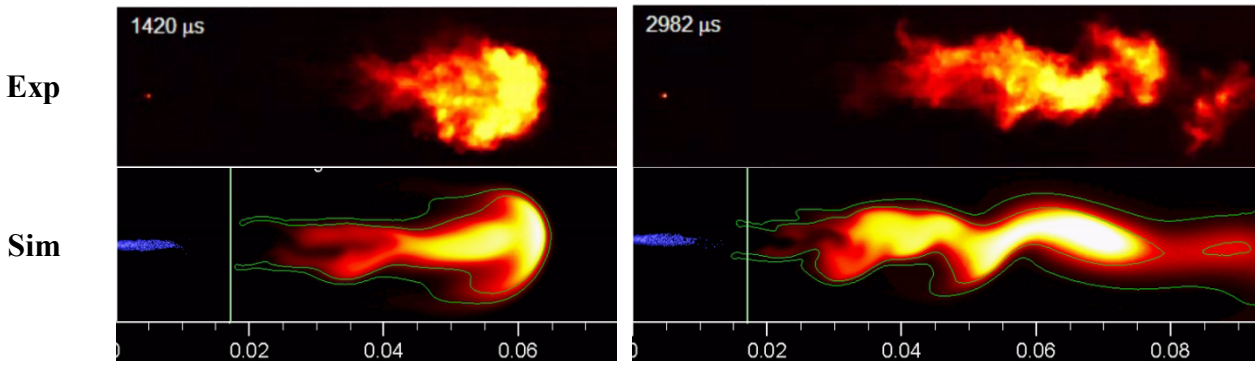

Figure 15. Comparison of predictions (soot mass fraction) of the reacting n-heptane spray using RANS turbulence model with measurements (high speed soot luminosity image) of ECN n-heptane reacting case (ambient conditions: 21% O_2, 1000K and 14.8kg/m^3; injection pressure 150MPa). Solid vertical line in each image indicates the flame LOL at 17mm. Green contour lines are OH mass fraction contours of 0.002 (2% of the maximum). Blue dots are liquid parcels.

Validation results for the n-heptane reacting spray are presented in Figure 16, which compares the measured and predicted ignition delays (τ_{ig}) and flame LOL for different initial temperatures. Additional validation for the predicted τ_{ig} and LOL for different O_2 concentrations

is presented in Figure 17. The experimental conditions used in the simulations are listed in Table 2. In experiments, τ_{ig} was determined using a criterion based on a specific pressure rise, while in simulations, it was computed by using the time from start of injection (SOI) to the instant when the maximum temperature in the computational domain reaches its peak value. A specific OH mass fraction contour was used to determine the LOL in simulations, while it was measured using an intensified CCD camera with a 310nm band-pass filter (10 nm FWHM)[117,118] in experiments. There is fairly good agreement between the predictions and experimental data. Both the experiments and predictions indicate a decrease in ignition delay, and consequently in LOL, as the initial temperature is increased. It is also important to note that both simulations and measurements do not indicate the existence of NTC region, which can be seen in Figure 5 for homogeneous n-heptane/air mixtures. This may be related to the temporally and spatially evolving temperature and species fields for the spray case[119]. As shown in Figure 17, which presents the ignition delay for different initial O_2 concentration cases, an over-prediction can be noticed. The simulation can capture the trend very well that τ_{ig} and LOL values both decrease as the O_2 concentration is increased.

Table 2. Experimental conditions for non-reacting and reacting n-heptane sprays

Temperature, K	800 – 1300 (reacting) 1000 (non-reacting & base case)
O_2 volume fraction, %	8 – 21 (reacting) 21 (base case) 0 (non-reacting case)
Density, kg/m^3	14.8
Injection pressure, MPa	150
Injection duration, ms	6.8
Injection mass, mg	17.8
Nozzle diameter, mm	0.1
Discharge coefficient (C_d)	0.8
Area contraction coefficient (C_a)	0.86

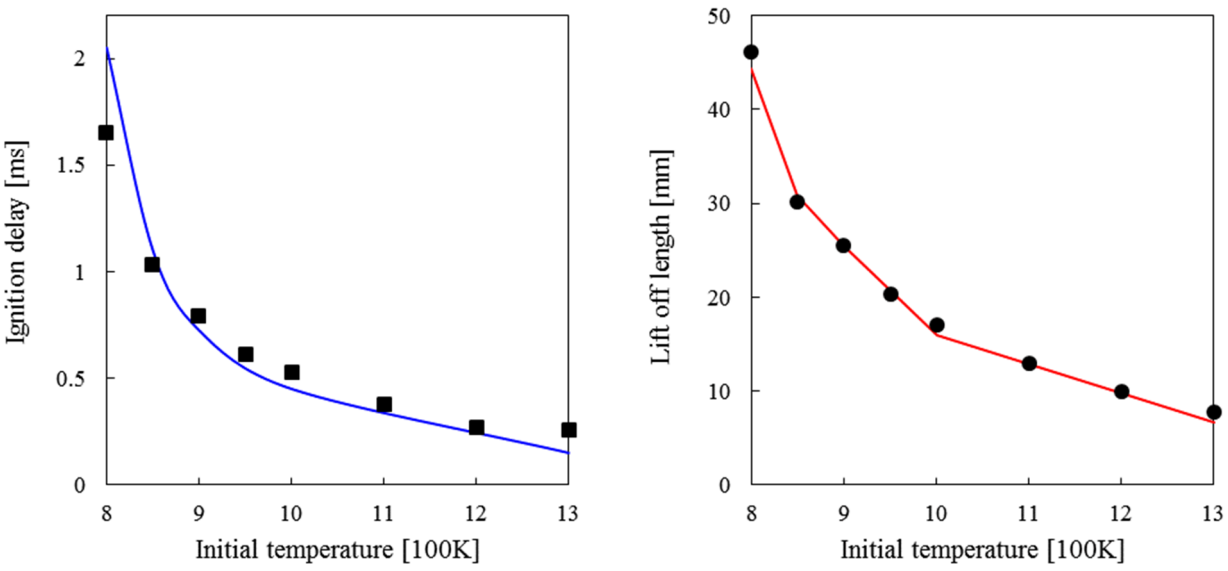

(a) (b)

Figure 16. Ignition delay and LOL versus initial temperature. Symbol represents experiment data. Line represents simulations.

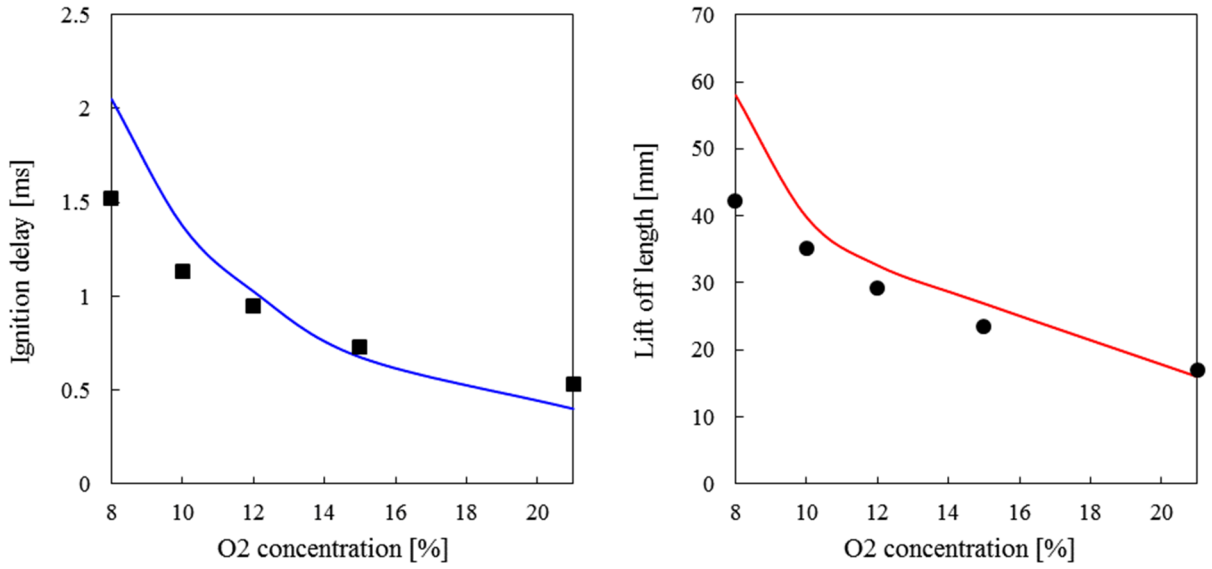

(a) (b)

Figure 17. Ignition delay and LOL versus O_2 concentration using a new criteria. Symbol represents experiment data. Line represents simulations.

3.6 COMPRESSION IGNITION ENGINE

Engine simulations are validated by comparing cylinder pressure and heat release rate profile with those for a light duty 1.9L 4-cylinder GM diesel engine obtained from Argonne National Laboratory [120]. The engine has a 7-hole common-rail injector in each cylinder. Simulations are performed for a 1/7 (51.43°) sector of the cylinder. The piston and cylinder walls temperatures including the head, and periodic boundaries at the front and back face of the sector are specified. The other engine geometry parameters, and the initial gas pressure and temperature are provided in Table 3. N-heptane is used as the diesel surrogate for chemistry calculation, while the physical properties of diesel fuel are considered when calculating vaporization and thermodynamics. Figure 18 compares the simulations and measurements in terms of pressure and heat release rate profiles. Simulations are shown for two base grid sizes corresponding to the minimum grid sizes of 0.25mm and 0.125mm. Good agreement can be observed for pressure profiles for both the grid sizes. However, the results using 0.125mm minimum grid size is closer to the experiment compared to that using 0.25mm. This provides confidence in the simulation since the power output is related to cylinder pressure. The predicted HRR profiles do not reproduced the experimentally observed decrease in heat release rate before ignition due to the vaporization. However, the general trends of these profiles obtained from the engine simulation show good agreement with experiment.

Table 3. Engine experiment parameters

Engine speed, rpm	1500
Engine bore diameter, mm	82
Engine stroke length, mm	90.4
Squish height, mm	0.6

Connecting rod length	145.4
IVC (intake valve closing), CAD	-132 ATDC
Gas temperature at IVC, K	310
Gas pressure at IVC, bar	1.1
EVO (exhaust valve opening), CAD	116 ATDC
SOI (start of injection), CAD	-0.5 ATDC
Fuel injection temperature, K	298
Nozzle diameter, mm	0.141
Injection Duration, CAD	8.5
Fuel intake temperature, K	298
Cylinder head temperature, K	450
Cylinder wall temperature, K	450
Piston wall temperature, K	450

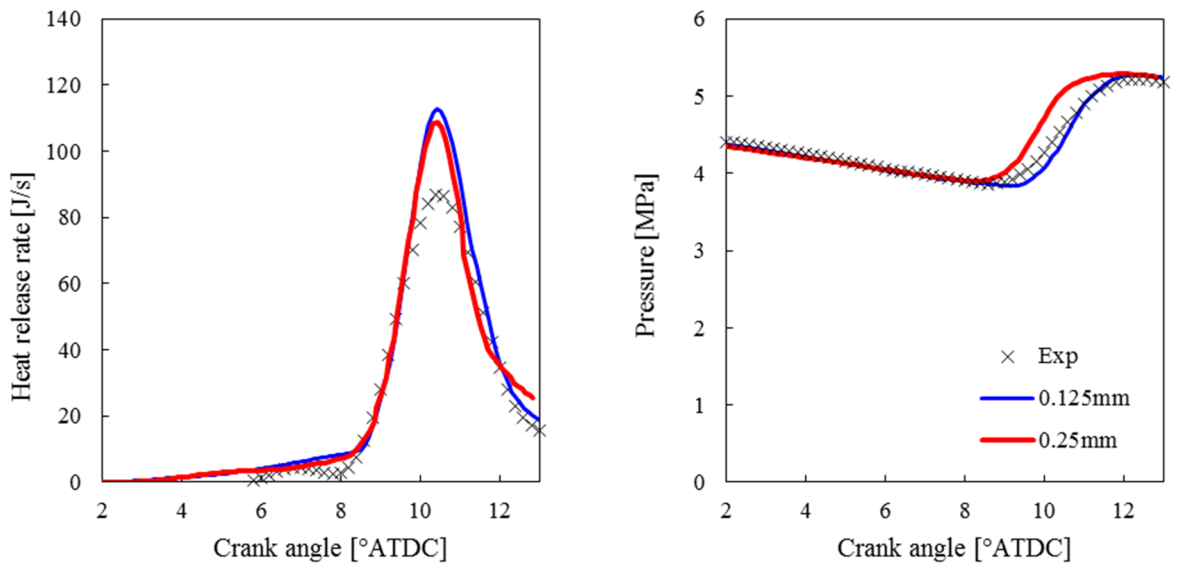

(a) (b)

Figure 18. Engine simulation and experimental results for heat release rate (a) and pressure (b) profiles. Symbol represents experiment data. Line represents simulation data using 0.125mm and 0.25mm as the minimum grid size.

4 COUNTERFLOW FLAME SIMULATION RESULTS AND DISCUSSION

(Previously published as Xiao Fu, Xu Han, Kenneth Brezinsky, Suresh Aggarwal, Effect of Fuel Molecular Structure and Premixing on Soot Emissions from n-Heptane and 1-Heptene Flames, Energy Fuels, 2013, 27 (10), pp 6262–6272, DOI: 10.1021/ef401409r; and Xiao Fu, Stephen Garner, Surresh Aggarwal, Kenneth Brezinsky, Numerical Study of NOx Emissions from n-Heptane and 1-Heptene Counterflow Flames, Energy Fuels, 2012, 26 (2), pp 879–888, DOI: 10.1021/ef2014315)

The first part of simulations results focus on the comparison of n-heptane and 1-heptene flames in a counterflow configuration. To study the effects of the unsaturated fuel structure, both diffusion and partially premixed flames are considered.

4.1 DIFFUSION FLAMES

To better understand the difference between the PPFs and diffusion flames (or non-premixed flame, NPF), one set of NPF analysis using n-heptane and 1-heptene is performed. Considering the initial conditions for PPFs, which will be discussed later, this simulation case is setup at a comparable condition. The strain rate is $a_G = 100s^{-1}$ and the carrier gas in the fuel stream is 17% nitrogen. The global strain rate is expressed as

$$a_G = \frac{2v_o}{L}\left(1+\frac{v_f\sqrt{\rho_f}}{v_o\sqrt{\rho_o}}\right) \tag{68}$$

Here L is the separation distance between the two nozzles. v_o is the oxidizer inlet velocity. v_f is the fuel inlet velocity. ρ_f and ρ_o are fuel and oxidizer densities, respectively. The fuel stream is introduced from the bottom nozzle (x=0cm) and the oxidizer form the top nozzle (x=1.5cm).

The fuel stream has a temperature of 400K and inlet velocity of 25cm/s. The oxidizer is air, entering at 300K and 37.5cm/s. These velocities are calculated by matching the inlet momentum.

The results of these NPFs are presented in Figure 19. The temperature profiles (Temp) and major species (fuels, O_2, CO, H_2 and CO_2) indicate very similar flame structure for the two fuels. Fuel is consumed rapidly near the stagnation plane (dashed vertical line) where a large amount of rich products such as CO and C_2H_4 are formed. The rich products of the fuel meet the air in the oxidizer side of the stagnation (about 0.2cm away above the stagnation plane) producing large amount of heat and through oxidation of CO and H_2. Less similarity can be observed in the profiles for minor species such as acetylene and benzene (C_6H_6). Compared to n-heptane flames, the 1-heptene flames produce greater amounts of acetylene and benzene, but smaller amounts of H_2 and C_2H_4. In particular, the mole fraction of benzene is significantly higher in 1-heptene flames than in n-heptane flames.

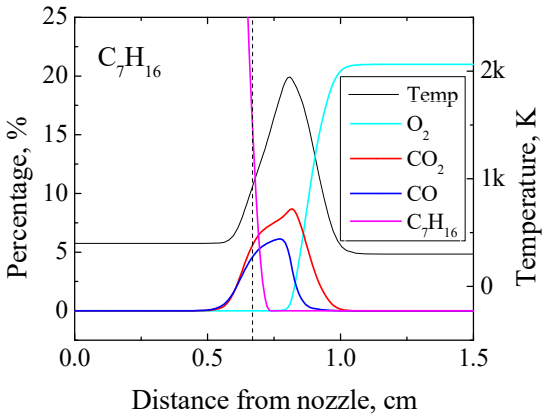

(a1)

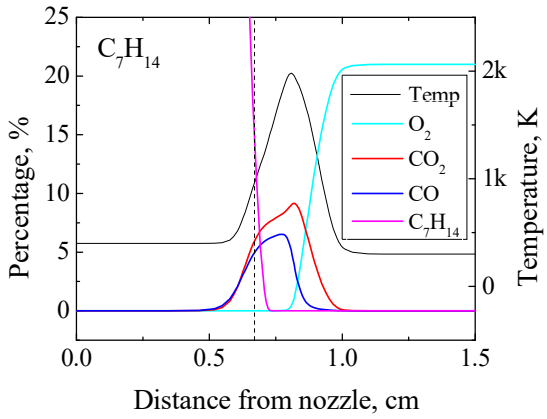

(b1)

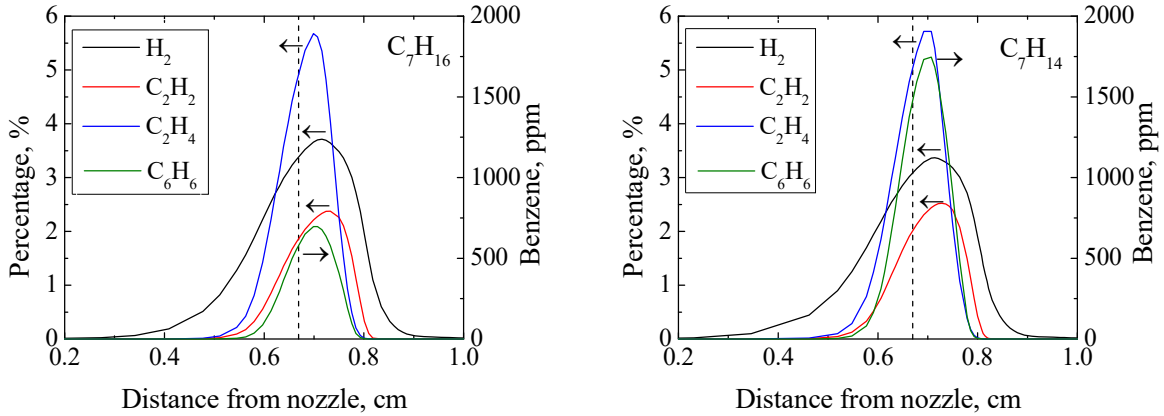

Figure 19. Flame structure in terms of temperature and species mole fraction profiles for n-heptane (a1, a2) and 1-heptene (b1, b2) nonpremixed flames ($\phi = \infty$) established at a_G = 100s^{-1} and nitrogen dilution of 17%. The dashed vertical line indicates the stagnation plane location.

4.2 PARTIALLY PREMIXED FLAME

To examine the effect of the partial premixing level on the flame structure, PPFs at different equivalence ratios are simulated. Table 4 lists the five flames in terms of equivalence ratio (ϕ) analyzed in the present study. Here ϕ = 2, 4, 8, 20 correspond to PPFs, while $\phi = \infty$ represents NPF. The ϕ is calculated based on the fuel and air in the fuel stream. The nitrogen dilution is kept at 17% for all the cases for consistency. The inlet velocities of the fuel and oxidizer streams are specified by matching the momentum of the two streams for given ϕ and a_G. Due to the difference in the molecular weight of n-heptane and 1-heptene, slight variation in fuel inlet velocities is necessary. However, this difference in the fuel inlet velocities is less than 0.3% between n-heptane and 1-heptene.

Table 4. Conditions for the five simulated n-heptane and 1-heptene flames

	ϕ	$\Phi=1-1/\phi$	Fuel/%	Air/%
1	2	0.5	3	80
2	4	0.75	6	77
3	8	0.88	11	72
4	20	0.95	23	60
5	∞	1	83	0

4.2.1 Partially Premixed Flame Structure

Figure 20 shows the comparison for n-heptane and 1-heptene PPFs with $\phi = 2$ in the fuel steam. The gaseous species, temperature, axial velocity and heat release rate (HRR) are presented in these figures. For both the fuels, the flame at $\phi = 2$ contains a double flame structure. The HRR profile contains two peaks. One peak corresponds to the rich premixed reaction zone (RPZ) on the fuel side and the other peak corresponds to the nonpremixed reaction zone (NPZ) located close to the stagnation plane. The RPZ is established downstream of the fuel inlet and characterized by high equivalence ratio, which results in the pyrolysis and partial oxidation of the fuel. The products of partial oxidation, such as CO, H_2, and C_2H_2, are transported to and consumed in the NPZ. The global flame structures for the two fuels are generally similar, implying that the overall combustion process is not strongly influenced by the presence of the unsaturated bond. However, more significant increase (about 280%) in benzene from RPZ when the fuel is changed from n-heptane to 1-heptene can be noticed compared to about 150% of that in NPF using both the fuels (cf. Figure 19). The increased benzene formation in 1-heptene PPF indicates a higher production rate of PAH and soot. In order to gain insight into the effect of unsaturated bond on soot formation and

oxidation processes, several soot properties are presented in Figure 20 (c) and (d). The soot properties include the average particle diameter, particle number density and soot volume fraction.

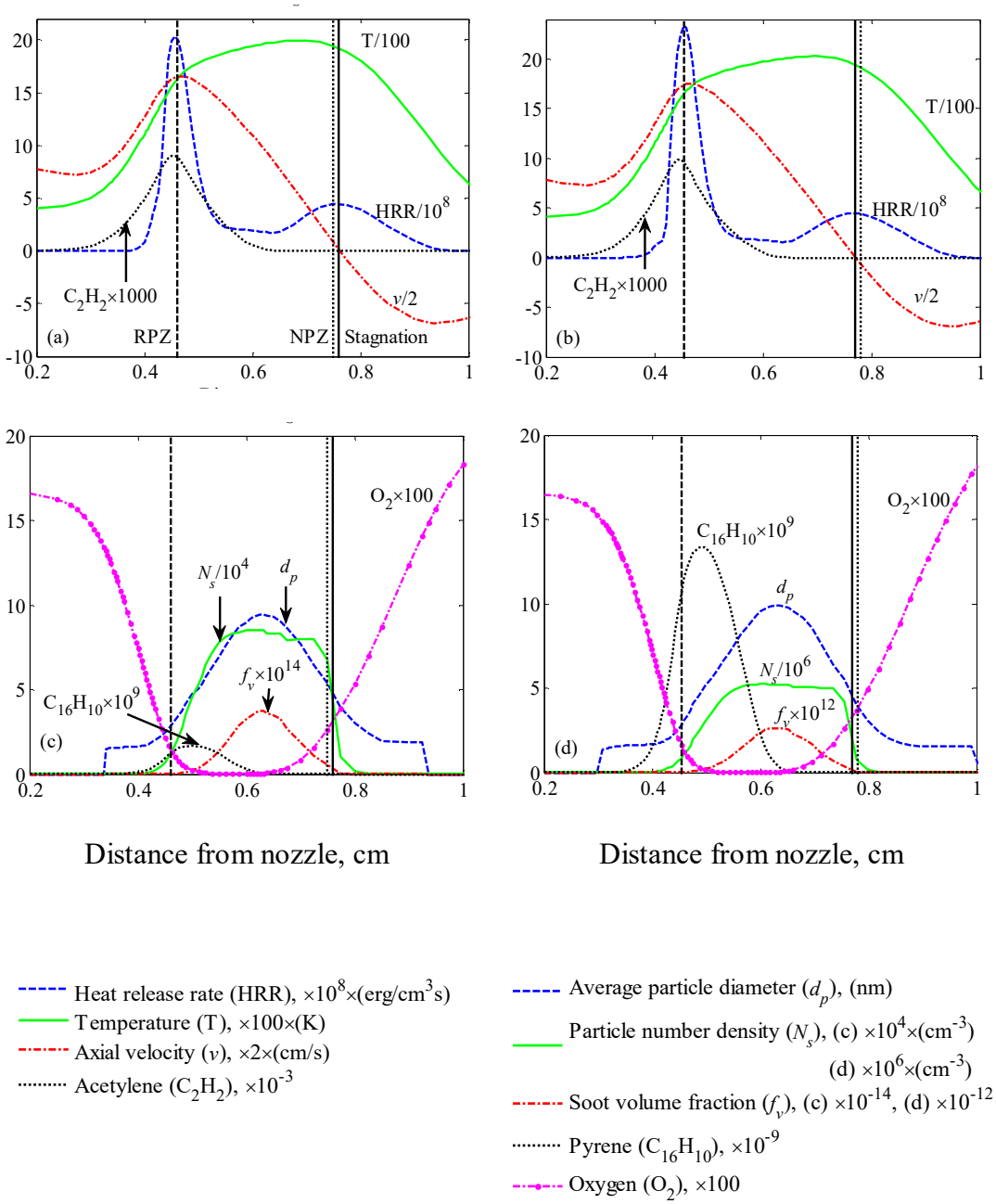

Figure 20. Flame structures of n-heptane and 1-heptene PPFs at $\phi = 2$, $a_G = 50s^{-1}$. Figs. (a) and (b) include temperature, heat release rate, axial velocity and acetylene mole fraction.

Figs. (c) and (d) include average particle diameter (d_p), particle number density (N_s), soot volume fraction (f_v), pyrene mole fraction and oxygen mole fraction. Vertical lines represent locations of the stagnation plane, rich premixed zone (RPZ) and non-premixed zone (NPZ), as noted in Fig. (a).

Figure 21 presents the computed structures of n-heptane and 1-heptene partially premixed flames (PPFs) at the same conditions as those for Figure 20, except that $\phi = 8$. Similar to the case for $\phi = 2$ (cf. Figure 20), the global flame structures for the two fuels are again similar, implying that the overall fuel oxidation and heat release processes are not strongly influenced by the presence of the unsaturated bond. However, the flame structure and soot formation are markedly influenced by the level of partial premixing, i.e., as ϕ is increased from 2 to 8. For the latter case, the RPZ is located very close to the stagnation plane, while the NPZ is located on the oxidizer side. The RPZ is also considerably weaker compared to the NPZ, where most of the heat release occurs. However, the concentrations of hydrocarbon species, especially PAHs, in the RPZ are significantly higher as ϕ is increased from 2 to 8. For instance, the peak pyrene mole fraction in n-heptane flame increases from 1.7×10^{-9} to 1.9×10^{-6} as ϕ is increased from 2 to 8, and this can be attributed to two factors. One is the effect of ϕ, which increases the concentration of hydrocarbon species due to their reduced oxidation rate. The other factor is the increased residence time since RPZ is now located near the stagnation plane. Thus the peaks in acetylene and pyrene profiles are located close to the stagnation plane. Consequently, the peaks in particle number density and soot volume fraction profiles are also located near the stagnation plane, and their values are considerably higher compared to those for $\phi = 2$. The O_2 profiles indicate relatively little soot oxidation for this case compared to that for $\phi = 2$, since the soot particles formed near NPZ are pushed away from this zone towards the stagnation plane. Moreover, there is little oxygen in this region. Thus for the

PPFs investigated in this study, the soot emission is predominantly due to nucleation and surface growth, with the latter caused by surface reactions and coagulation, while the amount of soot oxidation depends upon the level of partial premixing. Another important observation from Figure 20 and Figure 21 is that while the amount of soot produced is still noticeably higher in 1-heptene flame compared to that in n-heptane flame at all equivalence ratios, the effect of double bond becomes less pronounced at higher ϕ.

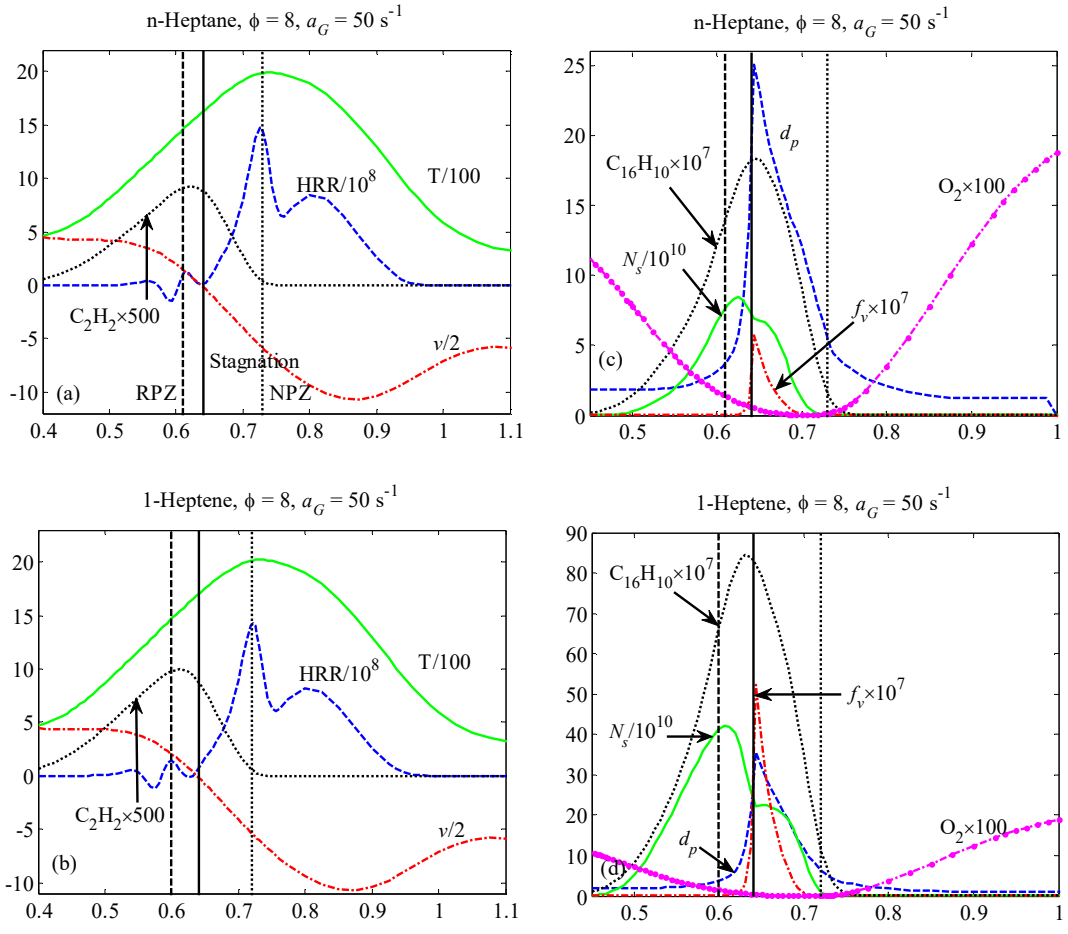

Distance from nozzle, cm

Distance from nozzle, cm

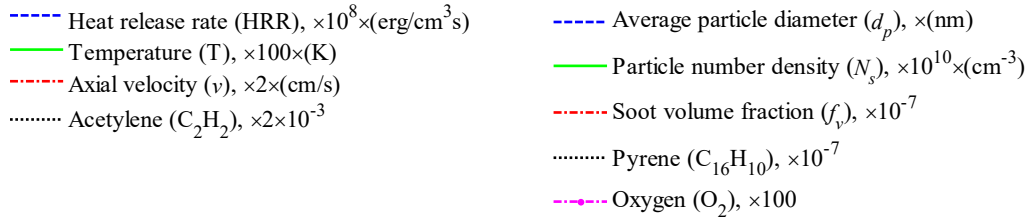

Figure 21. Flame structures of n-heptane and 1-heptene PPFs at $\phi = 8$, $a_G = 50s^{-1}$. Figs. (a) and (b) include temperature, heat release rate, axial velocity and acetylene mole fraction. Figs. (c) and (d) include average particle diameter (d_p), particle number density (N_s), soot volume fraction (f_v), pyrene mole fraction and oxygen mole fraction. Vertical lines represent locations of the stagnation plane, rich premixed zone (RPZ) and non-premixed zone (NPZ), as noted in Fig. (a).

Significantly higher amount of pyrene in 1-heptene flame can be noticed compared to that in n-heptane flame in the RPZ and region between RPZ and stagnation plane. The particle number density profiles indicate that nucleation is initiated with the formation of pyrene. Subsequently, the particle diameter and soot volume fraction continue to increase over the distance due to surface reactions and coagulation. The number density, which is determined by a competition between nucleation and coagulation, also increases in this region. As a consequence, the soot number density and volume fraction are both noticeably higher in 1-heptene flames compared to those in n-heptane flames. These differences can be attributed to the increased amounts of acetylene, propargyl, benzene and pyrene, and are related to the presence of double bond in 1-heptene. Consequently, as further studies show (not presented here), the differences between 1-heptene and n-heptane flames in particle diameter, number density and soot volume fraction are significantly

higher with higher a_G. Thus, the effect of double bond is more pronounced at lower ϕ and higher a_G

4.2.2 Effect of the Fuel Molecular Structure in PPFs

A commonly used way to compare the emission characteristics of the two fuels is through an emission index. For instance, the NO emission index is defined as:

$$EINO = \frac{\int_0^L MW_{NO}\dot{\omega}_{NO}dx}{-\int_0^L MW_{Fuel}\dot{\omega}_{Fuel}dx} \tag{69}$$

Here MW represents the molecular weight, $\dot{\omega}$ the reaction rate, L the separation distance between the two nozzles, and x the axial coordinate. Figure 22 presents emission indices of NO and benzene plotted versus $\Phi = 1\text{-}1/\phi$. The use of parameter Φ facilitates to represent the entire equivalence ratio range from $\phi = 2$ ($\Phi = 0.5$) to $\phi = \infty$ ($\Phi = 1$) analyzed in this study. The EINO decreases as the level of partial premixing is reduced, or ϕ is increased. However, the EINO for 1-heptene is higher than that for n-heptane, and the difference decreases as ϕ is increased, indicating that the effect of fuel chemical structure on NO formation becomes less noticeable for diffusion flames compared to that for partially premixed flames. The difference between the two fuels are also decreased in EIC_6H_6 for both fuels, though the actual values of EIC_6H_6 are increased as ϕ is increased. This effect of partial premixing has been discussed in previous publications[9,10].

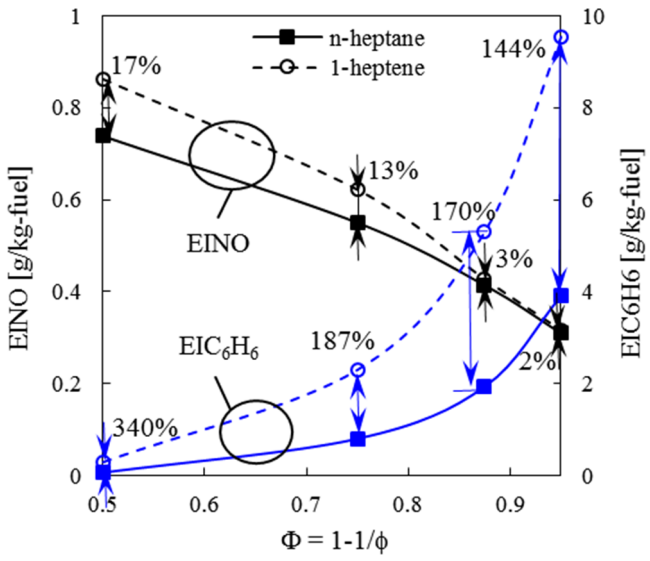

Figure 22. Emission indices of NO and benzene plotted versus Φ = 1-1/ϕ, where Φ from 0.5 to 1.0 corresponds to the five cases listed in Table 4. The differences between the emission indices of both the fuels are marked in percentage.

Even though the trade-off relationship of NO and benzene at different ϕ can be noticed, the unsaturated fuel (1-heptene) consistently produces larger amounts of NO and benzene compared to n-heptane. The reason can be attributed to the difference in the fuel molecular structures. Long chain saturated hydrocarbons such as n-heptane have lower probability to undergo β scission, since the absence of double bond leads to a more uniform distribution of electrons among all the bonds. The presence of a double bond in unsaturated hydrocarbons promotes β scission reactions leading to higher acetylene formation, which results in higher NO formation through prompt NO route[121,122]. The prompt NO mechanism is driven by the CH radical formed from acetylene during combustion[121], then leads to the formation of NO. Key reactions involved are listed here.

$$CH + N_2 \rightarrow NCN \text{ (or HCN)} + H \text{ (or N)} \quad (70)$$

$$CH_2 + N_2 \rightarrow HCN + NH \quad (71)$$

$$C + N_2 \rightarrow NCN \quad (72)$$

The first reaction dominates this sequence and produces NCN and H which can yield NO through the following reactions:

$$NCN + O \rightarrow N + NCO \quad (73)$$

$$NCN + H \rightarrow HCN + N \quad (74)$$

$$NCN + H \rightarrow N + H_2 \quad (75)$$

$$NCO + O \rightarrow CN + NO \quad (76)$$

$$N + OH \rightarrow NO + H \quad (77)$$

An alternative route through the formation of HCN[123] also depends on acetylene being the dominant source of CH_2 that leads to the formation of CH as does a pathway involving HCNN.[122] Additionally, the evidence of acetylene being the dominant source of CH_2 under rich combustion conditions has been provided by the rate of production analysis[124] for n-heptane partially premixed flames[125]. Consequently, the presence of acetylene in the pyrolysis products can be used as an indicator of how different fuel structures may potentially affect NO levels. The presence of a double bond in unsaturated hydrocarbons such as 1-heptene promotes β scission reactions leading to higher acetylene formation.

4.2.3 Contributions of Various NO Formation Routes

As discussed in previous studies,[76,77,100,126] the prompt NO is a major contributor to the total NO_x for long chain hydrocarbons, such as n-heptane. In order to examine the relative contributions of various NO routes, simulations were performed for each of the four NO routes, namely, the

thermal, prompt, N_2O intermediate, and NNH routes.[76,77] For instance, the thermal NO_x route includes the following reactions:

$$N_2 + O \rightarrow N + NO \quad (78)$$

$$N + OH \rightarrow NO + H \quad (79)$$

$$N + O_2 \rightarrow NO + O \quad (80)$$

The initiating reaction for thermal NO formation is Reaction 14. Similarly, particular reactions associated with prompt NO include: $CH + N_2 \rightarrow HCN + N$, $CH_2 + N_2 \rightarrow HCN + NH$, $C + N_2 \rightarrow CN + N$, $NH_2 + N \rightarrow N_2 + H + H$, $NH_2 + NO \rightarrow N_2 + H_2O$, $NH + NH \rightarrow N_2 + H + H$, $NCO + N \rightarrow N_2 + CO$, $N_2O + CO \rightarrow N_2 + CO_2$, $NCO + NCO \rightarrow CO + CO + N_2$, $NCO + NO \rightarrow N_2 + CO_2$.

Reactions associated with the N_2O intermediate sub-mechanism include: $N2 + O + M \rightarrow N_2O + M$, $N_2O + H \rightarrow N_2 + OH$, $N_2O + O \rightarrow N_2 + O_2$, $N_2O + OH \rightarrow N_2 + HO_2$.

Similarly reactions associated with the NNH sub-mechanism are: $NNH + NO \rightarrow N_2 + HNO$, $NNH \rightarrow N_2 + H$, $N_2 + H_2 \rightarrow NNH + H$, $NNH + NH_2 \rightarrow N_2 + NH_3$, $NNH + OH \rightarrow N_2 + H_2O$, $NNH + NH \rightarrow N_2 + NH_2$, $NNH + O_2 \rightarrow N_2 + H + O_2$, $HNNO + M \rightarrow N_2 + OH + M$, $NH + N \rightarrow N_2 + H$, $NH + NO \rightarrow N_2 + OH$, $NNH + O_2 \rightarrow N_2 + HO_2$.

In order to compute the contribution of each NO formation route, five sets of simulations were performed as listed in Table 4. Figure 23 presents the NO profiles computed by using the complete NO mechanism and by summing the contributions of the four NO routes. In general, the total NO from the summation of the four routes exceeds that obtained using the complete NO mechanism, with the largest discrepancy (~15%) occurring near the stagnation plane for the 1-heptene PPF at ϕ =2. This is consistent with the results reported in previous studies[76,77], and may

be attributed to the fact that removing certain reactions associated with a given NO sub-mechanism may affect the mole fractions of species involved in another NO sub-mechanism. Overall, the total NO obtained by summing the contributions of various NO routes is fairly close to that obtained using the complete NO mechanism.

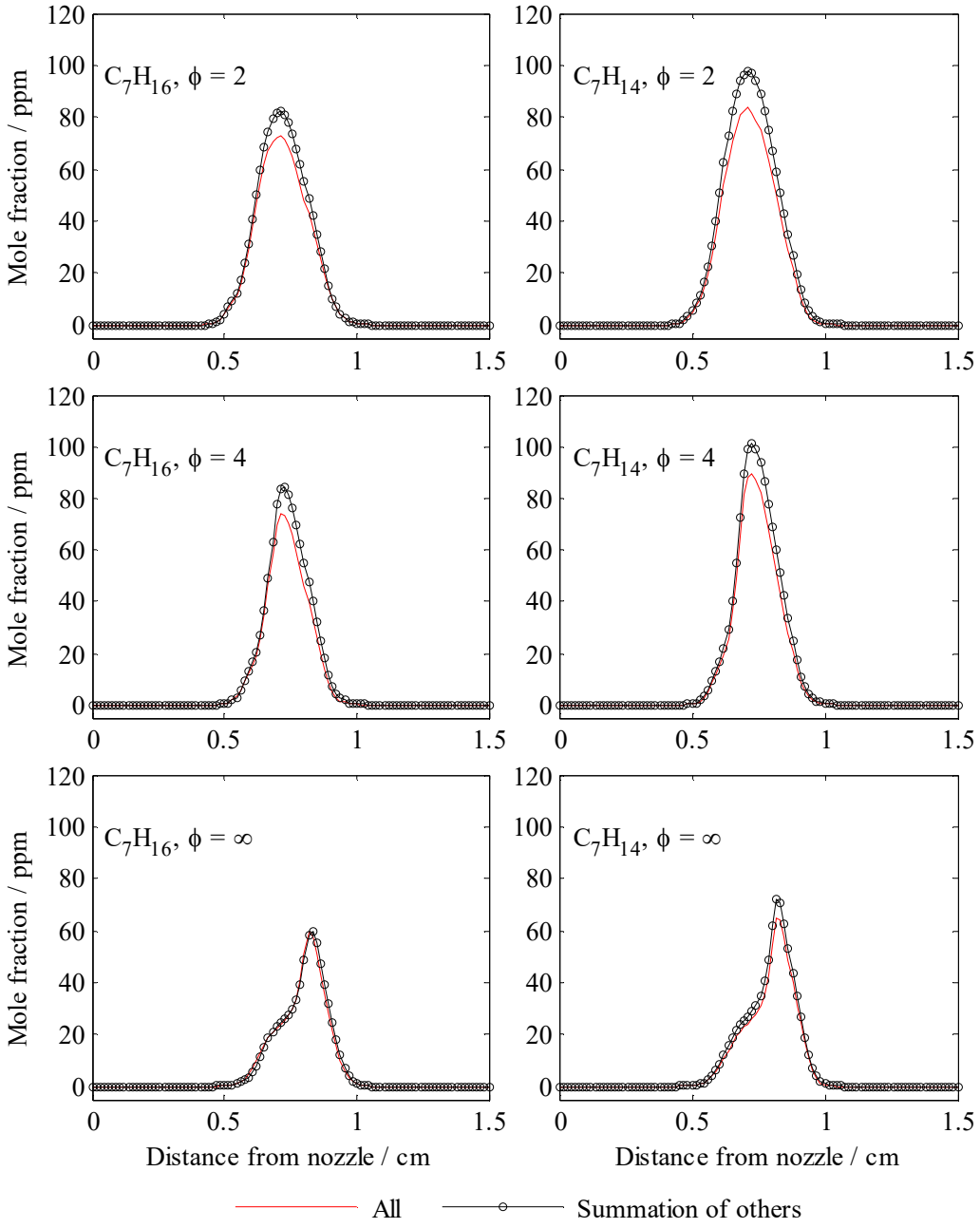

Figure 23. NO mole fraction profiles computed using the complete NO mechanism (red solid lines) and by summing the contributions of the thermal, prompt, NNH, and N_2O intermediate routes (black lines with circle symbols). Results are shown for n-heptane and 1-heptene flames at $\phi = 2$, 4 and ∞.

Figure 24 presents NO profiles computed using the total NO, thermal NO, and prompt NO mechanisms for n-heptane and 1-heptene flames at ϕ = 2 and 4. Results indicate that the contribution of thermal NO to the total NO is relatively small in these flames. In addition, as ϕ is increased, the contribution of thermal NO decreases, while that of prompt NO increases. The comparison of the relative contributions of the four sub-mechanisms is presented in Figure 25, which plots the NO profiles for the complete NO mechanism, and for four sub-mechanisms for n-heptane and 1-heptene flames at ϕ = 2, 4 and ∞. The peak NO values and peak temperature for each of these mechanisms are also listed in Table 5. In addition, the peak NO values for the various mechanisms are shown in Figure 26. These results indicate that the prompt NO provides the largest contribution to the total NO in these flames, followed by the intermediate N_2O, NNH, and thermal NO mechanisms. Thus the prompt NO contributes 28-37% and 33-46% in n-heptane and 1-heptene flames, respectively, depending upon the level of partial premixing. The corresponding values for other three mechanisms are 12-18% and 12-20% the for intermediate N_2O, 15-29% and 17-32% for the NNH, 2-12% and 4-18% for the thermal in n-heptane and 1-heptene flames, respectively. Another important observation is that the relative contribution of prompt NO to total NO is higher in 1-heptene flames compared to that in n-heptane flames. Finally it should be noted from Table 5 that the flame temperature for 1-heptene is typically 30-40K higher than that for n-heptane, which partly contributes to the increased NO for 1-heptene.

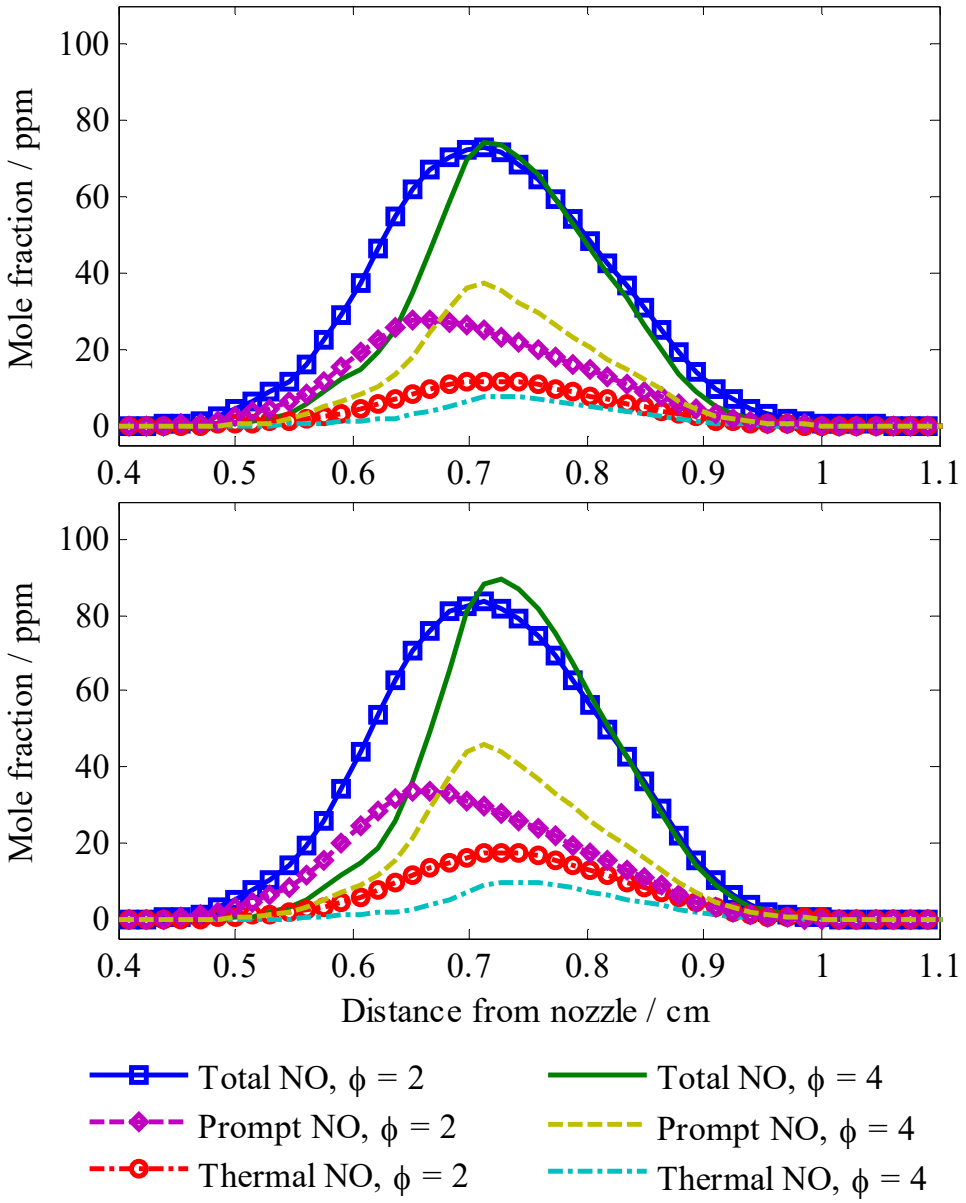

Figure 24. NO profiles computed using the complete NO, the thermal NO, and the prompt NO mechanisms for n-heptane and 1-heptene flames at ϕ = 2 (symbols) and ϕ = 4 (lines).

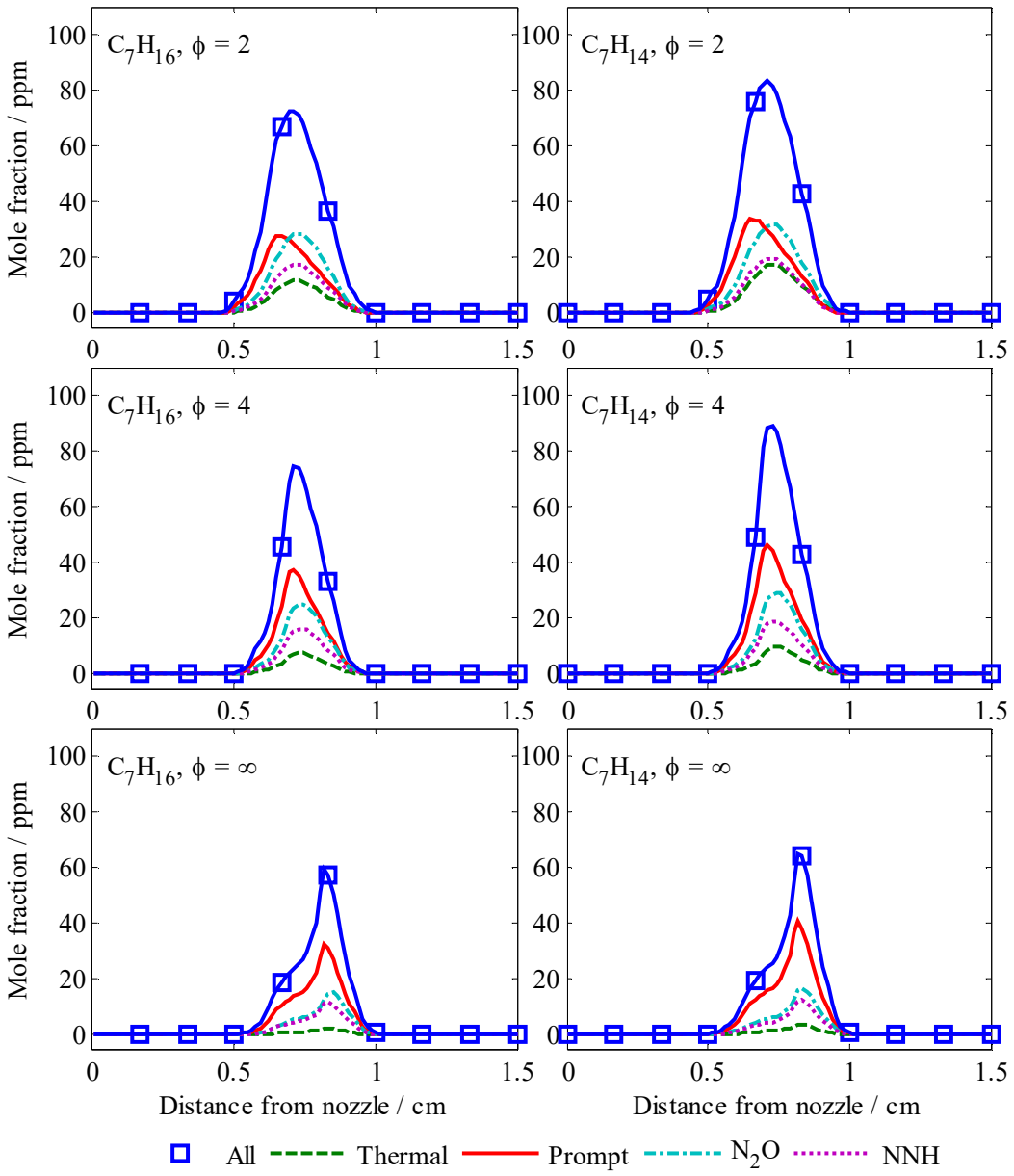

Figure 25. NO profiles computed using the complete NO_x mechanism, and using the thermal, prompt, N2O intermediate, and NNH sub-mechanisms for n-heptane and 1-heptene flames established at ϕ = 2, 4 and ∞. Blue Solid line with square symbols represents the complete NO_x mechanism, while the dashed, solid, dash dot, and dot lines represent the thermal, prompt, N_2O intermediate and NNH sub-mechanisms respectively.

Table 5. Peak flame temperature and peak NO (given in ppm and %) formed with the complete NO mechanism, and through the thermal, prompt, N_2O intermediate, and NNH routes for the three n-heptane and 1-heptene flames at different equivalence ratios.

Variable	n-Heptane Flames			1-Heptene Flames		
Equivalence ratio	ϕ=2	ϕ=4	ϕ=∞	ϕ=2	ϕ=4	ϕ=∞
Peak temperature (K)	1967	1948	1945	1993	1987	1981
Total NO (ppm)	72.7	74.3	59.5	83.5	89.3	65.0
Thermal NO (ppm)	11.8 (16%)	7.7 (10%)	2.4 (4%)	17.5 (21%)	9.8 (11%)	3.9 (6%)
Prompt NO (ppm)	27.8 (38%)	37.1 (50%)	32.4 (54%)	33.7 (40%)	46.0 (51%)	40.7 (63%)
N_2O Intermediate NO (ppm)	28.6 (39%)	25.2 (34%)	15.2 (26%)	32.1 (38%)	29.3 (33%)	16.6 (26%)
NNH Intermediate NO (ppm)	17.6 (24%)	16.3 (22%)	11.6 (19%)	19.5 (23%)	19.0 (21%)	12.3 (19%)

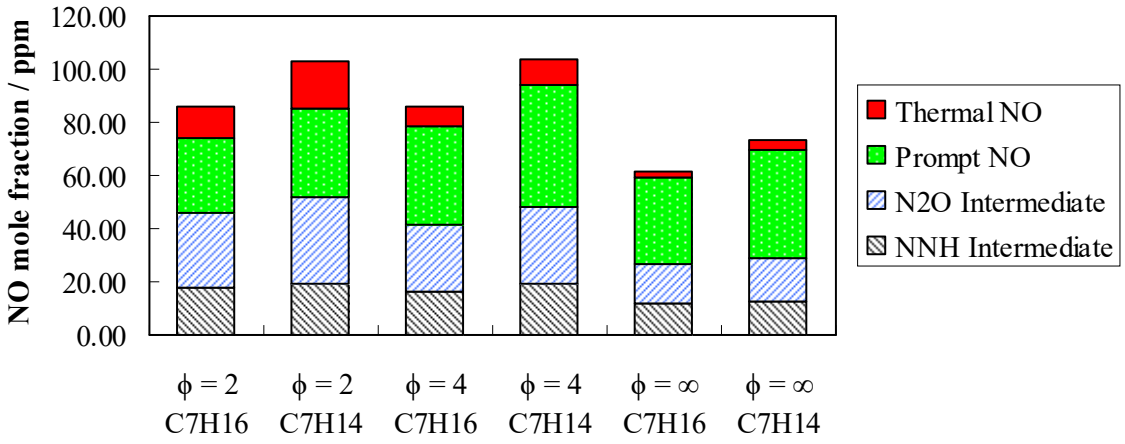

Figure 26. Contribution of each sub-mechanism to total NO in terms of the peak NO mole fraction for n-heptane and 1-heptene flames at ϕ = 2, 4 and ∞.

4.2.4 Effect of the Fuel Molecular Structure on Soot Formation

Moreover, unsaturated fuels produce higher amounts of hydrocarbons, such as acetylene, propargyl (C_3H_3) and benzene, resulting in increased PAHs emissions, such as naphthalene, phenanthrene and pyrene. As a consequence, the soot number density and volume fraction are also noticeably higher in 1-heptene flames compared to those in n-heptane flames. These differences can be attributed to the increased amounts of acetylene, propargyl, benzene and pyrene, and are related to the presence of double bond in 1-heptene. The increased soot emission as a consequence of double bond in the fuel molecular structure is related to the higher nucleation and surface growth rates, which are due to the increased production of pyrene and acetylene in 1-heptene flames compared to that in n-heptane flames. The nucleation process in the present soot model is represented by

$$2\ C_{16}H_{10} \Rightarrow 32\ C + 20\ C_{soot}\text{-}H + 28.75\ C_{soot}\bullet \qquad (81)$$

In this reaction, two pyrene molecules combine to form one soot nucleus containing 32 C atoms. The C_{soot}-H is a carbon atom site with surface-bonded hydrogen atom, while the C_{soot}• is an open (or empty) surface site. The surface site density is defined as the number of active chemical sites per surface area where adsorption, desorption, and chemical reaction can take place. Here 20 of the C atoms have H surface sites and about 28.75 of the 32 C atoms are open sites. The C_{soot}-H and C_{soot}• sites then react with gaseous species through surface growth reactions R12-R15, as described by the HACA (hydrogen abstraction, acetylene addition) mechanism. The particle number density is determined by the competition between the nucleation and coagulation processes, while the soot particle diameter and volume fraction are determined by the coagulation and surface reaction rates. As discussed by Frenklach[83], the coagulation of soot particles is based on Smoluchowski's theory of Brownian motion[81], and proportional to the square of total particle

number, while the surface growth is modeled through the HACA mechanism, represented by reactions:

$$H + C_{soot}\text{-}H <=> C_{soot}\bullet + H_2 \quad (82)$$

$$C_{soot}\text{-}H + OH <=> H_2O + C_{soot}\bullet \quad (83)$$

$$C_{soot}\bullet + H => C_{soot}\text{-}H \quad (84)$$

$$C_{soot}\bullet + C_2H_2 => C_{soot}\text{-}H + 2C + H \quad (85)$$

As indicated, acetylene, H and OH are the gaseous species involved in this mechanism. In reaction R15, an acetylene molecule attaches to the $C_{soot}\bullet$ site and forms C_{soot}-H and H. In addition, two carbons are added to the carbon bulk. Finally, the soot oxidation is determined by the following reaction:

$$OH + C_{soot}\bullet + C <=> C_{soot}\text{-}H + CO \quad (86)$$

As a conclusion of the first session, partially premixed or non-premixed counterflow flames burning n-heptane and 1-heptene are compared. The unsaturation of the fuel molecular structure pronounces a large amount of acetylene and propargyl formed through β scission reactions, therefore results in high NO and soot formation.

As discussed in previous studies[18, 127] unsaturated fuels produce higher amounts of hydrocarbons, especially C_2H_2, C_3H_3, and C_6H_6, resulting in increased PAHs emissions. This is supported by the simulation results presented in Figure 20 and Figure 21, which indicate significantly higher pyrene concentration in 1-heptene flame compared to that in n-heptane flame. As a consequence, the soot number density and volume fraction are also noticeably higher in 1-heptene flames compared to those in n-heptane flames. These differences can be attributed to the increased amounts of C_2H_2, C_3H_3, C_6H_6, and $C_{16}H_{10}$, and are related to the presence of double bond

in 1-heptene. This is illustrated more clearly in Figure 27 and Figure 28, which plot the peak values of PAHs and soot properties for different flame conditions for the two fuels. As indicated in Figure 27, at any given ϕ and a_G, the peak mole fractions of C_2H_2, C_6H_6 and pyrene are noticeably higher in 1-heptene flames compared to those in n-heptane flames. Consequently, as indicated in Figure 28, the particle diameter, number density and soot volume fraction are significantly higher in 1-heptene flames compared to those in n-heptane flames. Moreover, the effect of double bond is more pronounced at lower ϕ and higher a_G, except that the difference in particle diameter between two fuels is higher in $\phi = 8$ flames compared to $\phi = 2$ flames. Thus as the level of partial premixing is increased, or as the strain rate is increased, the effect of double bond on PAHs and soot emissions becomes more pronounced. Note however, that the PAHs and soot emissions are noticeably reduced as the strain rate and/or the level of partial premixing is increased.

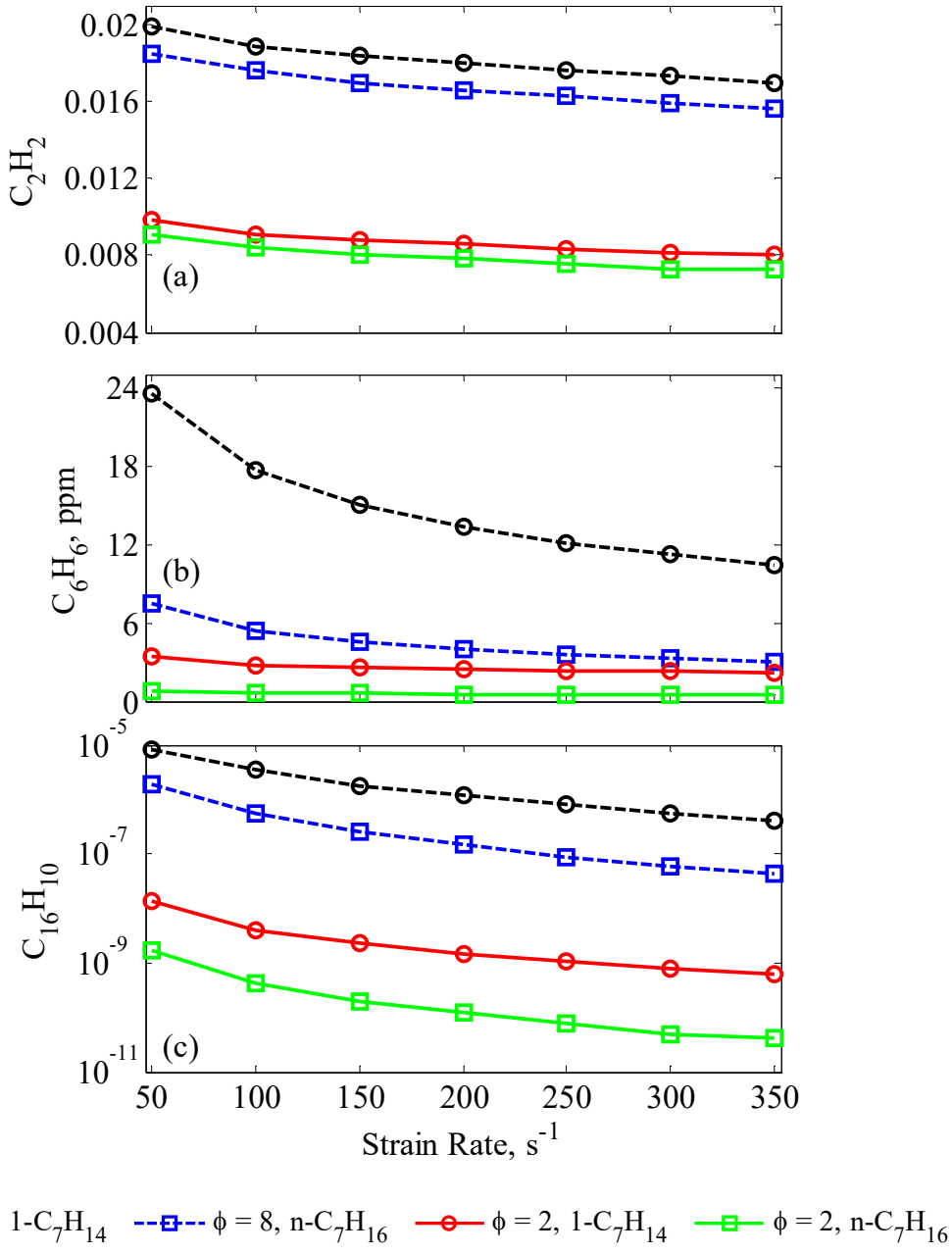

Figure 27. Peak mole fractions of acetylene (C_2H_2), benzene (C_6H_6) and pyrene ($C_{16}H_{10}$) plotted versus strain rate for n-heptane and 1-heptene PPFs at ϕ = 2 and 8. Note that pyrene is plotted on a log scale.

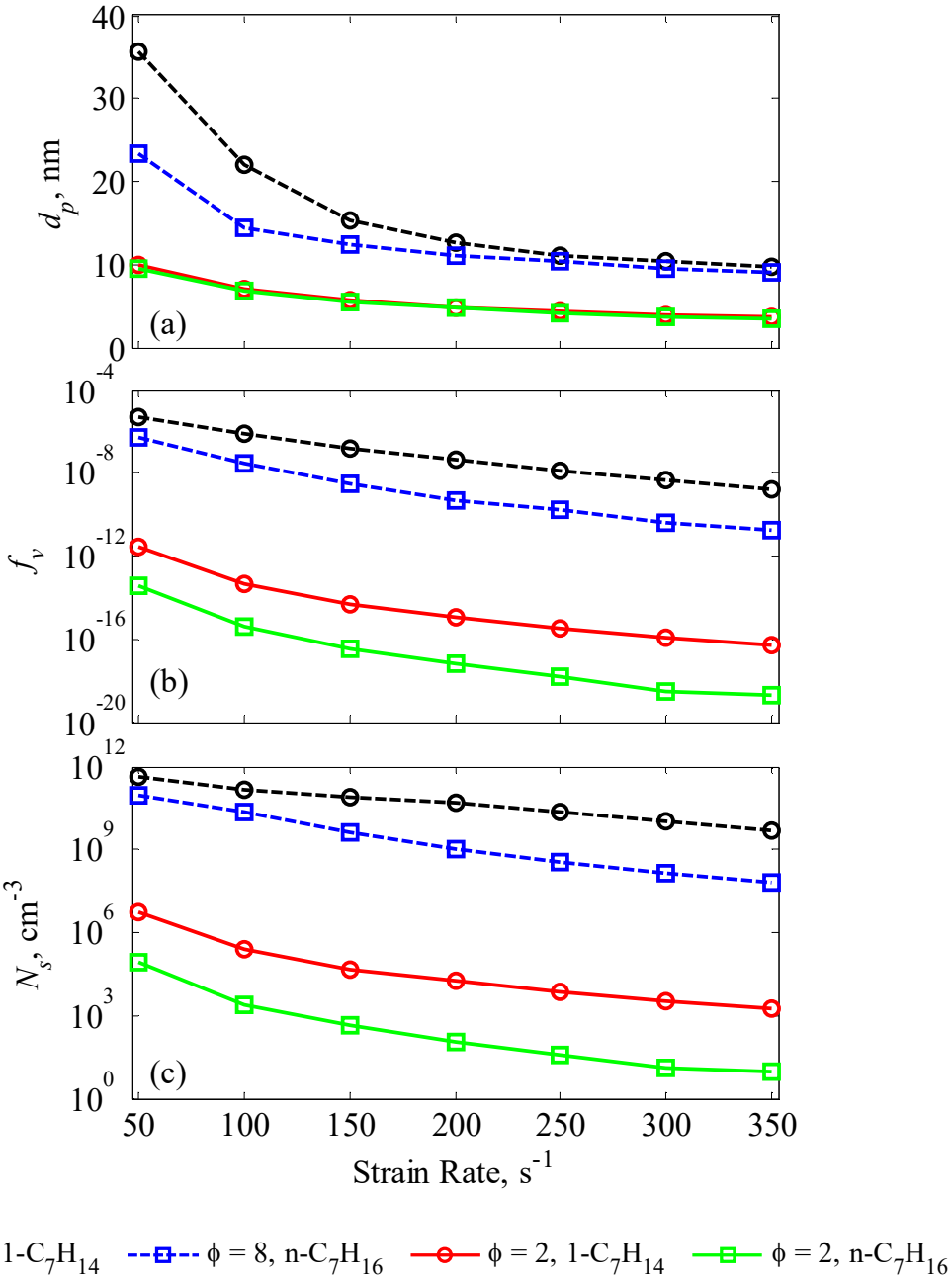

Figure 28. Peak soot diameter (Fig. a), number density (Fig. b), and volume fraction (Fig. c) plotted versus strain rate for n-heptane and 1-heptene PPFs at ϕ = 2 and 8. Note that the number density and volume fraction are plotted on a log scale, and soot diameter is plotted on a linear scale.

The effect of strain rate on soot emissions is illustrated in Figure 29, which presents the profiles number density and soot particle diameter in in n-heptane PPFs at $a_G = 50s^{-1}$ and $350s^{-1}$, and ϕ=2. The HRR profiles are also included to indicate the RPZ and NPZ locations. As expected, the HRR increases at higher strain rates due the higher fuel flow rate. In additions, with the increase in strain rate, the separation between the RPZ and NPZ decreases, since the RPZ moves further away from fuel nozzle, and is established at a location where the strained premixed flame speed matches with the local flow velocity. The NPZ location, which is close to the stagnation plane, is not much affected by the change in strain rate. More importantly, as the strain rate is increased, the soot number density and particle diameter decrease noticeably due to the reduced residence time at higher strain rates. The soot volume fraction exhibits similar behavior with respect to the strain rate, and is therefore not shown. Similarly, the soot properties profiles for 1-heptene flames are not shown, as these profiles were qualitatively similar to those for n-heptane flames, although there was significantly higher soot production in 1-heptene flames, as discussed earlier. In summary, while the presence of double bond causes a significant increase in soot emissions in PPFs, the effect is more noticeable at low strain rates. For instance, for the conditions investigated, there is little soot formation at strain rates higher than $350s^{-1}$.

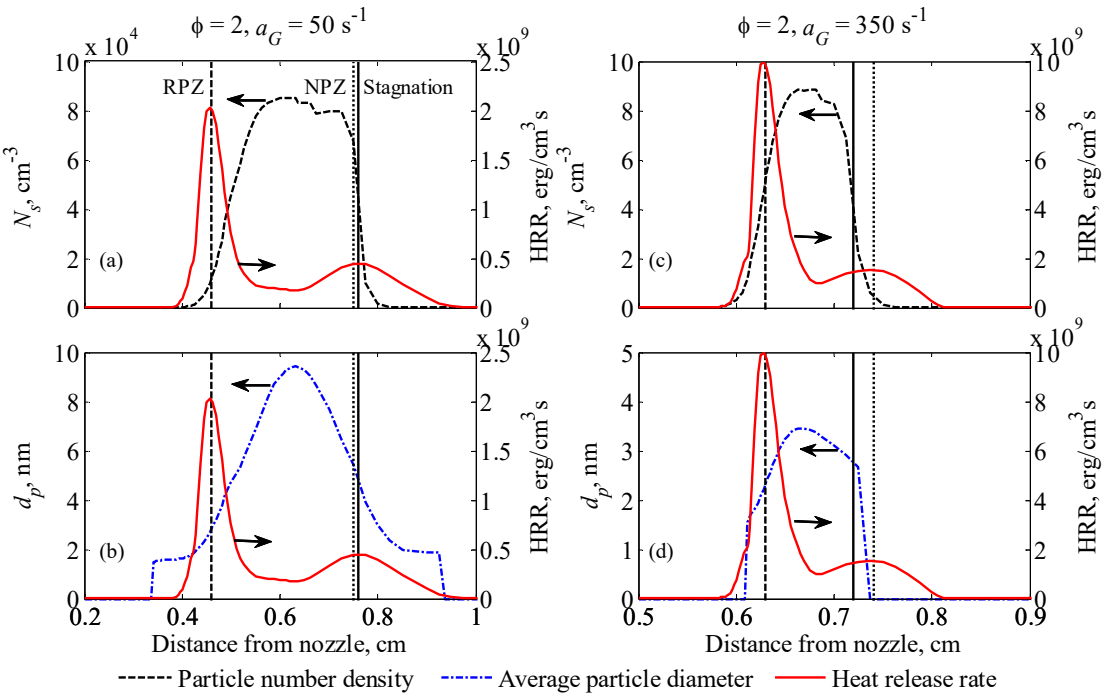

Figure 29. Effect of strain rate on soot emission in n-heptane PPF. Profiles of particle number density, N_s, (Figs. a and c) and particle diameter, d_p, (Figs. b and d) for PPFs at ϕ = 2, and strain rates of 50s^{-1} (Figs. a and b) and 350s^{-1} (Figs. c and d). Heat release rate (HRR) profiles are also shown (solid line). Vertical lines represent locations of the stagnation plane, rich premixed (RPZ) and nonpremixed reaction zones (NPZ), as noted in Fig. (a).

4.2.5 Reaction Path Analysis for PAH Formation in PPFs

As discussed in the preceding sections, there is significantly higher PAH and soot production in 1-heptene flames than in n-heptane flames. Since C_2H_2 and C_6H_6 are the major precursors for soot, an analysis was performed to identify the dominant pathways for their formation in these flames. The analysis considered a region between the RPZ and stagnation plane, where most of the PAHs and soot are formed. Results are presented in Figure 30, which

summarizes the major pathways for C_2H_2 and C_6H_6 formation in n-heptane and 1-heptene flames at ϕ=2.0 and strain rate of $50s^{-1}$. While the oxidation of the two fuels follows different paths, benzene is mainly formed through the recombination reaction of propargyl (C_3H_3) radicals[128]. Most of C_3H_3 is formed from allyl radical (C_3H_5), and its formation from fuel decomposition is quite different for the two fuels, as can be seen in Figure 30. At high temperatures (>1200K), typical of flame environment, most of 1-heptene directly decomposes into C_3H_5 and C_4H_9, as a consequence of the β scission reaction due to the presence of double bond in 1-heptene[1]. In contrast, the decomposition of n-heptane mostly leads to the formation of various alkyl radicals, such as CH_3, C_6H_{13}, C_2H_5, C_5H_{11}, C_3H_7 and C_4H_9, via the C-C bonds scission, most of which then decompose to produce C_2H_4 and CH_3 (not shown) through β scission and H abstraction reactions. In addition, the butyl (C_4H_9) formed from 1-heptene also decomposes to produce C_2H_4, which is the main path for the formation of ethylene in 1-heptene flame (cf. Figure 30b), while there are multiple alkyl species (C_6H_{13}, C_5H_{11}, C_4H_9, C_3H_7, etc.) that form ethylene in n-heptane flame (cf. Figure 30a). Consequently, the ethylene concentration is higher in n-heptane flames compared to that in 1-heptene flames, as indicated in Figure 31a. Ethylene subsequently forms vinyl (C_2H_3), which produces additional benzene through its reaction with 1,3-butadiene (C_4H_6). Note however, that higher C_2H_4 concentration does not imply increased benzene production in n-heptane flames, since the butadiene concentration is much lower in this flame compared to that in 1-heptene flames (cf. Figure 31b). The latter is due to the fact that the formation of allyl competes with that of butadiene in n-heptane flames, unlike the case for 1-heptene flames, in which the path to butadiene is preferred. The above pathway from fuel to benzene formation as well as the observations

[1]Note the presence of the double bond strengthens the adjacent C-C bond (β bond), while making the next C-C bond or C-H bond weaker.

regarding the importance of allylic radicals, propargyl, vinyl, and butadiene are consistent with previous studies; see, for example Zhang et al.[129,130] who examined the chemistry of aromatic precursor formation in n-heptane premixed flames, and Han et al.[127] who analyzed the effect of fuel unsaturation on the formation of C_2H_2 and C_6H_6 in triple flames.

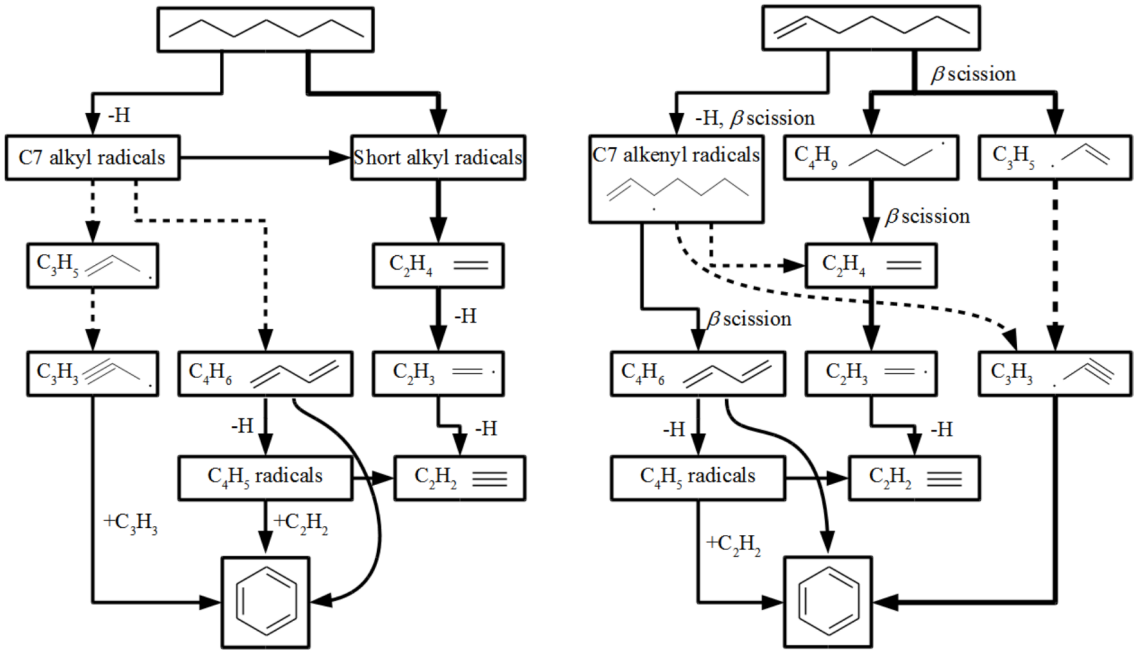

(a) n-heptane (b) 1-heptene

Figure 30. Dominant acetylene and benzene formation paths in n-heptene (a), and 1-heptene (b) established at ϕ=2.0 and strain rate of 50s^{-1}. Arrows with dashed lines indicate multiple reactions.

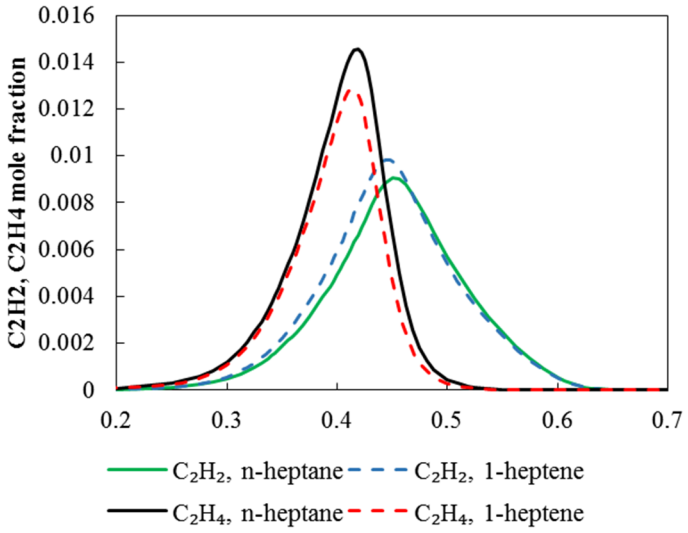

(a)

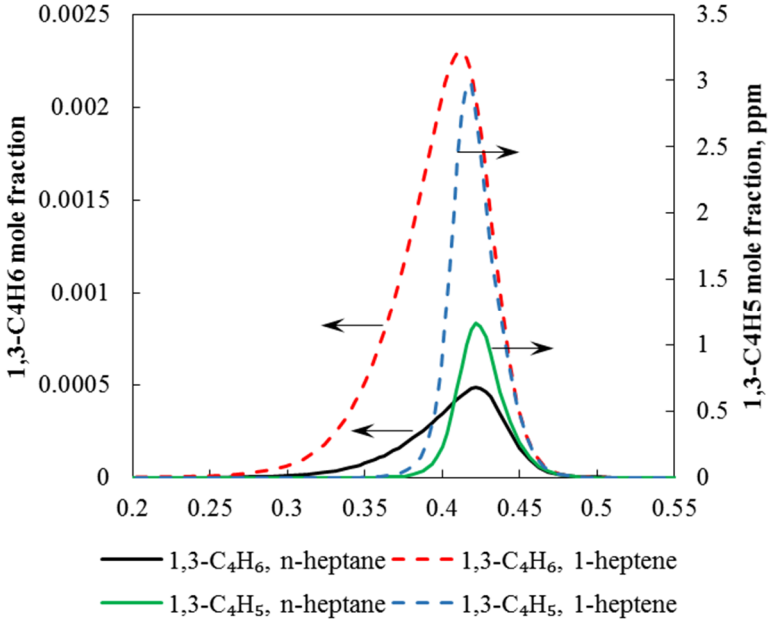

(b)

Figure 31. Comparison of C_2H_2 and C_2H_4 profiles (a), and 1,3-C_4H_6 and 1,3-C_4H_5 profiles (b) in n-heptane (solid lines) and 1-heptene (dashed lines) partially premixed flames at $\phi = 2$, $a_G = 50s^{-1}$.

Furthermore, it is important to mention that the presence of double bond also leads to the increased production of C_2H_2 in 1-heptene flames than in n-heptane flames. As indicated in Figure 30, C_2H_2 is mainly formed from vinyl, and produces benzene through its reaction with C_4H_5 radical, which is formed from butadiene. While the concentration of C_2H_4 is higher in n-heptane flames, as noted above, that of C_2H_2 is higher in 1-heptene flames. This is due to the fact that C_2H_2 is produced from both C_2H_4 (through vinyl) and C_4H_5 (which breaks down to form C_2H_2 and C_2H_3), and C_4H_5 concentration is noticeably higher in 1-heptene flames (cf. Figure 31b), leading to the increased production of C_2H_2 in these flames. Acetylene subsequently plays an important role in the formation of larger PAH species through the HACA (hydrogen abstraction acetylene addition) mechanism. In summary, the presence of double bond in unsaturated hydrocarbon (1-heptene) promotes β scission reactions leading to the increased production of C_2H_2 and C_6H_6, and thereby higher pyrene and soot emissions.

A pathway analysis was also performed for the formation of pyrene, which is considered as the major nucleating species for soot formation. As indicated in Figure 32, for both the fuels, benzene is a major precursor for pyrene ($C_{16}H_{10}$) formation. Once the first aromatic ring is formed, it undergoes multiple routes, preferably through phenyl (C_6H_5) radical and styrene (C_8H_8) to form phenylacetylene (C_8H_6). Then two phenylacetylene molecules can form pyrene and H_2. Another major pyrene formation path is from shorter chain alkene and alkenyl such as C_5, C_4 and C_2 species. These can form cyclopentadienyl radical (C_5H_5). Then two cyclopentadienyls can produce H_2 and naphthalene ($C_{10}H_8$), while the latter can subsequently form acenaphthylene ($C_{12}H_8$) through HACA reactions. Finally one acenaphthylene reacts with one propargyl (C_3H_3) to form half the pyrene and half the phenanthrene ($C_{14}H_{10}$). However, the pyrene formation through

cyclopentadienyl route is significantly less important compared to the benzene route. Other pyrene formation paths in the flame condition are even less important than cyclopentadienyl route, and are not shown. As noted earlier, benzene is more pronounced in 1-heptene flames, making the benzene route the most significant pyrene formation path in 1-heptene flames. Thus the increased formation of pyrene can be related to the higher concentrations of C_2H_2 and C_6H_6.

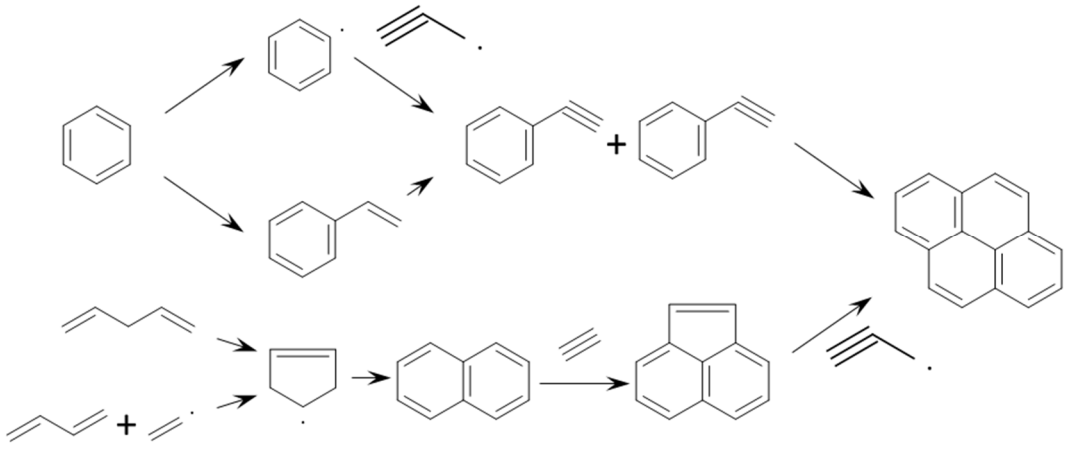

(a) n-heptane

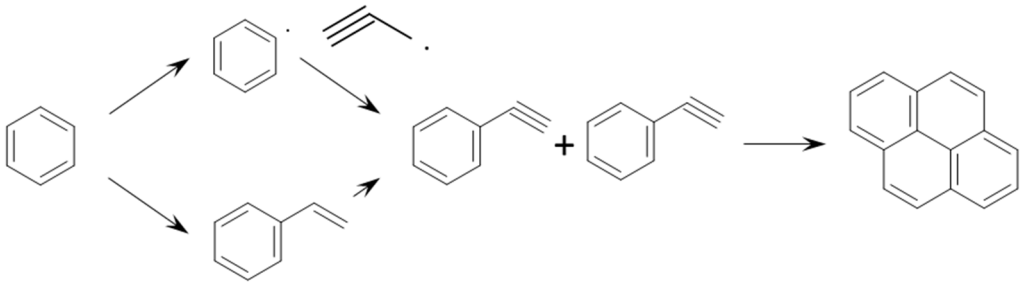

(b) 1-heptene

Figure 32. Dominant pyrene formation path in n-heptane (a) and 1-heptene (b) flames

5 SPRAY COMBUSTION SIMULATION RESULTS AND DISCUSSION

(Previously published as Xiao Fu, Suresh Aggarwal, Fuel unsaturation effects on NO_x and PAH formation in spray flames, Fuel, 2015, 160, 1-15, DOI: 10.1016/j.fuel.2015.07.075)

In this session, results are presented for n-heptane or 1-heptene spray flames in a constant volume combustion chamber described in the previous chapter (3.4). Simulations are carried out using the reduced mechanism developed in this work. Results in this chapter focus on: (a) n-heptane or 1-heptene spray flame structures, (b) the comparison of NO_x formation in n-heptane and 1-heptene flames, and (c) the comparison of PAH formation from n-heptane and 1-heptene combustion.

5.1 LIQUID SPRAY COMBUSTION FLAME STRUCTURE

The n-heptane spray flame case with initial temperature 1000K and 21% O_2 is analyzed to explain the detail of the physical and chemical processes in the constant volume reactor. Figure 33 presents the time evolution of the temperature contours at the center cut plane. The black lines represent the equivalence ratio ranging from 0.15 to 3. The equivalence ratio, ϕ, is determined by all species containing H, C and O except CO_2 and H_2O:

$$\phi = \frac{2\sum_i N_i \eta_{C,i} + \frac{1}{2}\sum_i N_i \eta_{H,i}}{\sum_i N_i \eta_{O,i}} \tag{87}$$

where i is all species except CO_2 and H_2O, N_i is the number of moles of species i and $\eta_{C,i}$, $\eta_{H,i}$ and $\eta_{O,i}$ are the number of carbon (C), hydrogen (H) and oxygen (O) atoms, respectively, for species i. These equivalence ratio contours are good indicators to monitor the reaction zones. Note

that only the center part (0.04m × 0.1m) of the computational domain (0.108 m × 0.108m) of the constant volume reactor is shown.

The processes of fuel injection, spray development, fuel-air mixing and ignition can be discerned from the contour plots at 0.3 and 0.5ms. For instance, region within ϕ=3 contour at 0.3ms indicates a fuel-rich zone characterized by pre-ignition pyrolysis and oxidation reactions. Subsequently, the ignition occurs at 0.5ms, as indicated by the high-temperature region between x=30mm and x=40mm. Note that the measured ignition delay time in Sandia experiments for the same conditions was 0.53ms. The ignition process is more clearly depicted in Figure 34, which presents the heat release rate (HRR) contours (left) and scatter plots in ϕ-T space (right) at three different times. Such scatter plots have previously been used to visualize the soot and NO_x formation regions in IC engines, and also to provide insight into the ignition process[119]. The blue contours and scatter plots in Figure 34 depict regions of negative HRR, indicating pre-ignition endothermic reactions. Moreover, prior to ignition event (at t=0.4ms), the peak HRR is only 10^{11}J/s-m^3, and located at T≈900K and ϕ≈4 in the scatter plot at t=0.4ms. However, at t=0.5ms, a small region of high HRR can be visualized in the ϕ-T plot near ϕ=2.5 and T=1200K, indicating the occurrence of ignition. Subsequently, a wide region with significant heat generation can be seen in both the contour and scatter plots at 0.6ms, indicating self-sustained combustion with T>1200K and $0.1<\phi<5$. The combustion process is more clearly indicated in Figure 33 by the ϕ and T contours at t=0.7 and 1.1ms. It is characterized by distinct regions of rich premixed combustion and diffusion combustion. For the present case, the rich premixed zone (RPZ) is indicated by region corresponding to $2<\phi<5$ and 2000K<T<2500, while the diffusion or non-premixed zone (NPZ) corresponds to $0.15<\phi<2.5$ and high temperatures (2500K<T<2800) due to exothermic reactions forming CO_2 and H_2O species. The green vertical lines at x=17mm in Figure

33 mark the measured flame LOL, which matches with the predicted LOL indicated by the contours at t=0.7 and 1.1ms.

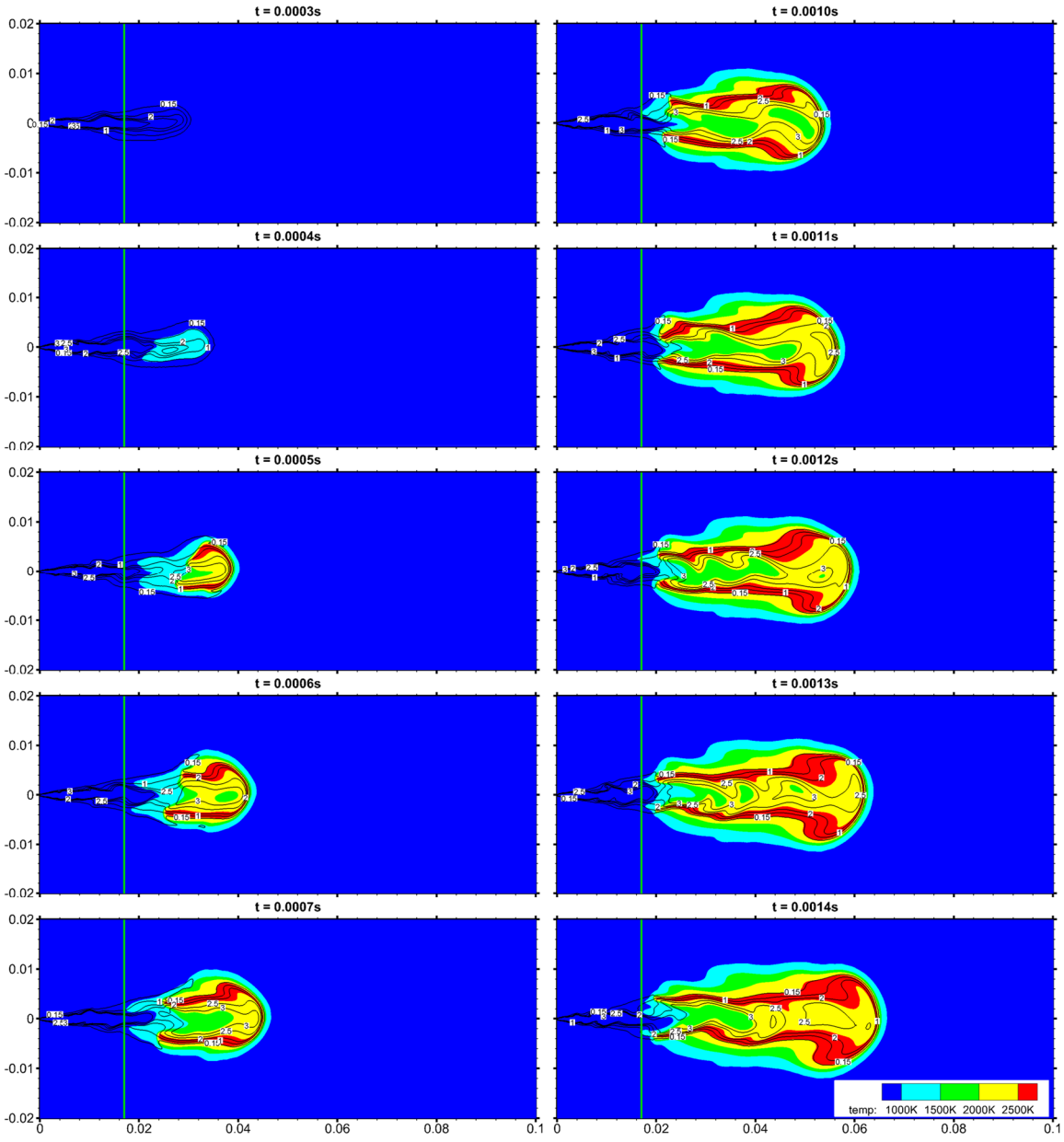

Figure 33. Mixture fraction and temperature contours at different times showing the temporal evolution of n-heptane spray flame. Color indicates the temperature range between 1000-2500K. Contour lines represent mixture fraction or equivalence ratio ranging from 0.15 to 3. Initial temperature=1000K. Dimensions are in m.

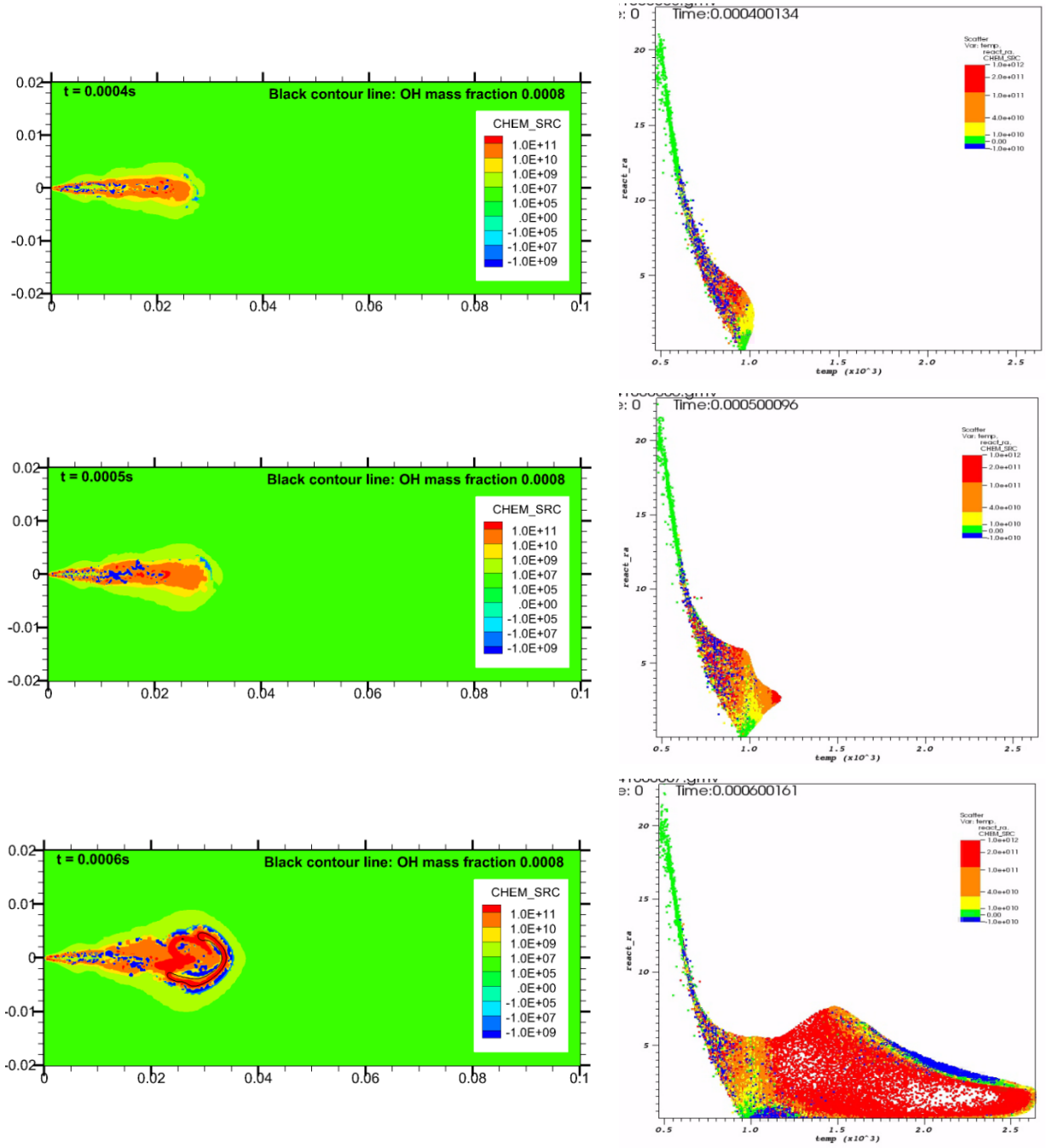

Figure 34. Heat release rate (J/s-m^3) contours (left) and scatter plots in ϕ-T space (right) at three different times. Heat release rate ranges between -1x10^9 to 1x10^{11} for contour plots and between -1x10^{10} to 1x10^{12} for scatter plots.

Figure 35 presents the integrated fuel vapor mass and HRR profiles with respect to time. The two-stage ignition process can be clearly seen from the HRR profile. The first increase in HRR at 0.2ms is related to the 1st-stage ignition while the second sharp increase at 0.5ms pertains to the 2nd-stage ignition, followed by the rich premixed combustion and the diffusion combustion. The rich premixed combustion is also indicated by the sharp decrease in n-heptane mass between 0.5 and 0.8ms, while the diffusion combustion is indicated by more moderate and nearly constant rate of decrease of n-heptane mass. The RPZ and NPZ can be distinguished more clearly in Figure 36, which presents C_2H_2, OH, NO, and C_6H_6 mass fraction contours. As indicated, the RPZ and NPZ are characterized, respectively, by the high concentrations of C_2H_2 and OH species. In addition, most of NO is formed in the NPZ where temperatures are high, while benzene (C_6H_6) is formed in the RPZ.

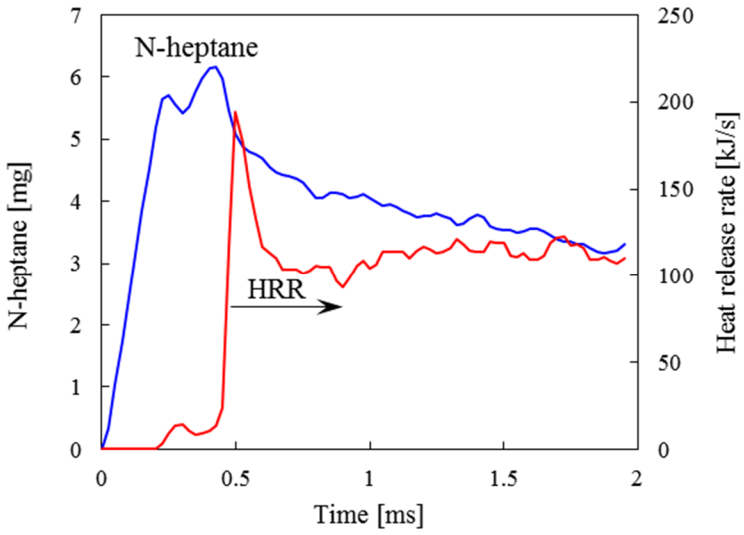

Figure 35. Integrated n-heptane vapor mass and heat release rate profiles with respect to time.

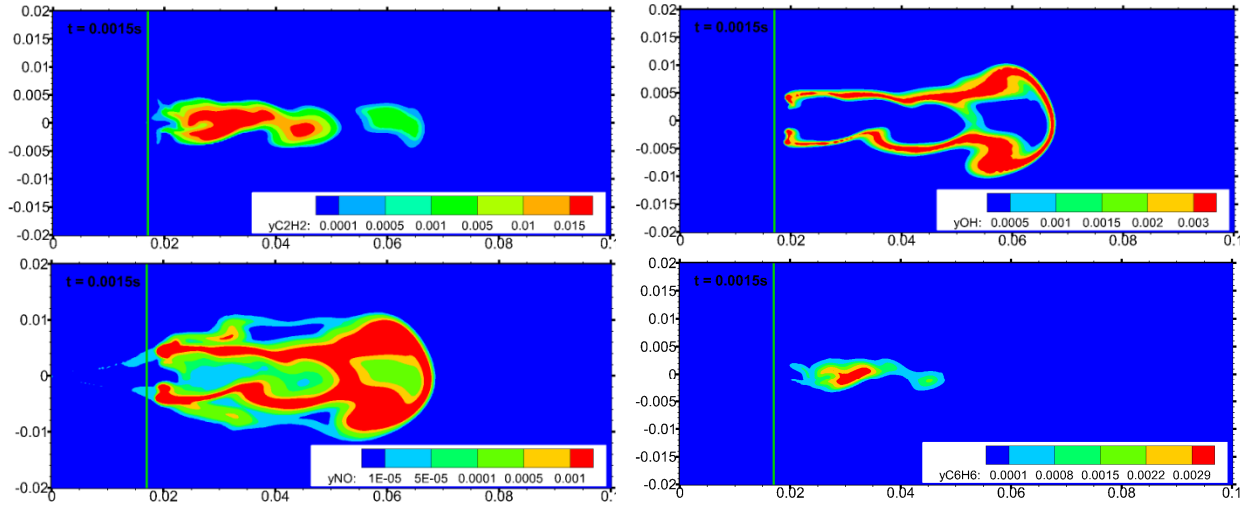

Figure 36. C_2H_2, OH, NO, and C_6H_6 mass fraction contours in n-heptane spray flame at t=1.5ms.

In order to identify the relative contributions of various NO_x (NO and NO_2) formation routes, Figure 37 presents contour plots for the mass fractions of NO, NO_2, HCN, NH, N_2O and NNH. Note that HCN and NH species are important for prompt NO, while N_2O and NNH species are associated with NO formed through the N_2O intermediate and NNH intermediate routes, respectively. As can be seen in Figure 37a, most of NO is formed in NPZ, with a relatively a small amount also being formed in RPZ and the region outside NPZ. The NO formed in NPZ is predominantly through the thermal NO route since temperatures are the highest (2600K to 2900K) there. In indicated in Figure 37b, most of NO_2 is formed in the region outside NPZ, where temperature is about 1500K and abundant amount of O_2 is present. The prompt NO is mainly formed in RPZ as indicated by the HCN and NH contours in Figure 37c and d, respectively. Finally, N_2O is formed in the lean region outside the NPZ similar to NO_2, (cf. Figure 37e), while NNH is formed in the region between the RPZ and NPZ (cf. Figure 37f), implying that NNH intermediate route is important there.

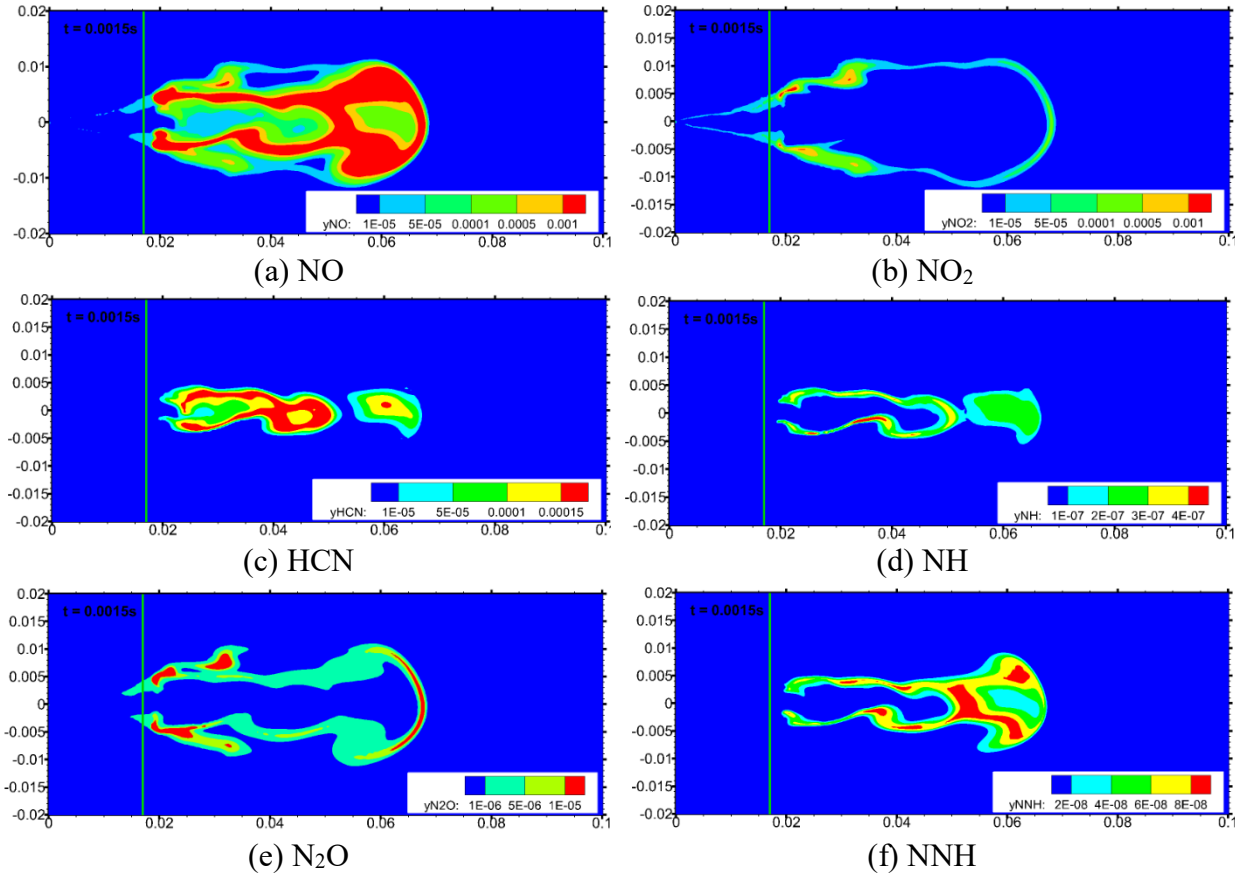

Figure 37. Mass fraction contours for NO, NO_2, HCN NH, N_2O, and NNH in the constant volume reactor for n-heptane spray flame. Initial ambient temperature=1000K.

5.2 EFFECT OF FUEL MOLECULAR STRUCTURE ON NO FORMATION

In order to characterize the effect of fuel molecular structure or unsaturation on NO and PAH emissions, n-heptane and 1-heptane spray flames were simulated at identical conditions in the Sandia reactor. Figure 38 presents the temporal variations of peak temperature and integrated NO mass for the two flames. Note that at typical autoignition temperatures (800-1000K) in diesel engines, 1-heptene has much longer ignition delays than n-heptane. Consequently, simulations were performed with an initial temperature of 1300K. At this temperature, ignition delays for the two fuels are nearly the same (≈0.2ms), as indicated in Figure 38. These values also compare well

with the measured value of 0.26ms in Sandia experiments. More importantly, the peak temperature for 1-heptene flame is 2870K compared to a value of 2840K for n-heptane flame. Consequently, 1-heptene flame produces more NO compared to n-heptane flame. For example, at t=1.4ms, the total NO in 1-heptene flame is 18% higher than that in n-heptane flames, and the difference can be mostly attributed to increased thermal NO in 1-heptene flame.

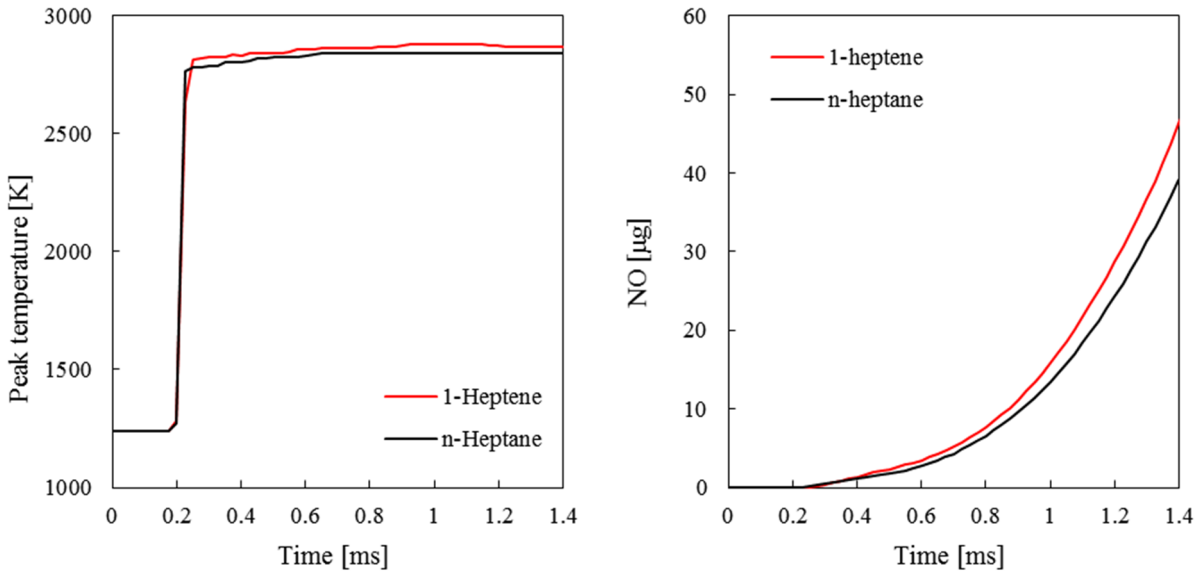

Figure 38. Peak temperature and total NO mass versus time for n-heptane (black) and 1-heptane (red) spray flames. Initial temperature is 1300K.

Since temperature is the important factor for thermal NO, the increased NO in 1-heptene flame can be attributed to higher peak temperature in this flame. Note that the heating value of 1-heptene is (LHV=44.66MJ/kg) is slightly lower than that of n-heptane (44.92MJ/kg). Thus the higher peak temperature in 1-heptene flame is not related to the heating value, but to the fuel oxidation chemistry. In order to examine this aspect, homogeneous reactor simulations were performed at similar conditions. Figure 39 presents the reaction path analysis for the two fuels, based on constant volume simulations with initial conditions similar to those for spray flames, i.e.,

T=1300K, p=55atm, ϕ=1. At these conditions, oxidation routes are significantly different for the two fuels. As indicated in Figure 39a, the dominant path for n-heptane is through H abstraction reaction forming alkyl radicals. Here the more prominent reaction is C_7H_{16}+ OH=> H_2O+C_7H_{15}. A relatively small amount of n-heptane (12%) also decomposes through the breaking of C-C bonds to form smaller alkyl radicals with 2 to 5 carbons. Subsequently, about 82% of C_7H_{15} undergoes β scission reactions forming smaller (C_2~C_5) alkyls and olefins, while about 12% of C_7H_{15} undergoes oxidation with O_2 and isomerization to form heptyl-hydroperoxy radical (C_7H_{14}-QOOH). However, the heptyl-hydroperoxy radicals directly dissociate into small hydrocarbons and heptene (C_7H_{14}), and the latter gets oxidized to form C_2~C_5. In contrast, due to the presence of double bond, about 33% of 1-heptene undergoes β scission reactions, mainly though reactions C_7H_{14}+OH=>CH_2CHCH_2+C_4H_8+H_2O and C_7H_{14}=>CH_2CHCH_2+C_4H_9, to form allyl radicals (CH_2CHCH_2). The rest 67% of 1-heptene is oxidized to form smaller hydrocarbons. All these oxidation reactions are faster compared to the dissociation reaction of 1-heptene. Consequently, the ignition delay is shorter for 1-heptene compared to that of n-heptane.

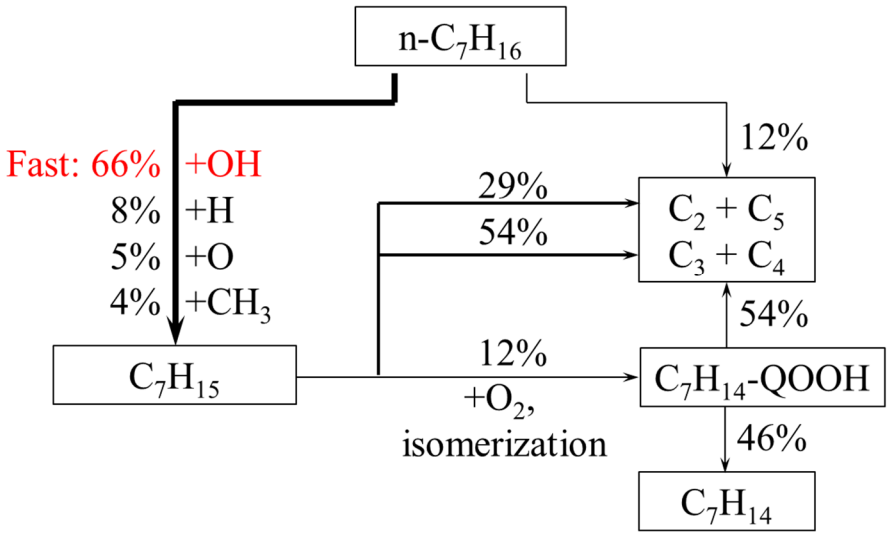

(a)

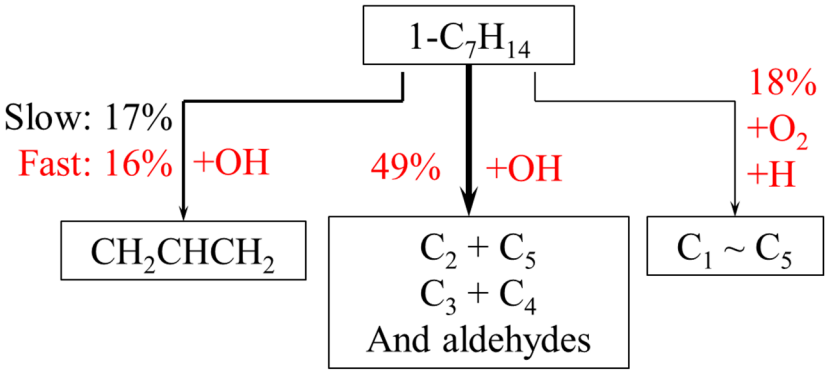

(b)

Figure 39. Simplified reaction paths for n-heptane and 1-heptene during the ignition with initial T=1300K, p=55atm and ϕ=1 in a homogeneous constant volume reactor. Simulation results are obtained from Chemkin.

Figure 40 compares the temporal profiles of temperature and NO mole fraction for the two fuels. These simulations were performed in a well-stirred reactor using the Chemkin software. Consistent with the reaction path analysis, the ignition delay times are 0.014ms and 0.018ms, while the peak temperatures are 3241K and 3217K for 1-heptene and n-heptane, respectively. The higher temperature is responsible for the 6.1% higher in NO for 1-heptene compared to that for n-heptane. Similar differences are observed for the NO formed through the prompt, N_2O and NNH intermediate routes for the two fuels. Finally, Figure 41 presents the mass profiles of allyl for the two fuels in spray combustion. The amount of allyl from 1-heptene combustion is increased by 45.6% compared to that of n-heptane. This trend confirms that the conclusion from the pathway analysis in constant volume simulations is still valid in spray flames.

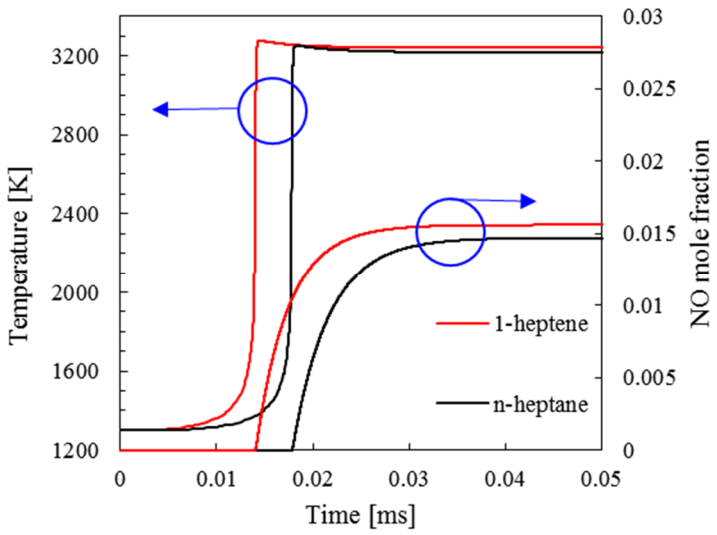

Figure 40. Temporal profiles of temperature and NO mole fraction for well-stirred reactor simulations with n-heptane and 1-heptene at initial T=1300K, p=55atm and ϕ=1.

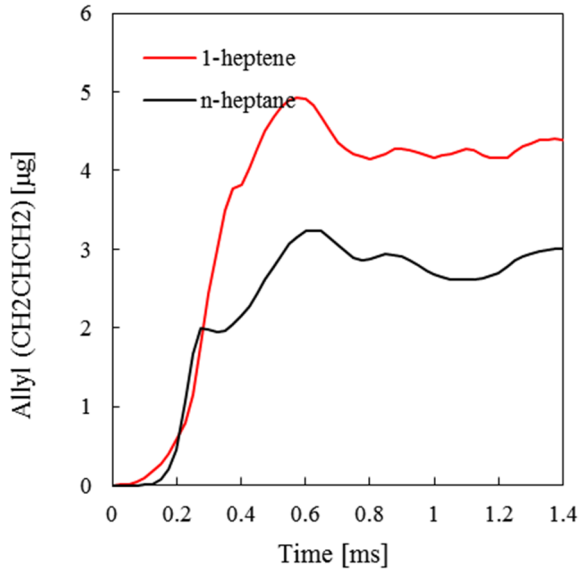

Figure 41. The mass of CH_2CHCH_2 for n-heptane (black) and 1-heptane (red) spray combustion with initial temperature of 1300K.

Figure 42 compares the total amounts of HCN, N_2O, NNH, and CH species in n-heptane and 1-heptene flames at 1.4ms. The CH_2 plot is similar to CH plot, and not shown. The amounts of HCN, N_2O, and NNH are higher in 1-heptene flame compared to those in n-heptane flame, indicating that the NO formed through these routes is also higher in 1-heptene flame. Amongst the three routes, the contribution of prompt NO is more significant compared to the N_2O and NNH intermediate routes. This is based on the fact that the total mass of HCN is noticeably higher than those of N_2O and NNH. It is also important to note that the amounts of CH and CH_2 (not shown) produced in n-heptane and 1-heptene flames are similar, implying that the prompt NO route depends less on these species, and more on the higher temperature in 1-heptene flame. Figure 43 presents the scatter plots of HCN, N_2O and NNH in ϕ-T space for the n-heptane and 1-heptene flames. Consistent with the plots of these species in Figure 37, most of HCN and thus prompt NO is formed in RPZ, i.e., in the region $2<\phi<6$ and $1700<T<2200$, while N_2O is formed in the lean region outside NPZ with $1500<T<2000$, and NNH is formed between RPZ and NPZ, in the region $2<\phi<3$ and $2400<T<2700$. Quantitatively, 1-heptene produces significantly higher HCN and thus higher prompt NO compared to that of n-heptane, as indicated by a wider range of red dots. The contributions of N_2O and NNH intermediate routes are also higher in -1-heptene flame that those in n-heptane flame, but the differences are not as significant.

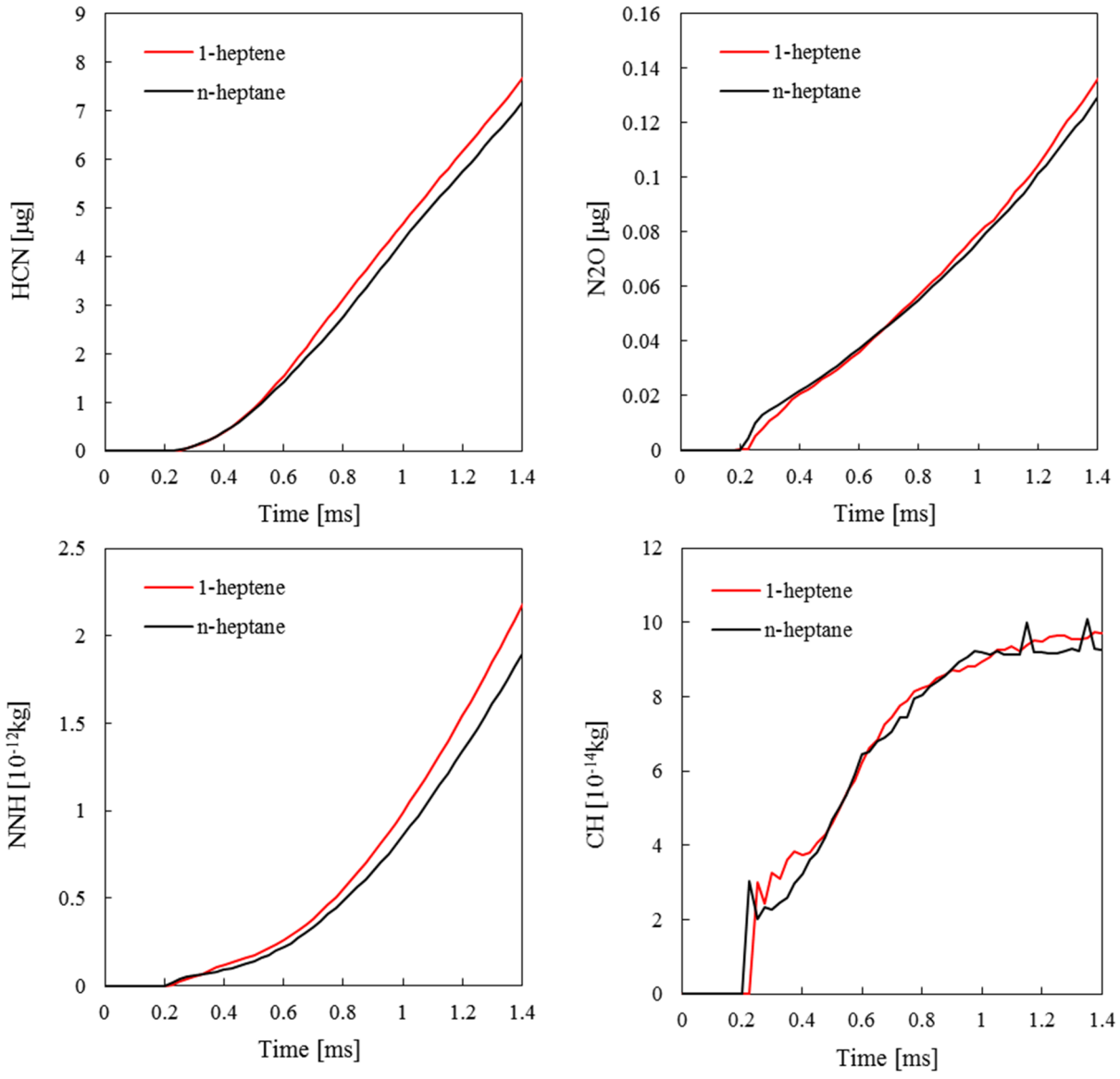

Figure 42. Total amounts of HCN, N_2O, NNH and CH species in n-heptane and 1-heptane flames. Initial temperature is 1300K.

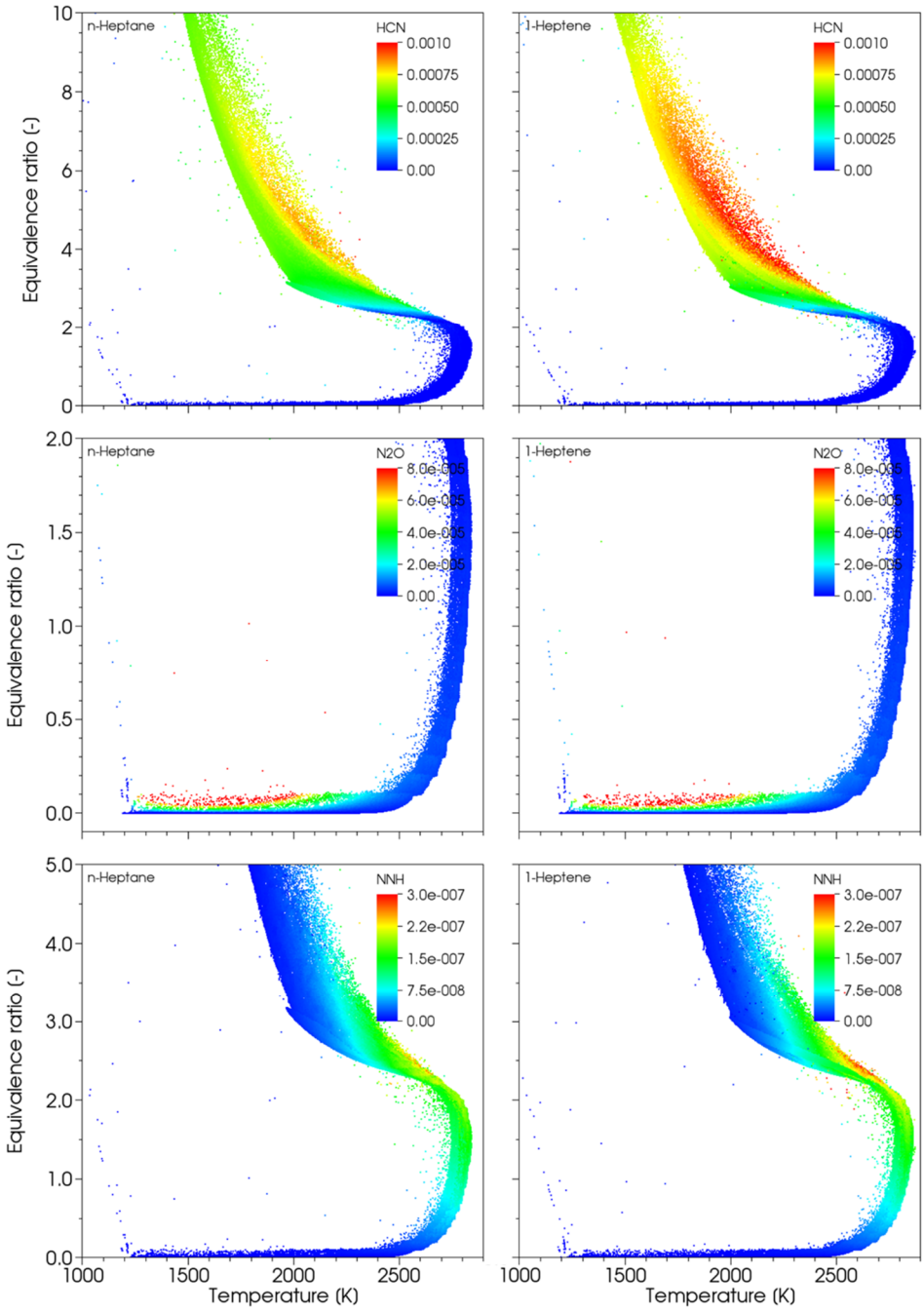

Figure 43. Scatter plots of HCN, N_2O and NNH in ϕ-T space for the n-heptane (left) and 1-heptene (right) flames at 1.4ms.

Figure 44 presents the mass profiles of CH_2 and CH for both the fuels. CH_2 and CH are the two of the main species related to prompt NO route. The amount of these radicals are very similar between the two fuels. This indicates that the prompt NO route does not primarily depend on the CH2 and CH but the temperature difference due to the fuel molecular structure.

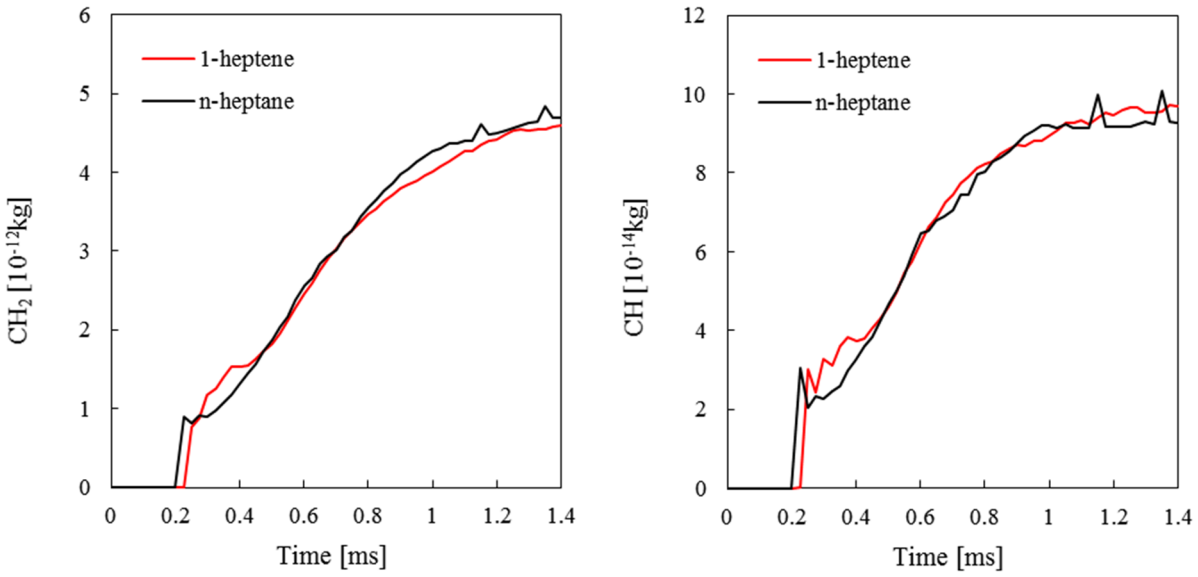

Figure 44. Mass of CH_2 and CH in the constant volume reactor for n-heptane (black) and 1-heptane (red) spray combustion with initial temperature of 1300K.

5.3 EFFECT OF FUEL MOLECULAR STRUCTURE ON PAH FORMATION

Figure 45 presents the benzene mass fraction contours for 1-heptene and n-heptane flames at t=1.4ms. While the benzene formation region is located within the rich premixed zone for both flames, the amount of benzene formed in 1-heptene is significantly higher. The peak mass fractions are 0.0118 and 0.0087 for 1-heptene and n-heptane, respectively, i.e., 36% higher benzene for 1-heptene. Similar trends were observed for the formation of heavier PAH, such as pyrene ($C_{16}H_{10}$). Figure 46 compares the temporal variation of integrated mass of benzene and pyrene in n-heptane

and 1-heptene flames. As expected, 1-heptene flame produces significantly more benzene and pyrene compared to n-heptane flame, with the differences being 22.0% and 21.9% for benzene and pyrene, respectively, at t=1.4ms.

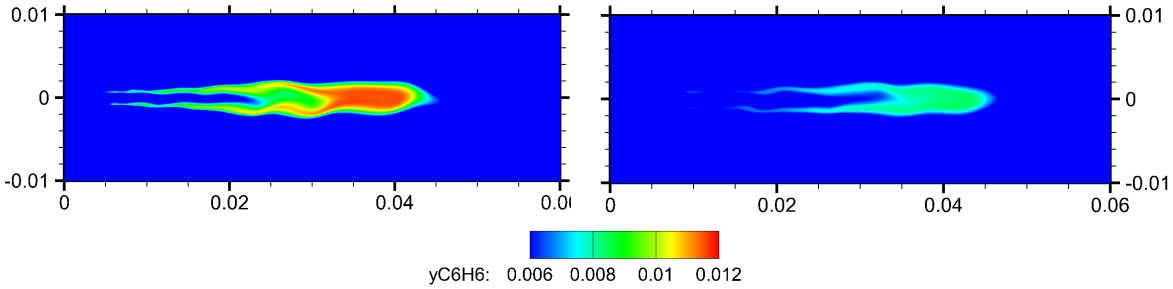

Figure 45. Benzene mass fraction contours for 1-heptene and n-heptane flames at 1.4ms. Mass fractions are between 0.006 and 0.012.

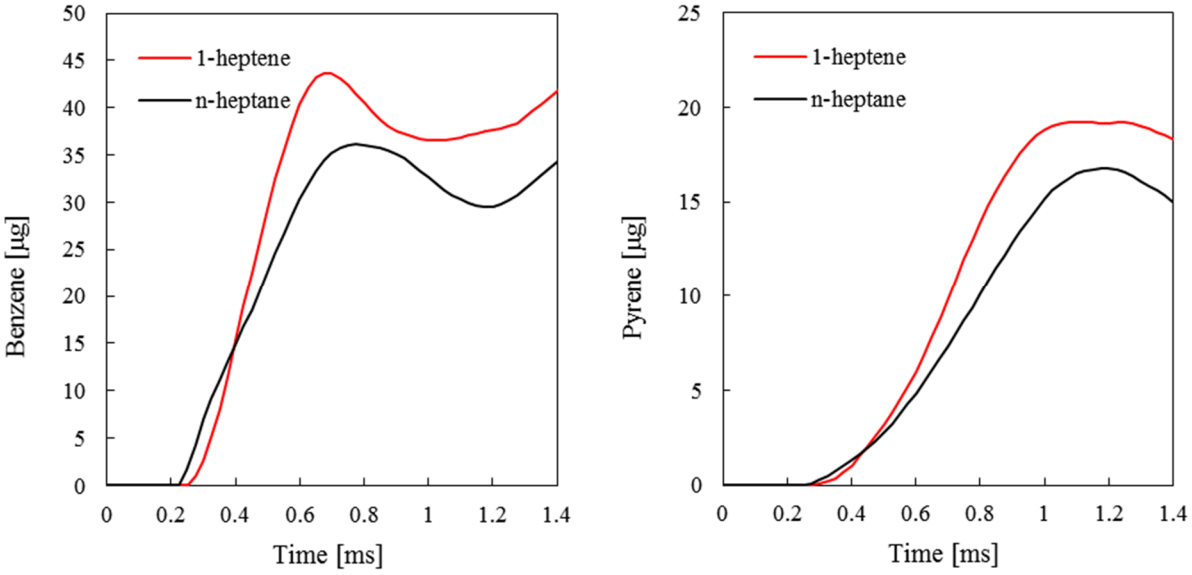

Figure 46. Integrated mass of benzene and pyrene for n-heptane (black) and 1-heptane (red) flames. Initial temperature is 1300K.

Since benzene is an important aromatic species for pyrene and subsequent soot formation, it is important to identify the dominant path for benzene formation. The path analysis is presented

in Figure 47, based on well-stirred reactor simulations for the combustion of the two fuels at the same conditions as those of Figure 39. Two major routes to form benzene involve reactions methyl-cyclo-pentadiene (MCPTD)=>benzene and C_3+C_3=>benzene, where C_3+C_3 represent reactions involving either two propargyl (C_3H_3) radicals or a propargyl reacting with allene (AC_3H_3) or propyne (PC_3H_3). While these two routes appear to be similar for the two fuels, the amount of benzene formed is higher in 1-heptene due to the higher concentrations of allene and C_4H_5 species. This is due to the fact that the presence of double bond in 1-heptene opens an additional route (highlighted with red) for allene formation through 1,3-butadiene (C_4H_6) and 3-butenal (C_3H_5CHO). In addition, the contribution of C_4H_5 route to form allene in 1-heptene is increased to 14% compared to 8% for n-heptane. Since these two routes are both associated with 1,3-butadiene, further analysis was done to identify the reason for the increased formation of 1,3-butadiene in 1-heptene. As highlighted by red lines in Figure 47, this can be attributed to the presence of double bond in 1-heptene, which leads to its direct decomposition to form two C_4 hydrocarbons, C_4H_8 and $CH_2C_3H_5$, through β scission reaction. These two C_4 species lead to the formation of 1,3-butadiene and C_4H_7 in 1-heptene. In contrast, there are fewer routes to form 1,3-butadiene and C_4H_7 in n-heptane. Moreover, the two routes involving C_4H_8 and C_5H_{10} produce much less 1,3-butadiene compared to the direct decomposition reactions for 1-heptene. Finally, 1-heptene also produces higher amount of cyC_5H_5 through C_5H_8, which further increases the amount of benzene formed through methyl-cyclo-pentadiene route. Thus, while the relative contributions of the two benzene formation routes are similar for the two fuels (21% for MCPTD route and 79% for C3 route vs. 20% and 80% for n-heptane and 1-heptene, respectively), the amount of benzene formed is higher in 1-heptene due to the significantly higher amounts of 1,3-butadiene and allene. This is further confirmed in Figure 48, which compares the integrated amounts of acetylene, propargyl, 1,3-

butadiene and allene formed in n-heptane and 1-heptene flames. While the amounts of acetylene and propargyl formed in the two flames are similar, significantly higher amounts of 1,3-butadiene (about 117% higher) and allene (48% higher) are formed in 1-heptene flame compared to those in n-heptane flame. Thus the pathway analysis based on well-stirred reactor simulations confirm the 3-D CFD results that the increased amount of benzene in 1-heptene flame is associated with the β scission reactions due to the presence of double bond in 1-heptene. This result is generally consistent, except for the methyl-cyclo-pentadiene route, with the reaction path analysis for benzene formation reported in a previous study [131] dealing with 1-heptene and n-heptane counterflow flames.

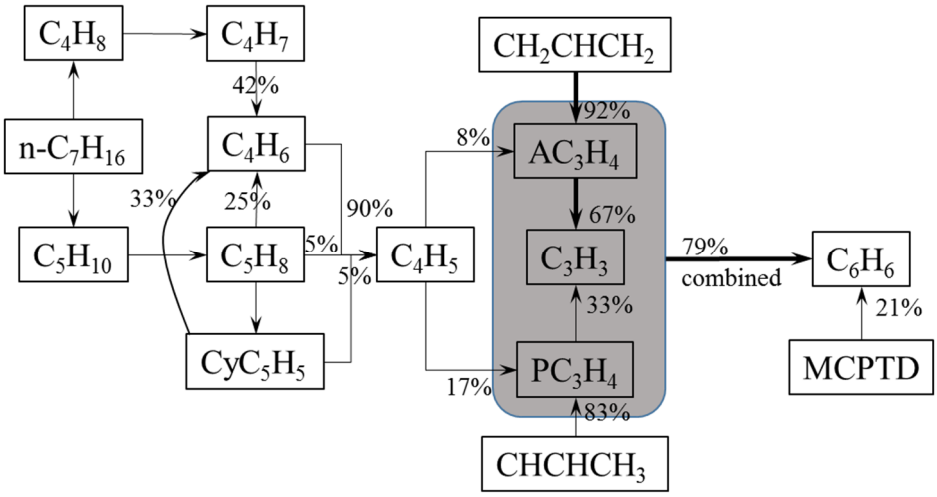

(a): n-Heptane

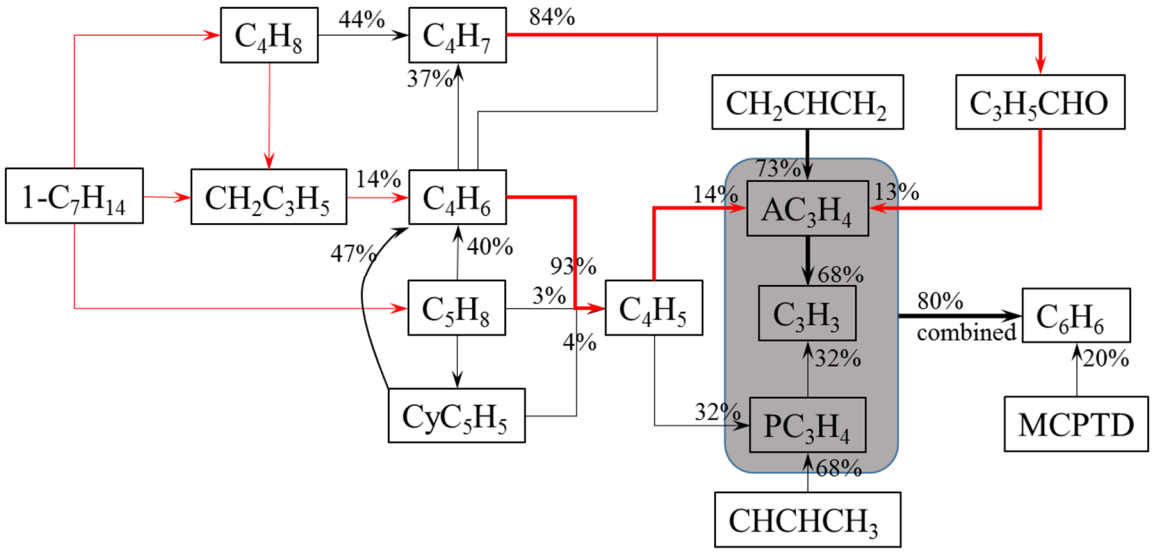

(b): 1-Heptene

Figure 47. Dominant reaction paths for benzene formation for n-heptane (a) and 1-heptene (b). Simulations are performed in a well-stirred reactor with initial T=1300K, p=55atm and ϕ=1. The effect of double bond in 1-heptene on the various reactions are indicated by the red color. Also AC_3H_4: allene; PC_3H_4: propyne; MCPTD: methyl-cyclo-pentadiene. Percentage implies the relative amount of a species formed though a given reaction. For example, in Fig. a, 79% of C_6H_6 is formed through the combined reactions between C_3 species.

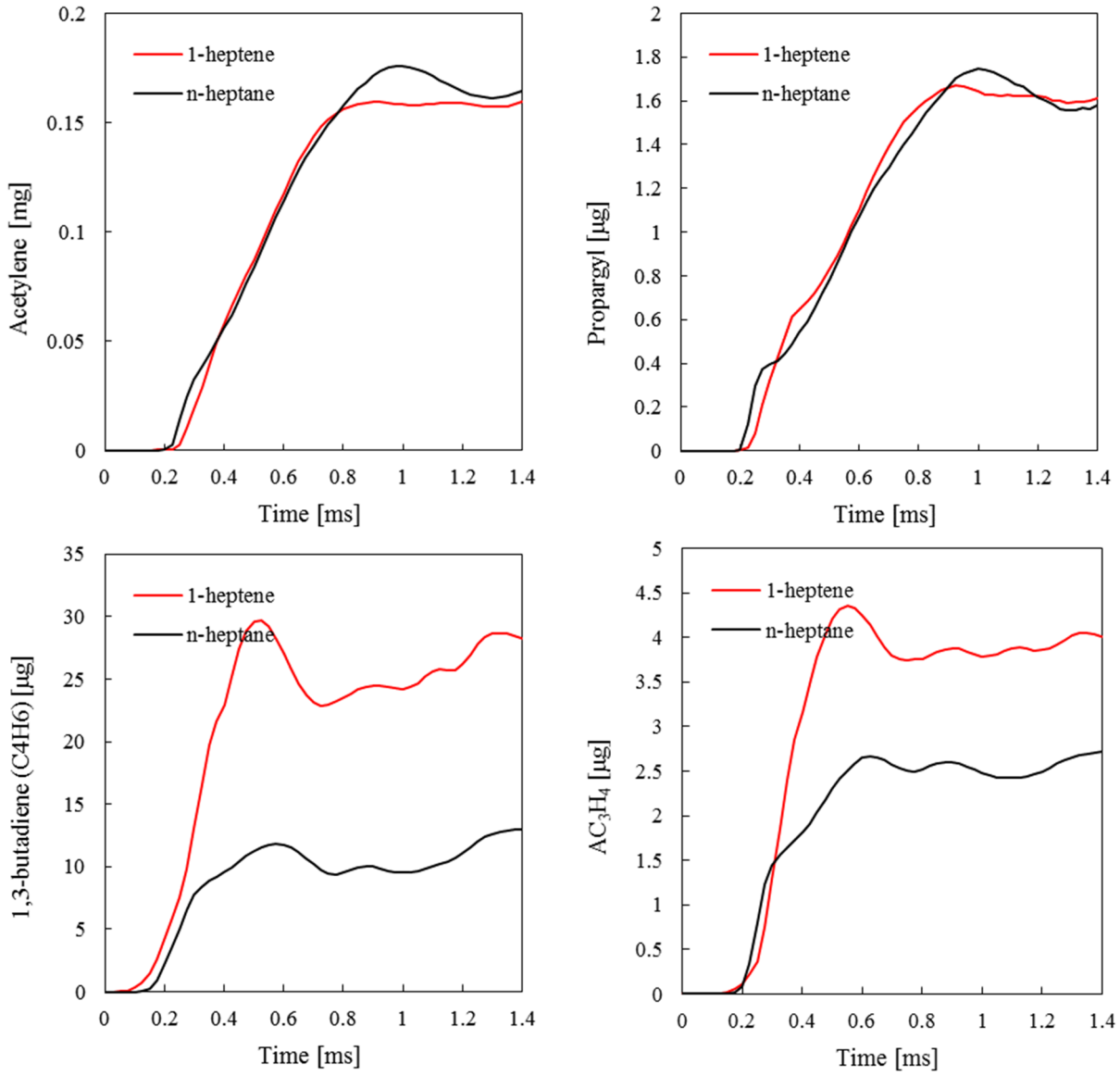

Figure 48. Integrated mass of acetylene (C_2H_2), propargyl (C_3H_3), 1,3-butadiene (C_4H_6) and allene (AC_3H_4) in n-heptane and 1-heptane flames.

6 DUAL-FUEL DIESEL ENGINE SIMULATIONS

(Previously published as Xiao Fu, Suresh Aggarwal, Two-stage ignition and NTC phenomenon in diesel engines, Fuel, 2015, 144, 188-196, DOI: 10.1016/j.fuel.2014.12.059)

For the second part of the thesis, detailed discussions on the dual-fuel combustion strategy are organized in three parts: the two-stage ignition behavior, effects of methane on combustion and emissions, and dual-fuel strategy optimizations.

6.1 IGNITION BEHAVIOR IN SINGLE- AND DUAL-FUEL COMBUSTION

6.1.1 Two-Stage Ignition in Single Fuel Combustion

Using the 3D simulation code, the temporal and spatial evolution of chemistry reactions can be studied in detail. The ignition chemistry of large straight-chain hydrocarbons is known to be characterized by the NTC and two-stage ignition processes[132]. These processes are described by a transition between the low- and high-temperature reaction paths as determined by the formation of peroxy radical, R + O_2 <=> ROO. Here alkyl radical (R) is formed from fuel decomposition through H abstraction. The two competing reaction paths and the associated NTC and two-stage ignition processes have been discussed in earlier studies for both homogeneous[132] and heterogeneous[133,134] mixtures; the latter in the context of droplet ignition. The two-stage ignition in diesel engines is also well known. Here this phenomenon is examined by following the temporal and spatial evolution of two radical species, alkyl hydroperoxy (QOOH) and OH radicals, which are shown in Figure 49 (a) and the integrated heat and heat release rate profiles in Fig. (b). For this engine simulation case, the SOI is -8° ATDC. And the first and second stage ignition for the engine case occurs at -4.8° and -2.4° ATDC, respectively. Crank angle values are converted to

time using engine speed of 1500rpm. The duration time between first- and second-ignition stages agrees with that calculated using constant pressure homogeneous reactor simulation at the same initial temperature and pressure, with n-heptane/air equivalence ratio at 1. The first stage ignition for diesel spray is defined by the first inflection point in QOOH profile, and the second stage ignition by the sharp rise in OH profile. In this case, the engine simulation is started at the instant of intake valve closing, the SOI is -8° ATDC, and the injection duration is 8.5 CAD. The physical delay, computed based on the integrated n-heptane vapor mass exceeding a value of 10^{-6} kg, is 1 CAD. The physical delay is associated with the processes of fuel atomization, vaporization and mixing. It is also important to note that in case of QOOH and OH profiles not being available (e.g., with a simplified reaction mechanism or engine experiments), one can also define the first and second stage ignition events using the heat release rate and integrated heat release profiles, as shown in Figure 49 (b).

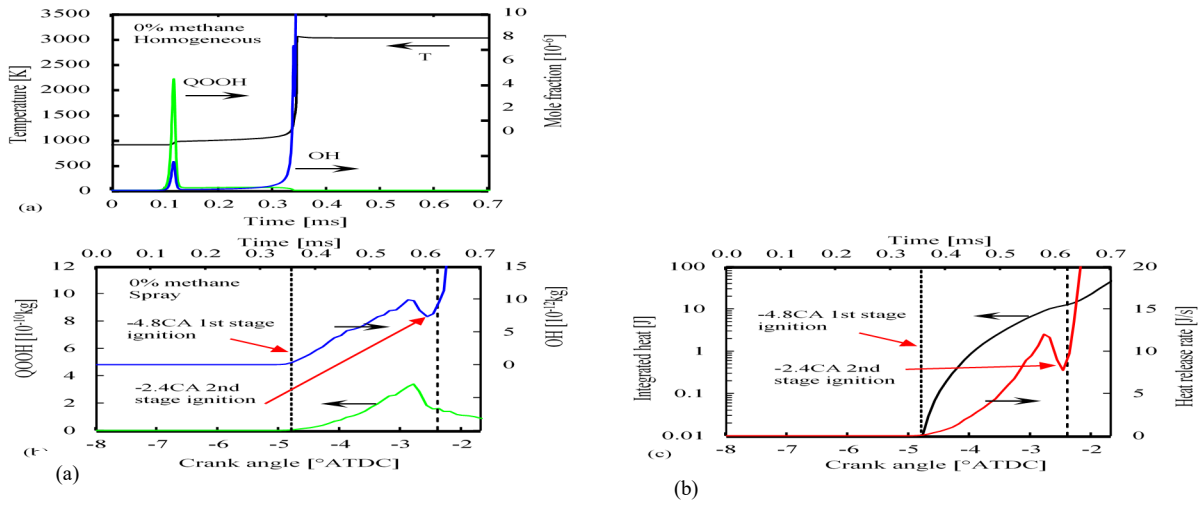

Figure 49. Temporal profiles of QOOH and OH mole fractions (a) and heat release rate and integrated heat release profiles (b) during ignition for engine sprays with 0% methane.

Further insight into the spatial evolution of two-stage ignition and the associated ignition kernel can be gained from the QOOH and OH contour plots presented in Figure 50. Black dots in the figure represent n-heptane droplet parcels. The processes of liquid fuel injection, atomization, vaporization, and ignition are clearly depicted in this figure. As indicated by QOOH contours, the first stage ignition occurs near the injector at -4.8° ATDC. This is followed by the spreading of first stage ignition kernel downstream in the fuel jet. As a result, the total QOOH mass increases with time, and chemical reactions associated with the second stage ignition are initiated. Subsequently, the second stage ignition occurs in the tip region of the jet at -2.4° ATDC, as indicated by OH contours in Figure 50, as well as by OH temporal profile in Figure 49a.

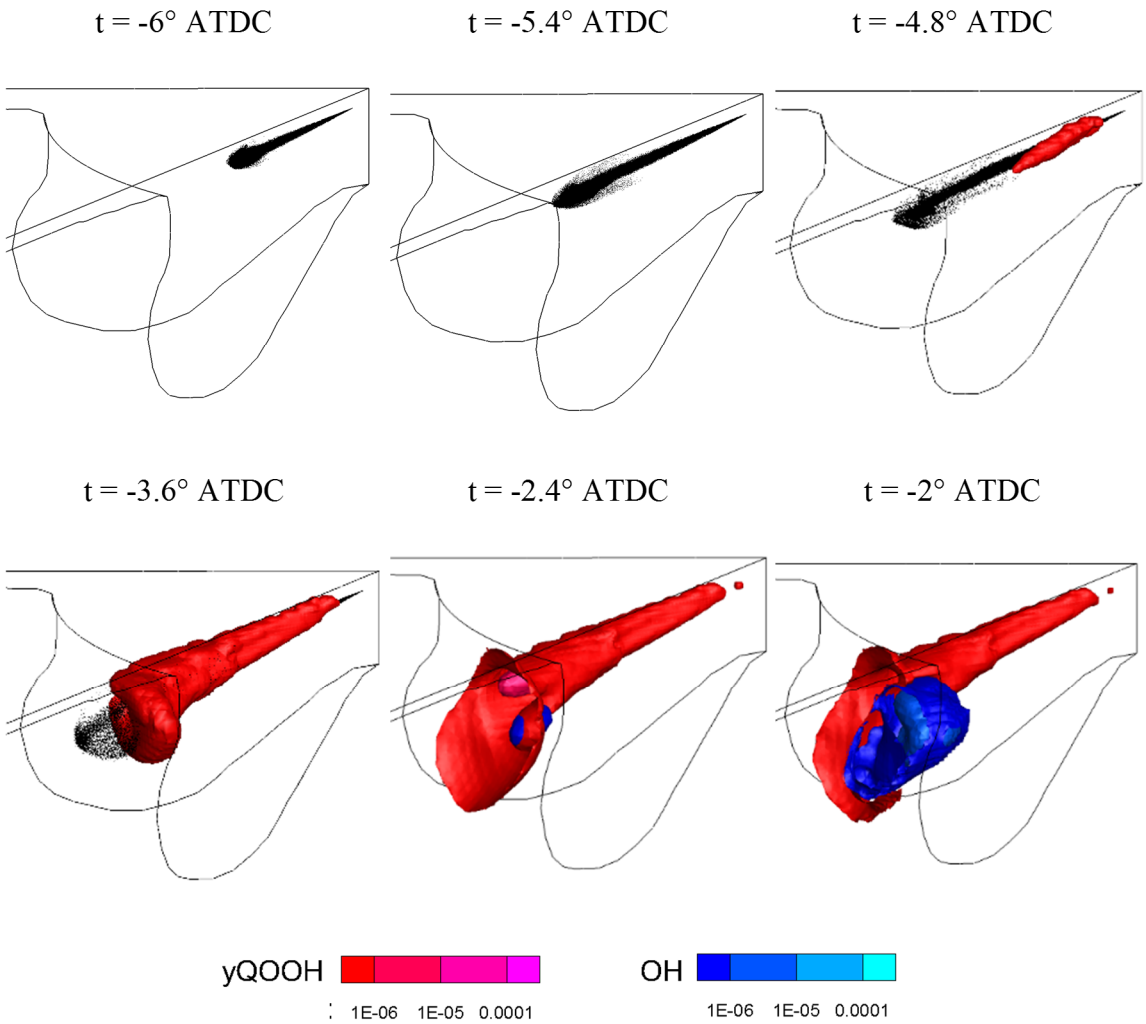

Figure 50. QOOH and OH contours for 0% methane case showing the first stage ignition at -4.8° ATDC and second stage ignition at -2.4° ATDC. Black dots represent n-heptane droplet parcels. SOI is -8° ATDC.

An alternative way of analyzing the ignition process is through equivalence ratio – temperature (ϕ – T) scatter plot. Here the equivalence ratio is calculated by:

$$\phi = \frac{2\sum_i N_i \eta_{C,i} + \frac{1}{2}\sum_i N_i \eta_{H,i}}{\sum_i N_i \eta_{O,i}} \tag{88}$$

where i is all species except H_2O and CO_2; N_i is the number of moles of species i; and $\eta_{C,i}$, $\eta_{H,i}$ and $\eta_{O,i}$ are the number of carbon, hydrogen and oxygen atoms, respectively, for species i. The ϕ – T scatter plot is useful and well accepted in 3D CFD studies involving both turbulence and chemistry, because it breaks down the three dimensional physical space into a two dimensional ϕ – T space while indicating the local fuel/air ratio and temperature information. Figure 51 presents the ϕ – T scatter plot for the single fuel case at -2.4° ATDC. The OH mass fraction of the scatters is presented using different color. The peak of OH mass fraction is $3x10^{-6}$ and is located near 1300K. The temperature increases due to heat release from the first-stage ignition which covers from T=550K to 1000K. The narrow high OH mass fraction region near $T \approx 850K$ indicates the main location of first stage n-heptane ignition. During this stage, OH is formed through the QOOHOO radical to form ketohydroperoxide. The QOOHOO radical comes from the combination of QOOH and O_2. The range of ϕ is between 1 and 8 for first-stage ignition. Once the second-stage ignition occurs, the temperature reaches 1000 to 1025K, indicated by high OH mass fraction region

above T=1025K. A distinct horizontal gradient of OH mass fraction can be noticed around T=1000K to 1100K, which demonstrate the sudden increase in temperature for the second stage ignition. The most important chain branching reaction is $M+H_2O_2=M+2OH$, which is the key reaction causing the second ignition stage over the wide equivalence ratio range.

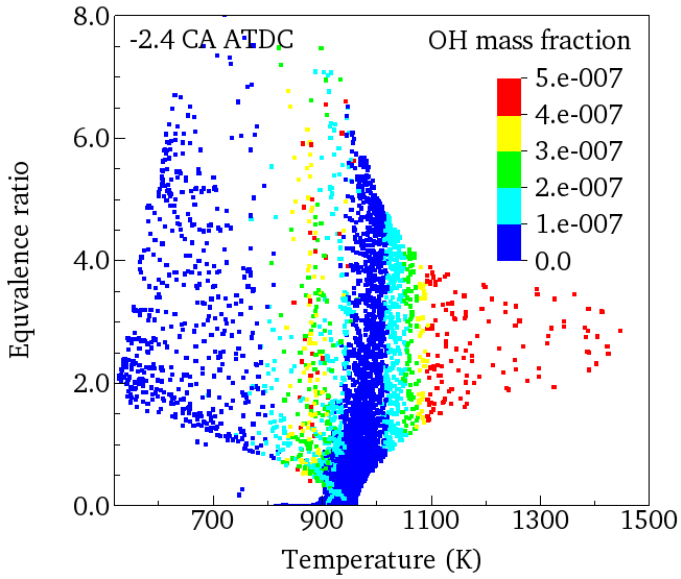

Figure 51. Scatter plot of OH mole fraction in equivalence ratio -temperature space at -2.4 CA ATDC (2nd stage ignition) for 0% methane case. The color of the scatter plot indicates local OH mass fraction.

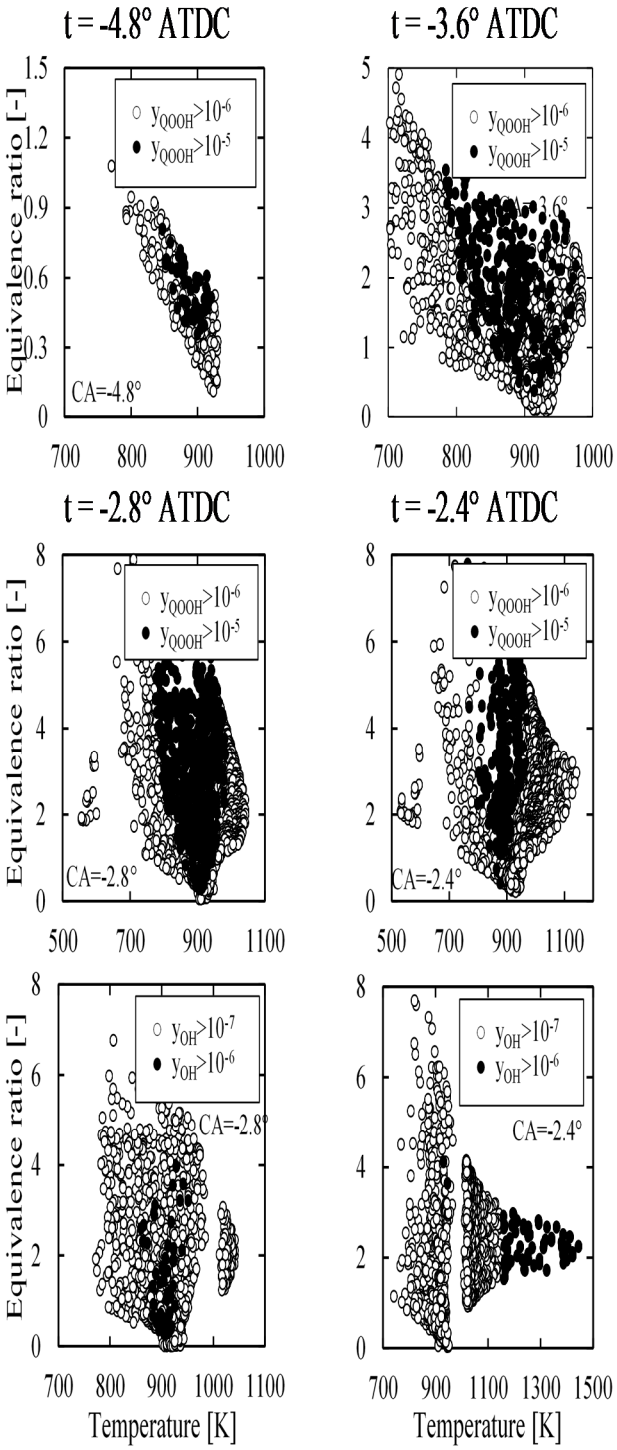

Figure 52. Scatter plots of QOOH and OH mass in ϕ-T space for the 0% methane case. QOOH plots depict the first stage ignition at -4.8°ATDC, and subsequently the evolution of

first stage ignition kernel at -3.6°, -2.8° and -2.4°. OH plots indicate the formation of second stage ignition kernel at -2.8° and the occurrence of second stage ignition at -2.4°.

Figure 52 presents the temporal evolution of the ϕ-T scatter plots in a diesel engine. QOOH scatter plots indicate that the first ignition occurs in a relatively narrow temperature range (T≈850-900K), but a wide ϕ range (0.3-0.8), implying a spatially wide ignition kernel. The temperature and species fields then continue to evolve due to vaporization, mixing and chemical reactions. This is illustrated by the broadening QOOH plots at -3.6°, -2.8° and -2.4° ATDC, and by the widening ϕ and T range. The temperature increases due to heat release from the first ignition, which in terms enhances vaporization rate and promotes ignition kinetics leading to second-stage ignition, which occurs near T≈1050-1100K, and ϕ=1-4, as indicated by the OH scatter plots at -2.8° and -2.4° ATDC in Figure 52. Thus, processes leading to second ignition are also strongly influenced by the spatially and temporally evolving two-phase flow field in diesel sprays, whereas in homogeneous systems, they essentially depend on temperature at the end of first stage. Furthermore, the first and second ignition locations are spatially separated in diesel sprays, as discussed earlier in the context of Figure 50.

6.1.2 Two-Stage Ignition in Dual-Fuel Combustion

The effect of methane on two-stage ignition was characterized by performing engine simulations for three dual-fuel cases with 90, 93, and 97% methane by volume. The SOI, injection duration, and mass of n-heptane injected were kept the same for these three cases. Note that as the amount of methane is increased, it increases the engine power, which will be discussed in the next section.

For the dual-fuel engine, methane air mixture is introduced into the cylinder through the intake valve, while n-heptane is injected directly and compress ignited. Simulations for all the engine cases start at the instance of intake valve closing (IVC = 132° BTDC). The initial mixture mass ($m_{g,0}$) in the cylinder is determined by specifying the mixture temperature (T_{IVC}), pressure (p_{IVC}), and volume (V_{IVC}) at IVC. As indicated in Table 2, for the single-fuel case, the mass of n-heptane ($m_{h,0}$) injected is specified as 8.8 mg. This corresponds to low load conditions. For dual-fuel cases at low load, the total energy input (E_{in}) to the cylinder is kept the same as that for the single fuel case, as the volume fractions of n-heptane and methane are varied. The volume fractions are defined in terms of the molar ratio of liquid fuel to gaseous fuel (r_{lg}). Then the mass of liquid fuel (m_h) and gaseous fuel (m_m) for a given case can be determined using the following two equations:

$$E_{in} = m_h HV_h + m_m HV_m \tag{1}$$

$$r_{lg} = \frac{m_h / M_h}{m_m / M_m} \tag{2}$$

As the mass of methane in the cylinder is increased, it decreases the mass of air (m_g), which can be calculated using the following equation:

$$n_{IVC} = \frac{V_{IVC} p_{IVC}}{R T_{IVC}} = \frac{m_m}{M_m} + \frac{m_g}{M_g} \tag{3}$$

Here HV_h and HV_m are the lower heating values for n-heptane and methane, respectively. $E_{in} = m_{h,0} \times HV_h$, R is the universal gas constant, and M_h, M_m and M_g are the molecular weights for n-heptane, methane and air, respectively. The initial conditions and some key engine performance properties for the various cases are provided in Table 6.

Table 6. Parameters for Various Simulation Cases

	Low load		Medium load
Molar ratio of methane (r)	0%	90%	97%
Molar ratio of n-heptane (1-r)	100%	10%	3%
Total chemical energy per cylinder (E_{in}), J	390		1014
Mass of n-heptane per cylinder (m_h), mg	8.8	3.3	3.3
Mass of methane per cylinder (m_m), mg	0	4.8	17.3
Mass of air per cylinder (m_g), mg	546	542	515
ϕ based on methane	0	0.16	0.58
ϕ based on both methane and n-heptane	0.24	0.25	0.68
Total volume per cylinder (V_{IVC}), L	0.448		
Work output per cylinder, J	133	87	351
Indicated mean effective pressure (IMEP), bar	2.78	1.82	7.36
Indicated power, kW	1.66	1.09	4.39

Figure 53 presents the temporal profiles of pressure and HRR for three cases with 0%, 90%, and 97% methane by volume. For the first two cases corresponding to low-load condition, the amount of energy input is kept fixed. For the 90%, and 97% methane cases, the amount of n-heptane injected is kept fixed. Consequently, the energy input and engine load increase as the amount of methane in the cylinder is increased. The IMEP and indicated power are both increased in the 97% methane case compared with 90% case as shown in Table 6. In addition, the HRR plots indicate that the ignition delay is increased due to the addition of methane.

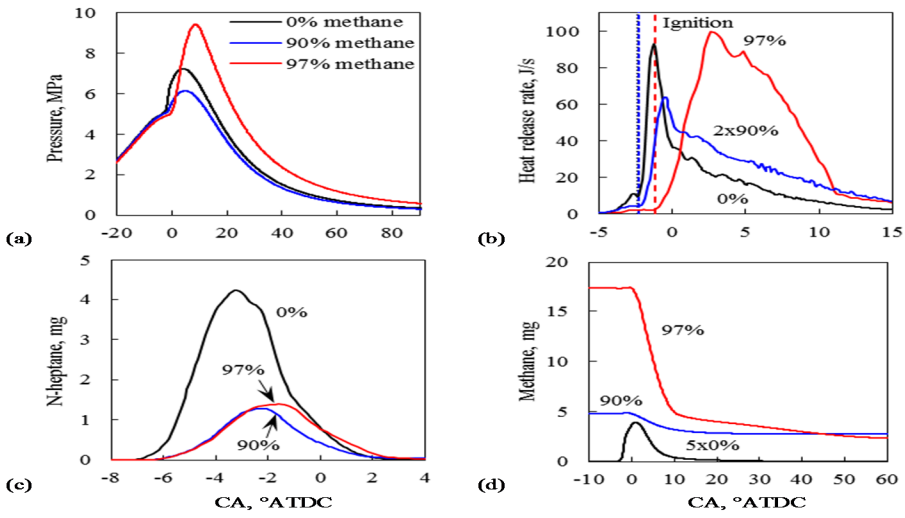

Figure 53. Pressure and heat release rate profiles with respect to crank angle for the 0%, 90% and 97% methane cases. Vertical lines in Fig. b indicate crank angles at ignition for corresponding cases.

Simulations were also performed for the corresponding homogeneous cases at the same pressure and temperature as those for the engine cases. Figure 54 compares the first and second stage ignition delays for both diesel sprays and homogeneous mixtures with different methane mole fractions. As discussed earlier, the respective ignition delays were determined from the QOOH and OH temporal profiles, which are presented in Figure 55 for the 90 and 97% methane cases. The ignition delays can also be obtained from the integrated heat release and heat release rate profiles, as noted earlier.

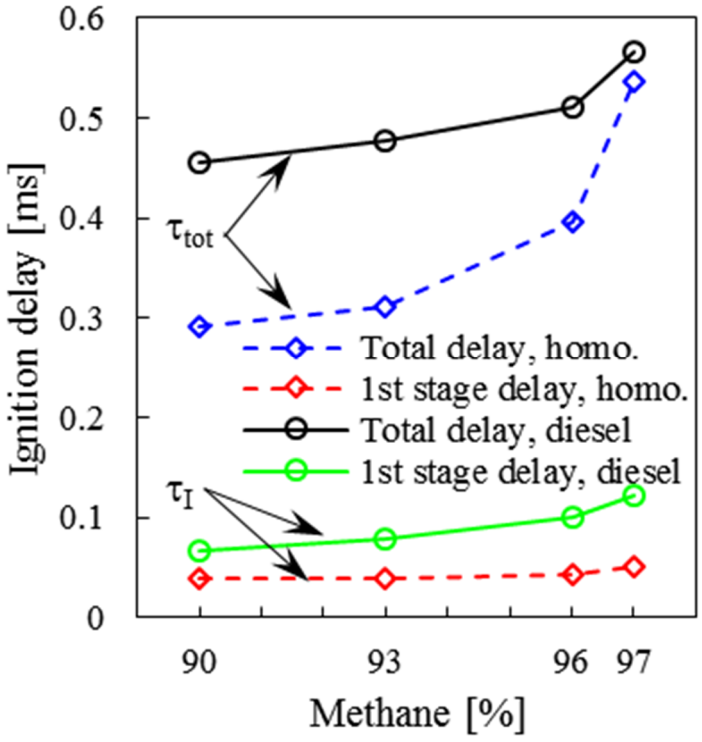

Figure 54. First and total ignition delays versus methane molar fraction for homogeneous mixtures and diesel sprays.

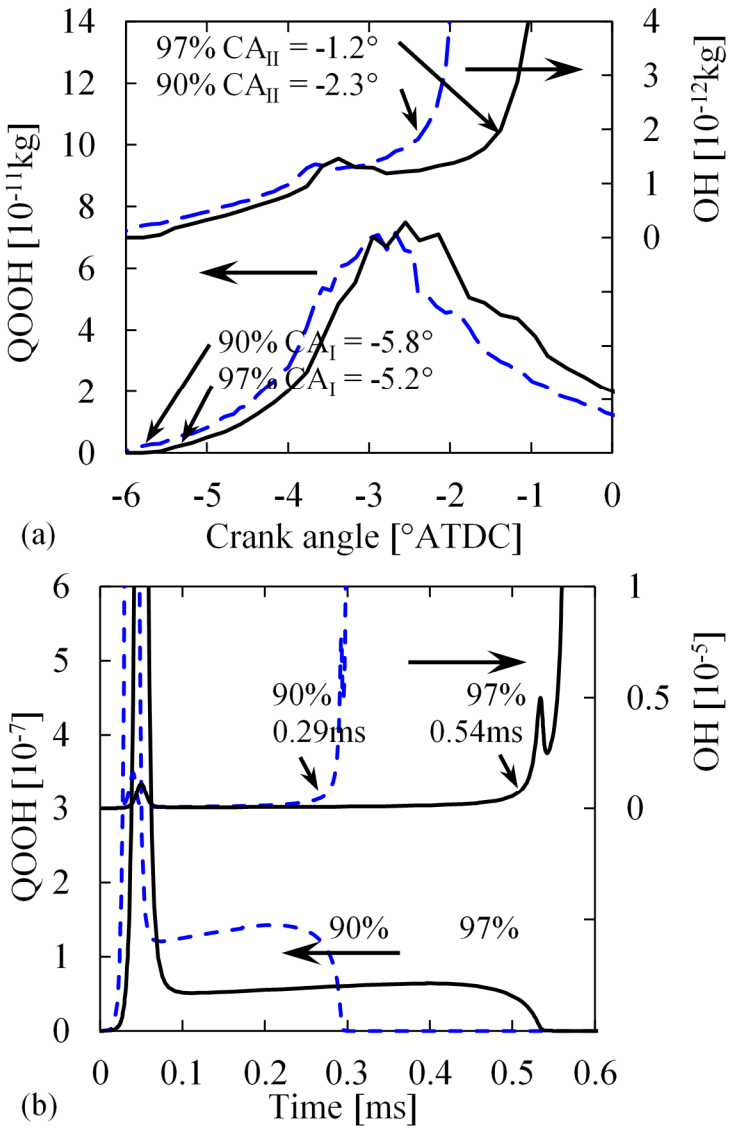

Figure 55. QOOH and OH mass profiles during ignition of diesel spray (a) and QOOH and OH mole fraction profiles for homogeneous mixture (b) for 90% and 97% methane.

For both sprays and homogeneous mixtures, the first (t_I) and second stage (t_{II}) ignition delays increase as the amount of methane is increased. The increase in t_I may be due to a reduction in O_2 concentration, which decreases the rate of formation of RO_2 and QOOH. In contrast, the increase

in t_{II} may be due to both the reduction in O_2 concentration and the chemical effect of methane. Consequently, the effect of methane on t_{II} is stronger compared to that on t_I. Furthermore, the sensitivity analysis for the homogeneous case indicated that the inhibiting effect of methane is primarily due to reaction $CH_4 + OH = CH_3 + H_2O$, which depletes OH radicals. Another observation from Figure 54 is that the ignition delays are higher for sprays compared to those for homogeneous mixtures, and this can again be attributed to the spatially and temporally evolving two-phase flow field. The two-phase flow effects for the 90% and 97% methane cases are depicted in Figure 56, which presents the QOOH and OH contour plots. The corresponding scatter plots in ϕ-T space are shown in Figure 57. These contour and scatter plots are qualitatively similar to those for the 0% methane case shown in Figure 50 and Figure 52, respectively, implying that the two-stage ignition process for n-heptane is not affected qualitatively by the addition of methane. Similar to the 0% methane case, the QOOH contours for the dual-fuel cases indicate that first stage ignition occurs near the injector. The ignition kernel then spreads downstream in the fuel jet, leading to second stage ignition that occurs in the spray tip region, as indicated by OH contours in Figure 56. Furthermore, the scatter plots in Figure 57 indicate that the first-stage ignition for the dual-fuel cases also occurs in a narrow T range (≈850-900K), but a wide ϕ range (0.3-0.8), implying a spatially wide ignition kernel leading to second-stage ignition, which occurs near T≈1050-1100K and ϕ ≈1-4. In summary, the two-stage ignition process for diesel sprays remains intact even when as much as 97% methane is present by volume. However, the fuel injection and spray processes are strongly influenced by methane. For instance, the liquid penetration decreases as the amount of liquid fuel injected is reduced. Consequently, the physical delay increases for the dual-fuel cases, as the amount of methane is increased.

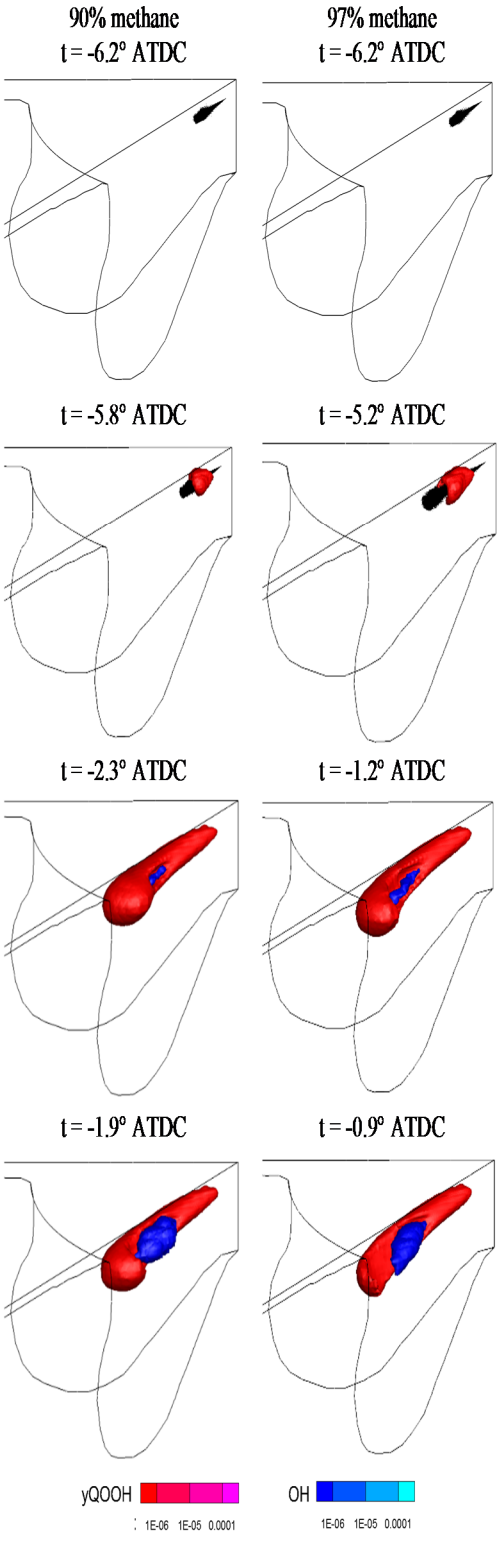
90% methane
t = -6.2° ATDC
97% methane
t = -6.2° ATDC
t = -5.8° ATDC
t = -5.2° ATDC
t = -2.3° ATDC
t = -1.2° ATDC
t = -1.9° ATDC
t = -0.9° ATDC
yQOOH
1E-06 1E-05 0.0001
OH
1E-06 1E-05 0.0001

Figure 56. QOOH and OH contours for the 90% and 97% methane cases showing the first- and second-stage ignition processes. Black dots represent the n-heptane droplet parcels. SOI is -8° ATDC.

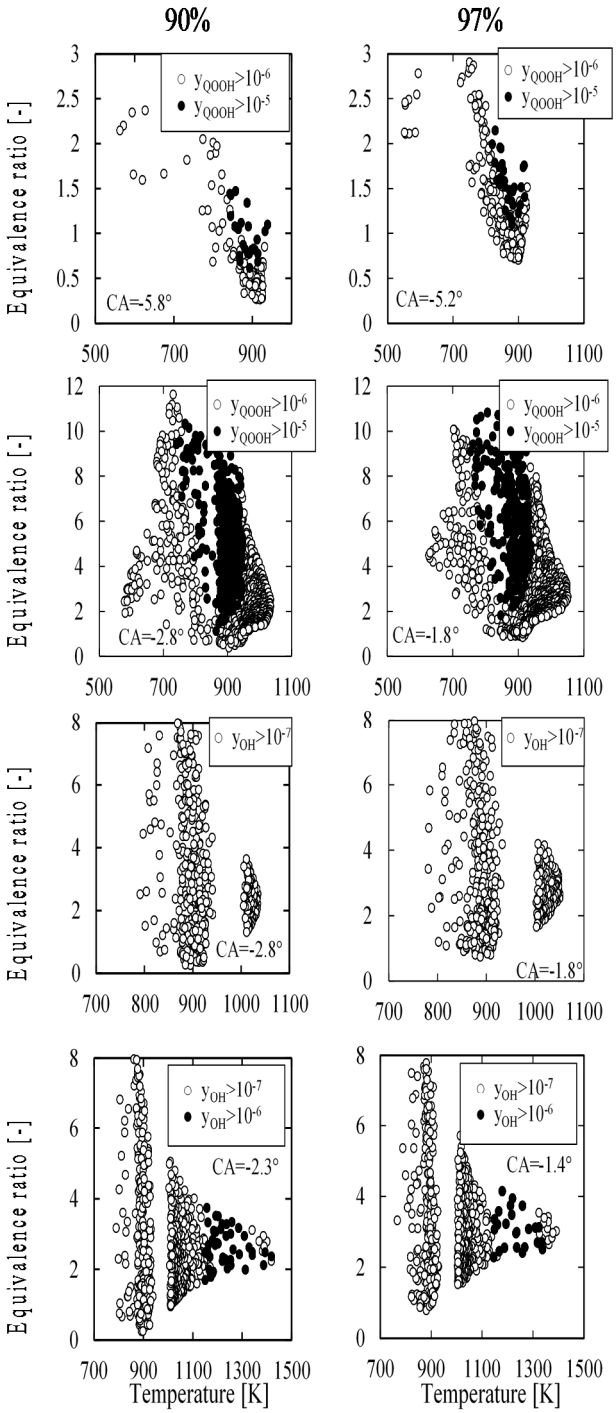

Figure 57. Scatter plots of QOOH and OH mass in ϕ-T space for the 90% and 97% methane cases. QOOH plots at -4.8° ATDC depict the first stage ignition, and subsequently the evolution of first stage ignition kernel at -3.6° -2.8° and -2.4°. OH plots at -2.8° and -2.4° depict the second stage ignition process.

6.2 EFFECT OF METHANE ON COMBUSTION AND EMISSIONS

6.2.1 Effect of Methane on Dual-Fuel Engine Combustion

Figure 58 presents the temporal profiles of pressure, heat release rate (HRR), n-heptane vapor mass, and methane mass for three cases with 0%, 90%, and 97% methane by volume. Conditions for these cases are the same in Table 6. For the first two cases corresponding to low-load condition, the amount of energy input is kept fixed, while for the 90%, and 97% methane cases, the amount of n-heptane injected is kept fixed. Consequently, the energy input and load increase as the amount of methane in the cylinder is increased. The higher load for the 97% methane can also be seen from the pressure and HRR plots in Figure 58. In addition, the HRR plots indicate that the ignition delay is increased due to the addition of methane, as discussed earlier.

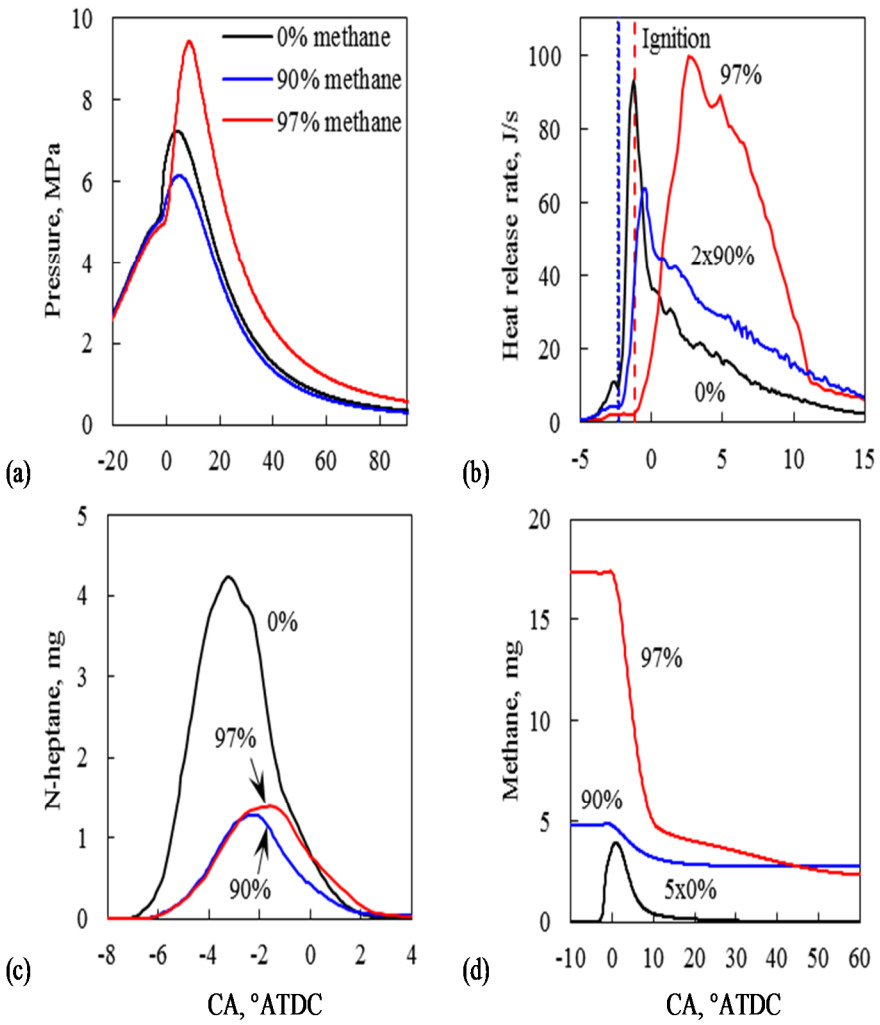

Figure 58. Pressure, heat release rate, n-heptane vapor mass, and methane mass profiles with respect to crank angle for the 0%, 90% and 97% methane cases. Vertical lines in Fig. b indicate crank angles at ignition.

The combustion process in a diesel engine has often been characterized by a hybrid combustion mode involving rich premixed combustion and diffusion combustion[50,51]. In contrast, depending upon operating conditions, the heat release in a dual-fuel engine may also involve a lean combustion mode with a propagating flame[135]. The HRR and methane mass profiles in Figure

58 seem to support this hypothesis, especially for the 97% methane case. However, the methane mass profile for the 90% case seems to indicate the extinction of this flame due to ultra lean conditions at low load. These aspects concerning the combustion modes and flame propagation/extinction can be analyzed by examining the evolution of some key species during combustion. Figure 59 presents CO, CO_2 and HO_2 mass fraction contours at different crank angles for the single-fuel case. These plots are cut through the peak ϕ value location. Black lines in each figure indicate ϕ contours (0.3-3). The corresponding plots for the two dual-fuel cases are shown in Figures 11 and 12. These plots can be used to identify the different combustion zones. For instance, for all three cases, the high CO region locates the rich premixed zone with ϕ between 2.0-3.0, while the high CO_2 region corresponds to diffusion combustion zone with ϕ near 1. This is consistent with previous studies[136,137] dealing with partially premixed flames, indicating that the most of CO is produced in the rich premixed zone, while the most of CO_2 is produced in the diffusion combustion zone, where the temperature is the highest. Thus, the rich premixed zone is characterized by n-heptane decomposition and partial oxidation, producing CO, H_2, and intermediate hydrocarbon species. These species are then consumed through oxidation reactions in the diffusion combustion zone. In a similar way, HO_2 plots can be used to examine the lean combustion zone. Thus, for the two dual-fuel cases, HO_2 contours at 0 and 4° ATDC (cf. Figure 60 and Figure 61) indicate the presence of a lean combustion zone, characterized by a propagating flame. Clearly, the corresponding contours for the single-fuel case do not show this lean combustion zone (cf. Figure 59).

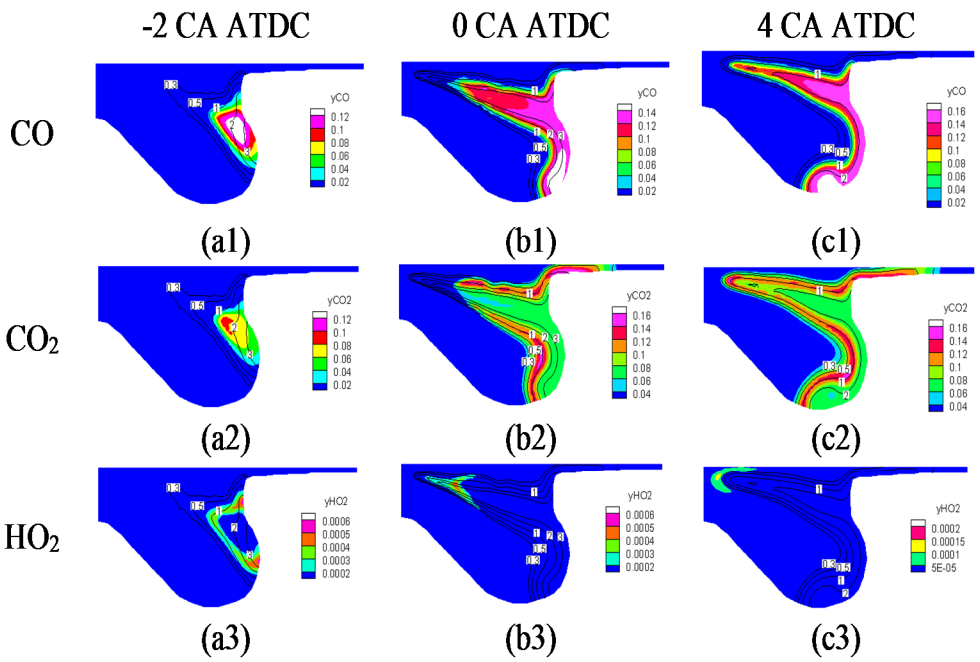

Figure 59. Mass fraction contours of CO (a1-c1), CO_2 (a2-c2) and HO_2 (a3-c3) at -2, 0 and 4 CA ATDC for the 0% methane case. Black lines in each figure indicate ϕ contours (0.3 to 3).

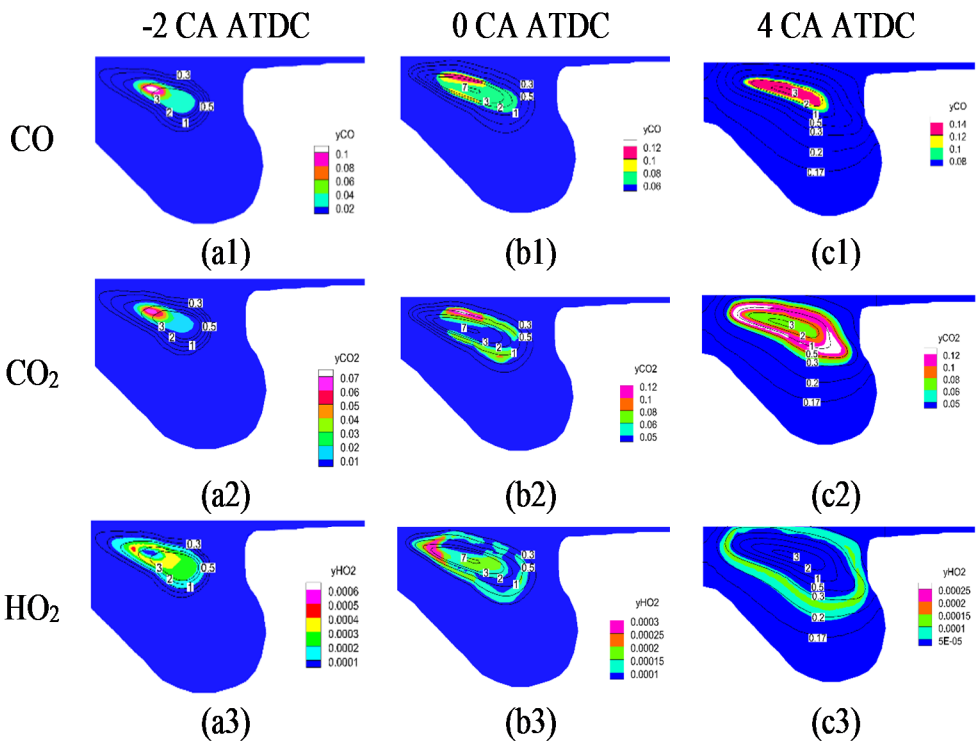

Figure 60. Mass fraction contours of CO (a1-c1), CO_2 (a2-c2) and HO_2 (a3-c3) at -2, 0 and 4 CA ATDC for the 90% methane case. Black lines in each figure indicate ϕ contours (0.3 to 3).

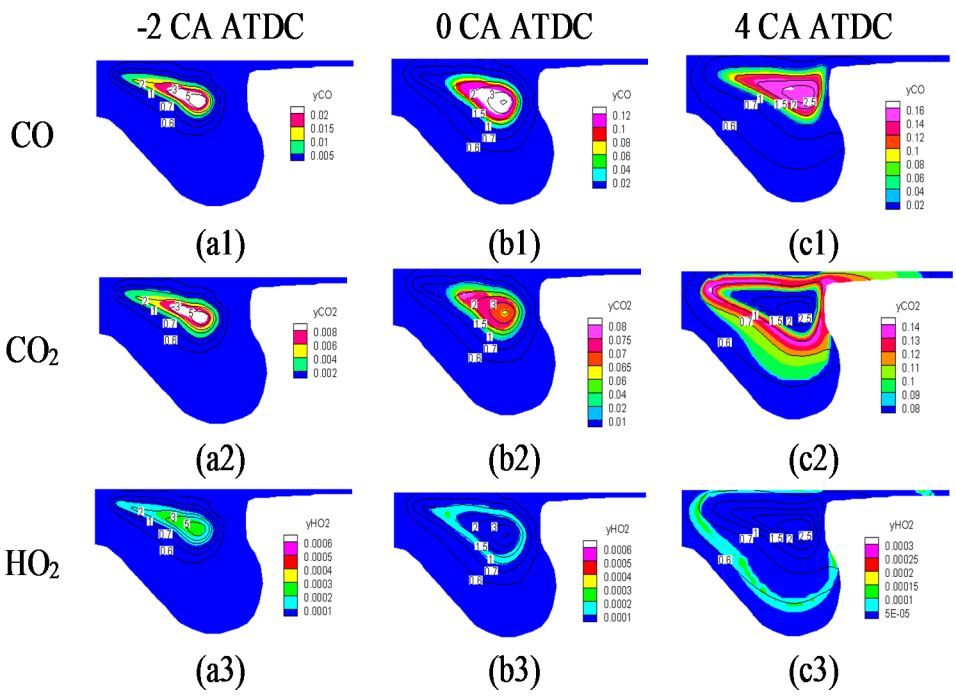

Figure 61. Mass fraction contours of CO (a1-c1), CO_2 (a2-c2) and HO_2 (a3-c3) at -2, 0 and 4 CA ATDC for the 97% methane case. Black lines in each figure indicate ϕ contours (0.3 to 3).

Three combustion zones for the dual-fuel combustion can be qualitatively identified by deconstructing the HRR diagram based on the temporal mass profiles of some relevant species. Figure 62 presents the mass profiles of several such species for the 97% methane case. As indicated, the rich premixed combustion mostly occurs between -5° to 3° ATDC, and is characterized by the consumption of n-heptane and the production of C_2H_2, CO and other intermediate species, such as H_2. As indicated in Figure 62(a), C_2H_2 and CO species attain their peak values during this period. Based on these observations, a HRR profile corresponding to rich premixed combustion can be constructed, and is shown in Figure 62(b). Similarly, from the methane mass profile, the duration for the lean premixed combustion can be defined to be between 0° to 10° ATDC. Methane is almost

completely consumed during this period, producing a significant amount of CO_2. Accordingly, a HRR profile for lean combustion can be constructed, and is also shown in Figure 62(b). Finally, C_2H_2, CO, and other species (such as H_2), which are produced during rich premixed combustion, are consumed in the diffusion combustion zone. Consequently, the HRR profile corresponding to diffusion combustion can be constructed based on this observation and the overall HRR profile. This is also shown in Figure 62(b). The diffusion combustion is estimated to occur between 0° to 60° ATDC, during which time CO_2 (cf. Fig. 13(a)) and H_2O attain their peak values.

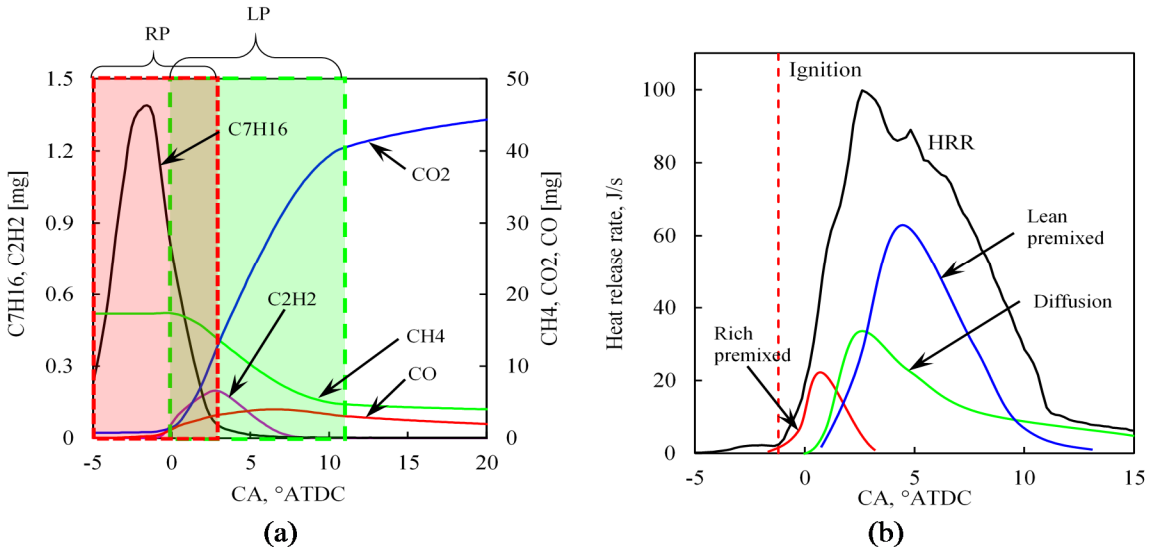

Figure 62. (a) Temporal mass profiles of n-C_7H_{16}, C_2H_2, CH_4, CO and CO_2 for the 97% methane case and (b) computed overall HRR profile and the qualitative HRR profiles for the rich premixed (RP), diffusion, and lean premixed (LP) combustion, constructed based on the species profiles.

As stated earlier, methane profiles (cf. Figure 53) indicate the extinction of lean combustion zone for the 90% methane case. This is further confirmed by analyzing the HO_2 contour plots for the two dual-fuel cases. As shown in Figure 63, for both cases, HO_2 contours at 2° ATDC indicate the presence of a lean propagating flame in the piston bowl. For the 90% methane case, however, this flame gets extinguished due to ultra lean conditions, with $\phi \approx 0.05$-0.1 ahead of the flame. The extinction is clearly illustrated by HO_2 contour plots at 7° and 9° ATDC. In contrast, the contour plots for the 97% case indicate a lean propagating flame with $\phi \approx 0.5$. Consequently, most of methane gets consumed through lean premixed combustion for this case, while a significant amount of methane remains unreacted for the 90% case. This is further confirmed by the methane mass profiles in Figure 53, discussed earlier. Note that a small amount of methane remains unreacted for the 97% case also, but that is mostly confined to the crevice and boundary layer regions. These regions also contribute to UHC and CO emissions.

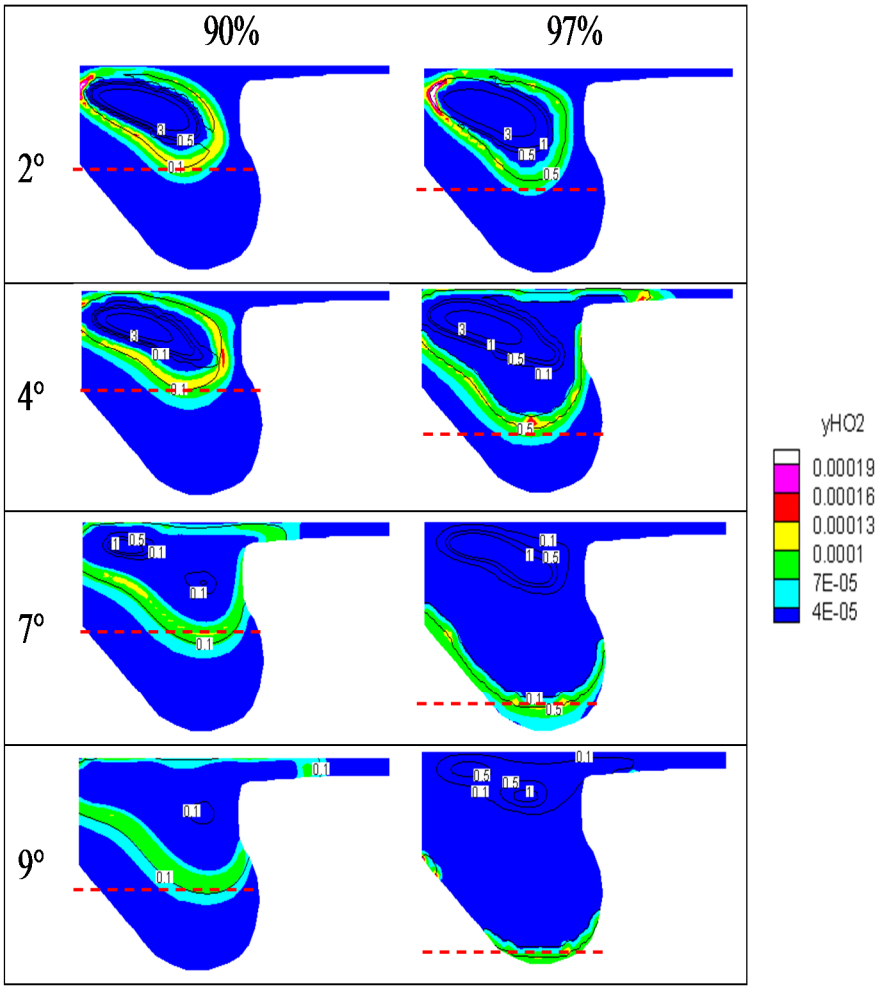

Figure 63. HO_2 mass fraction contours at different crank angles for the 90% and 97% methane cases. Black lines indicate ϕ contour. Red line in each figure is used to show the flame propagation.

6.2.2 Effect of Methane on Dual-Fuel Engine Emissions

Two performance parameters, i.e., IMEP (indicated mean effective pressure) and thermal efficiency determined from simulation results, are provided in Table 6 for the three cases. As indicated, the presence of methane at low load can adversely affect the engine performance. Both IMEP and thermal efficiency are lower for the 90% methane case compared to the 0% case. This

is consistent with the pressure and HRR profiles in Figure 53, which indicate lower peak pressure and HRR values for the 90% case. The loss of performance can be attributed to the incomplete combustion of methane at low load. In contrast, at high load (97% methane), methane is almost completely consumed through lean premixed combustion, and, the engine performance can be maintained or even enhanced with dual-fuel operation.

The effect of methane on emissions is depicted in Figure 64, which plots the specific emission (mass normalized by the work output) of soot, NO_x, UHC, and CO with respect to crank angle for the three cases. As indicated, the specific soot mass at EVO (exhaust valve opening at 116° ATDC) for the 90% methane case is reduced by a factor of 7 compared to the 0% methane case, while NO_x at EVO is increased by 2.3%. Thus the dual-fuel operation at low load can significantly reduce soot emission without affecting NO_x emission. However, there is a considerable increase in UHC and CO emissions due to incomplete combustion of methane for the dual-fuel case. Results at high load (97% methane) also indicate significant reduction in soot emission, but NO_x emission increases due to higher temperatures. In addition, CO emission decreases for this case, while UHC emission is slightly higher due to some unreacted methane in the crevice and boundary layer regions.

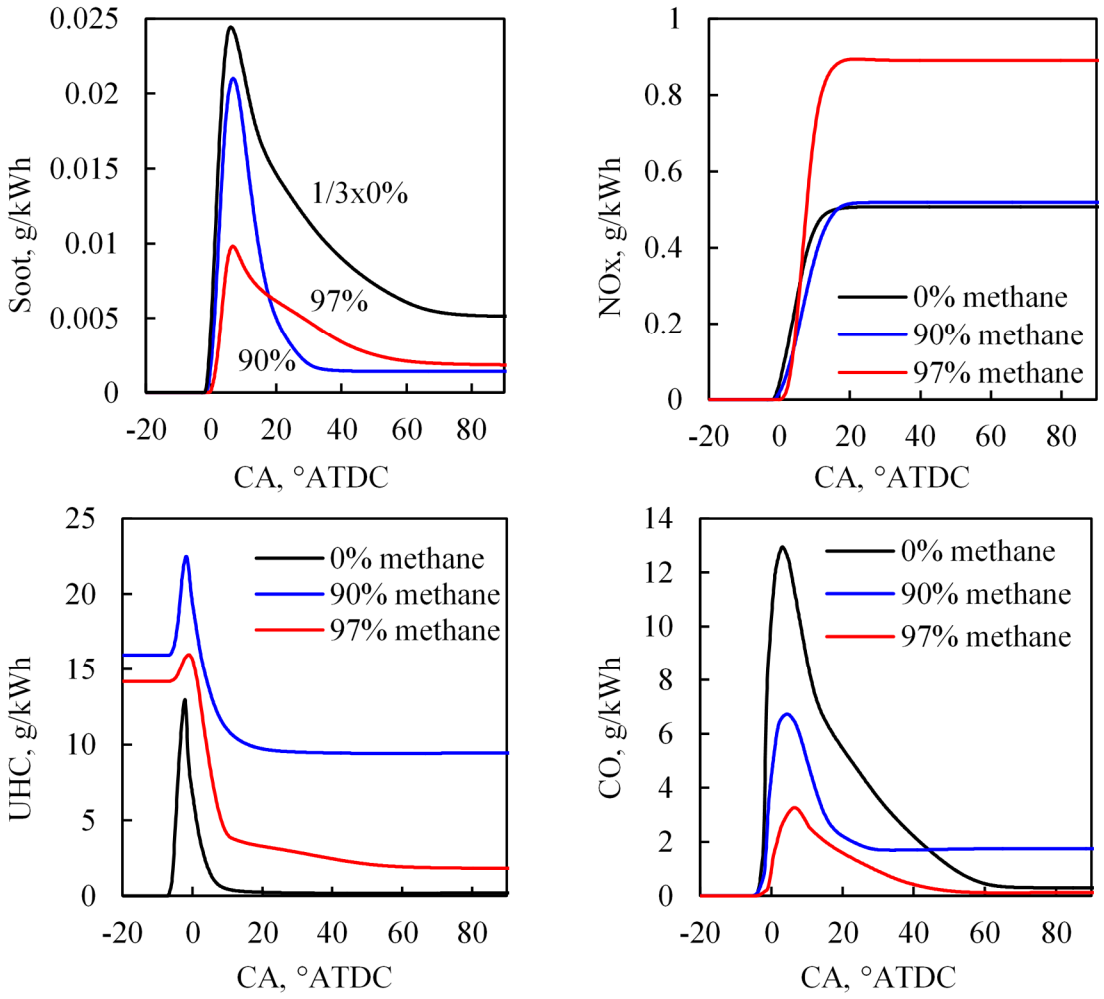

Figure 64. Normalized mass profiles of soot, NO_x, UHC (unburned hydrocarbon), and CO with respect to crank angle for the 0, 90, and 97% methane cases.

Figure 65 presents the mass fraction contours of soot and NO_x at 4° ATDC for the three cases. The comparison of these plots with the corresponding CO and CO_2 contour plots (cf. Figs. 10-12) indicates that most of soot is produced in the rich premixed combustion region, while most of NO_x is produced in the diffusion combustion region, characterized by high temperatures. This is confirmed by the fact that high soot region corresponds to high CO region, while high NO_x

region corresponds to high CO_2 region. The contour plots also provide insight into the effect of methane on soot and NO_x emissions. For instance, the reduction in soot for the dual fuel cases is due to the fact that the extent of rich premixed region is considerably reduced due to the decreased amount of n-heptane. However, the NO_x emission increases at high load due to higher temperatures in the diffusion combustion region.

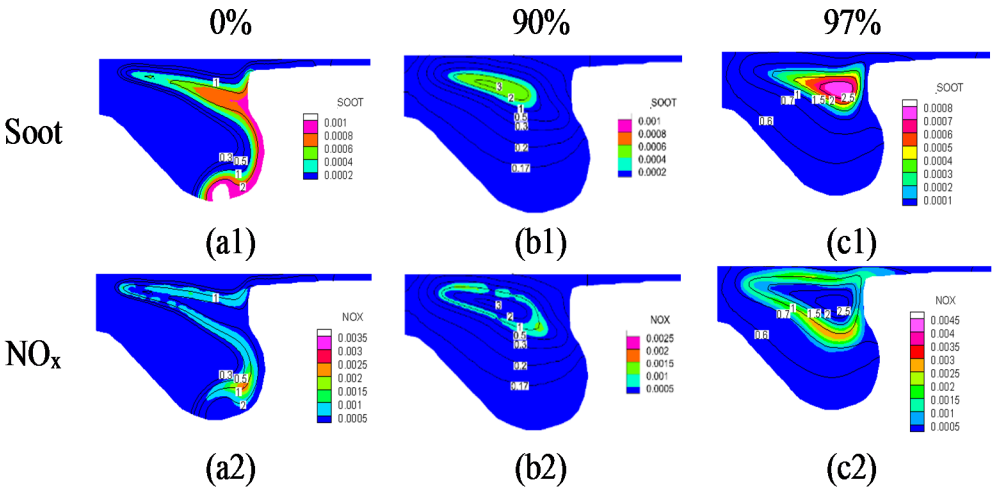

Figure 65. Mass fraction contours of soot (a1-c1) and NO_x (a2-c2) at 4 CA ATDC for the 0%, 90% and 97% methane cases.

6.3 DUAL FUEL ENGINE OPTIMIZATION STRATEGY

Simulations are carried out for medium and high load conditions. Low load conditions were not considered, as results indicated significant amount of unburned methane due to incomplete combustion. For both medium and high load, simulations were performed for different values of SOI and n-heptane energy content. The objective was to determine the minimum n-heptane energy content and an optimum operating condition in terms of SOI. Various parameters for these simulations are listed in Table 7. As indicated, five cases were considered at medium load, and

three cases were considered at high load. The five medium load cases are considered based on the 97% methane case, M16 in Table 7. Two target IMEPs (Indicated Mean Effective Pressure) of 750 and 1000 kPa were used to represent the medium and high load conditions, respectively. The energy content of n-heptane is defined as

$$r_{hept} = \frac{m_{hept} \times LHV_{hept}}{m_{met} \times LHV_{met}} \times 100\%$$

where m_{hept} and m_{met} represent the mass of n-heptane and methane, respectively. LHV_{hept} and LHV_{met} are the lower heating values of the two fuels. For each value of n-heptane energy content, simulations were performed by sweeping the SOI from -30 to 0° ATDC to determined an optimum point in terms of thermal efficiency.

Table 7. Case information for dual-fuel engine simulation (units are based on per cylinder per cycle)

Engine Load	Medium					High		
Target IMEP (kPa)	750					1000		
Energy input (J)	1014					1535		
Name	M6	M7	M8	M12	M16	H4	H5	H7
Energy ratio of n-heptane	6%	7%	8%	12%	16%	4%	5%	7%
CH4 (mg)	19.2	19.0	18.8	18.0	17.3	29.6	29.2	28.5
CH4/air equivalence ratio	0.64	0.64	0.63	0.60	0.58	1.04	1.03	1.00
N-heptane (mg)	1.3	1.5	1.7	2.5	3.3	1.3	1.7	2.5
Optimized SOI (° ATDC)	N/A	-11	-10	-7	-5	N/A	-15	-10

Figure 66 presents the thermal efficiency versus SOI for the five n-heptane cases at medium load (M6 to M16). The corresponding IMEP plots are shown in Figure 67. As indicated in Figure 66, the peak thermal efficiency for the M6 case is 33.1% while that for the other four cases varies in a narrow range, from 38.7% to 39.4%. For each case, the peak efficiency is indicated by the diamond symbol. The low efficiency for case M6 can be attributed to the fact that following ignition, complete combustion could not be sustained in methane-air mixtures for all the SOI considered for this case. Consequently, only the other four cases are considered in further discussion. Since the engine efficiency and NO_x emissions generally have a trade-off relationship, an optimal operation condition can achieve relative high efficiency and low NO_x. For each case, an optimal SOI can be determined based on the peak thermal efficiency, and is indicated by symbols in Figure 66 and Figure 67. Thus the optimum SOI values are -11°, -10°, -7° and -5° ATDC for sets M7, M8, M12 and M16 respectively.

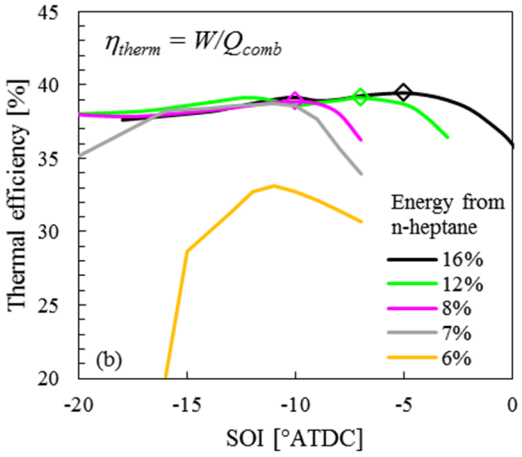

Figure 66. The thermal efficiency versus SOI for the medium load n-heptane cases. Diamond symbols represent the optimized SOI values corresponding to the peak thermal efficiency and the CA50 close to 10° ATDC.

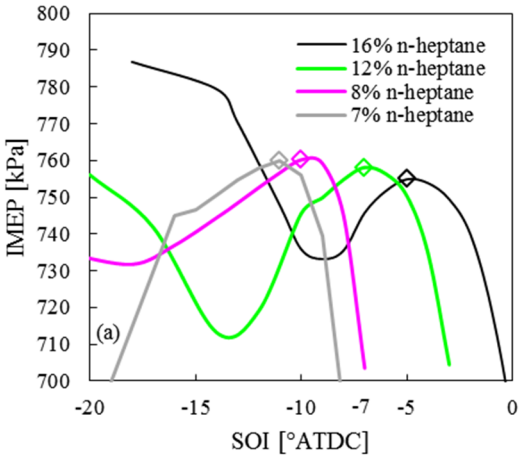

Figure 67. The IMEP versus SOI for the medium load n-heptane cases. Diamond symbols represent the optimized SOI values corresponding to the peak thermal efficiency and the CA50 close to 10° ATDC.

In order to explain the existence of an optimum SOI, detailed results are provided for one representative case (M8). Figure 68 presents the mass fraction contours of methane and n-heptane vapor (indicated by black lines) at various crank angles for three different SOIs, -16, -10 and -7 °ATDC for the M8 case. The initial methane mass fraction is 0.035. For each SOI, the contours are plotted at three crank angles, with the first one near the occurrence of ignition, the second near the completion of combustion, and the third near the cycle end. Details of the two-stage ignition process in a dual-fuel engine have been discussed in a previous section. Based on the temporal variation of heat release rate and OH and QOOH (alkyl hydroperoxy) mass fractions, the first-stage ignition was found to occur -11.0, -6.5 and -3.5°ATDC, and the second-stage ignition at -6, -2 and 0°ATDC, corresponding to the -16, -10 and -7°ATDC SOIs, respectively. Thus the ignition delay progressively decreases as the SOI is retarded, since the injection occurs in increasingly higher pressure and temperature ambient.

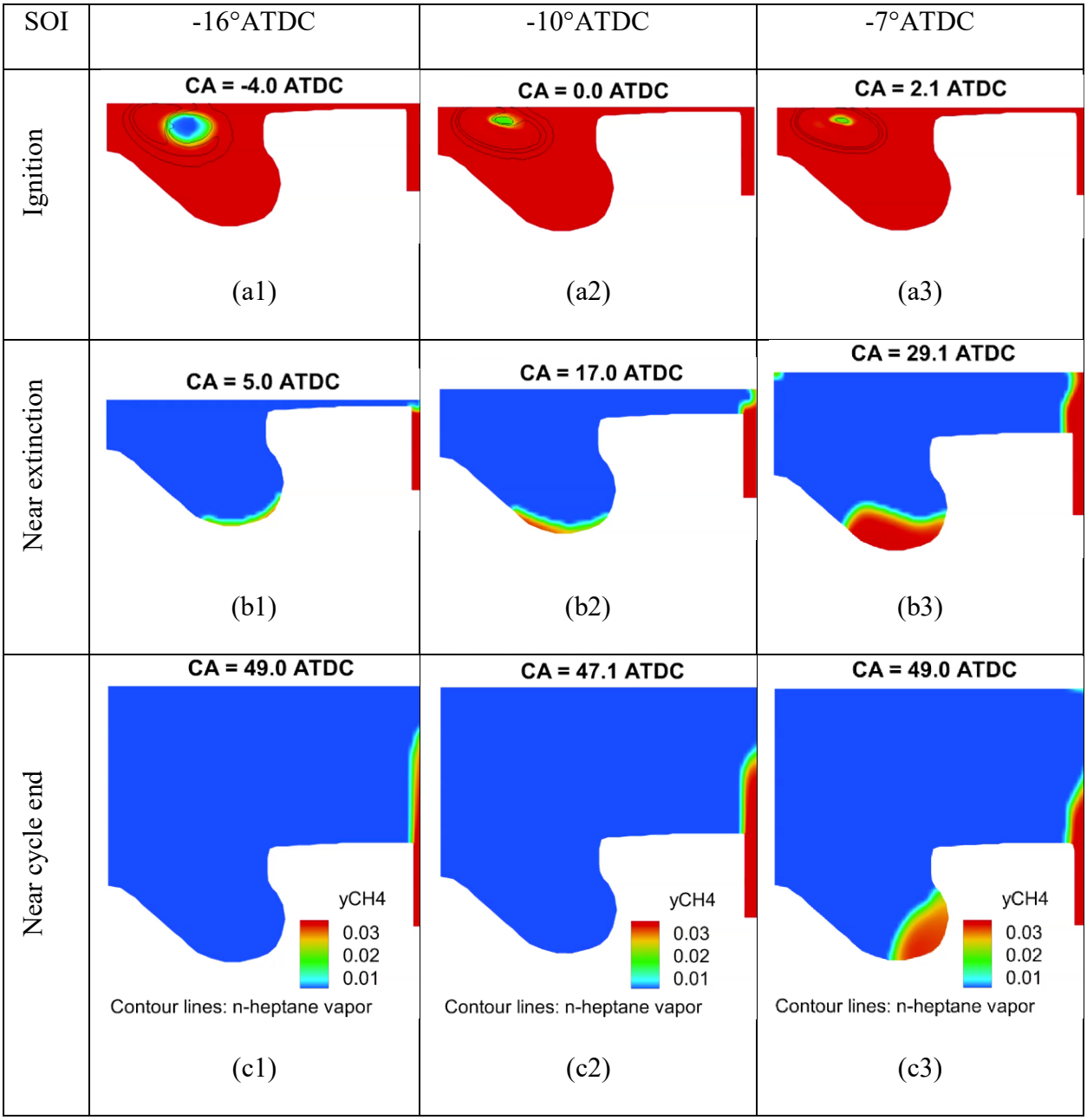

Figure 68. Methane mass fraction (between 0.01 to 0.03) contours at the center cut plane for the M8 case with three different SOIs, -16, -10 and -7°ATDC. For each SOI, plots are shown near ignition (a1-a3), near extinction (b1-b3) and near cycle end (c1-c3). Black lines in Fig. a1-a3 indicate n-heptane vapor mass fraction contours.

Black contour lines for the n-heptane vapor in Figs. a1-a3 essentially envelope the ignition kernel and indicate the rich premixed combustion zone containing mostly unburned mixture. As the temperature and OH mass fraction increase rapidly during ignition and rich premixed combustion of n-heptane, it leads to ignition in methane-air mixtures, followed by rapid consumption of methane via lean premixed flame propagation. The combustion region continues to propagate until the flame front reaches the bottom of the piston bowl shown in Figs. b1-b3.

A more notable difference between the three SOI cases is that for the first two SOIs (-16 and -10° ATDC), the methane is completely consumed, except for a small amount trapped in the crevice region, whereas for the third case (SOI=-7°ATDC), a small amount of methane remains unburned near the bottom of the piston bowl. Since the total input energy is the same for these cases, the thermal efficiency is reduced for the -7° SOI case, as indicated in Figure 67. On the hand, for the -16° SOI case, a significant amount of heat release occurs during the compression stroke near TDC (between -4 to 0°ATDC), while for the -10° SOI case, most of the heat release occurs during the expansion stroke near TDC. This is further confirmed by the CA50 values (crank angle corresponding to 50% of the total heat release), which are 2.4, 9.2 and 16.0° ATDC for -16, -10 and -7° SOI cases, respectively. Consequently, the efficiency is lower for -16° case compared to the -10° case. Thus SOI=-10°ATDC represents the optimum value for the M8 set.

Figure 69 presents the effect of SOI on specific soot, NO_x, HC and CO emissions at EVO (exhaust valve opening at 116° ATDC) for the medium load n-heptane cases at. As indicated, for each n-heptane case, each optimum SOI point is characterized by relatively low amounts of soot, NO_x and HC emission. As the SOI is retarded, the soot and HC emissions first increase and then decrease, while NO_x emission decreases monotonically. The variation in HC and CO emission correlates with the amount of unburned methane at EVO, while that in NO_x follows the cylinder

temperature, which decreases monotonically as the SOI is retarded. In addition, Figure 69 indicates that as the amount of pilot fuel is reduced, the soot, HC and CO emissions at the optimum SOI point decrease considerably, while the NO_x emission increases slightly. These trends in emissions are not surprising since methane combustion produces very little soot compared to n-heptane. Note that the present study employs a C_2H_2 based soot model and the extended Zeldovich mechanism for the NO_x formation. Consequently, the results concerning soot and NO_x emissions should be considered qualitative only.

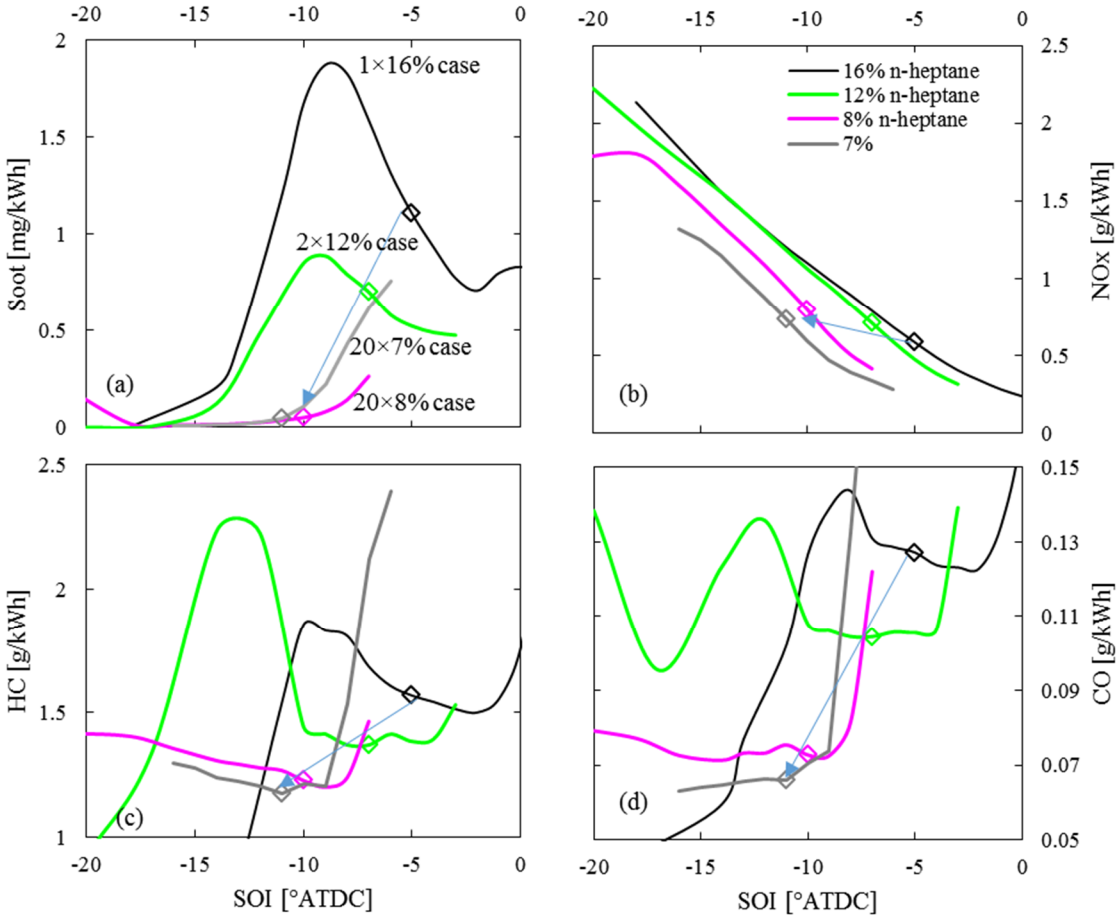

Figure 69. Specific Soot, NO_x, HC and CO emissions plotted versus SOI for the four medium load dual-fuel cases. Diamond symbols represent the optimized SOI values

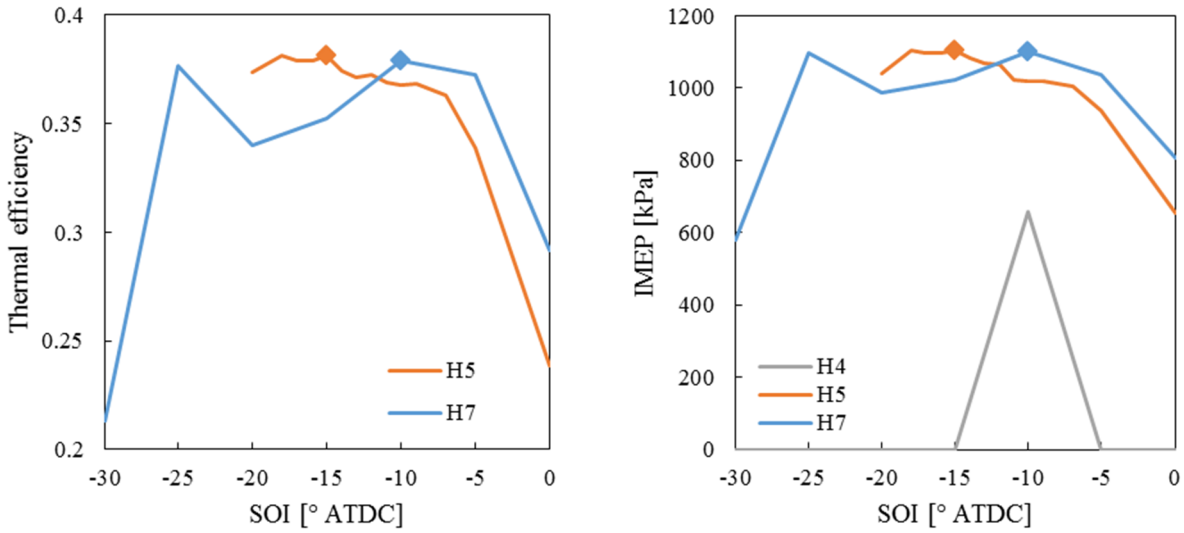

Figure 70. Thermal efficiency (a) and IMEP (b) versus SOI for the high load cases. Diamond symbols represent the optimized SOI values corresponding to the peak thermal efficiency and IMEP.

Figure 70 presents the thermal efficiency and IMEP versus SOI for the three high load n-heptane cases (H4, H5 and H7). Note that for the H4 case, combustion could not be sustained in methane-air mixtures for most of SOIs investigated. Thus, the minimum amount of pilot fuel (n-heptane) for sustained combustion is 5% (in terms of energy content) at high engine load. For the other two n-heptane cases, the peak thermal efficiencies are 34.3% and 37.9% corresponding to the optimum SOI values of -15° and -10° ATDC for the H5 and H7 cases, respectively. The thermal efficiency values at high load are generally lower than those at medium load conditions (between 38.7% and 39.4%). The reason is that at high load, simulations were carried out at slightly rich conditions, with global equivalence ratio considering both methane and n-heptane being near 1.08. The peak IMEP values are 1103 and 1099 for the H5 and H7 cases, respectively. Therefore, the 5%

n-heptane case appears more desirable since it produce slightly higher power output but requires less liquid fuel.

Figure 71 presents the soot, NO_x, UHC and CO specific emissions plotted versus SOI for the high load cases. For both the cases, the diamond symbol indicates the optimum SOI as discussed in the context of Figure 70. For the optimum SOI, as the amount of pilot fuel is reduced, soot and NO_x emissions decrease, while UHC emission increases, and CO emission remains essentially the same. These values indicate that the soot and UHC emissions are minimal, but the NO_x and CO emissions are significant due to high temperatures at high load and rich mixture condition. As the SOI is retarded, the amount of soot is increased. But the NO_x, UHC and CO all experience non-monotonic variation. Note that the cases with SOI earlier than -20° for H7 and -25° for H5 do not have sustainable combustion, so the decreased NO_x, increased UHC and CO are all due to the missed or weak combustion. An important benefit of the high load operation is that the methane trapped in the crevice region can be consumed to produce lower amount of UHC compared to medium load. Figure 72 presents the contour plots of methane for set H5, case SOI = -15°ATDC at four crank angles. The methane is ignited at -2°ATDC and propagates to the bottom of the piston bowl at 5°ATDC. From 5 to 15°ATDC, the methane in the crevice is consumed through combustion. As depicted in Figure 72 at 50°ATDC, the mass fraction of methane is less than 0.01 in the crevice.

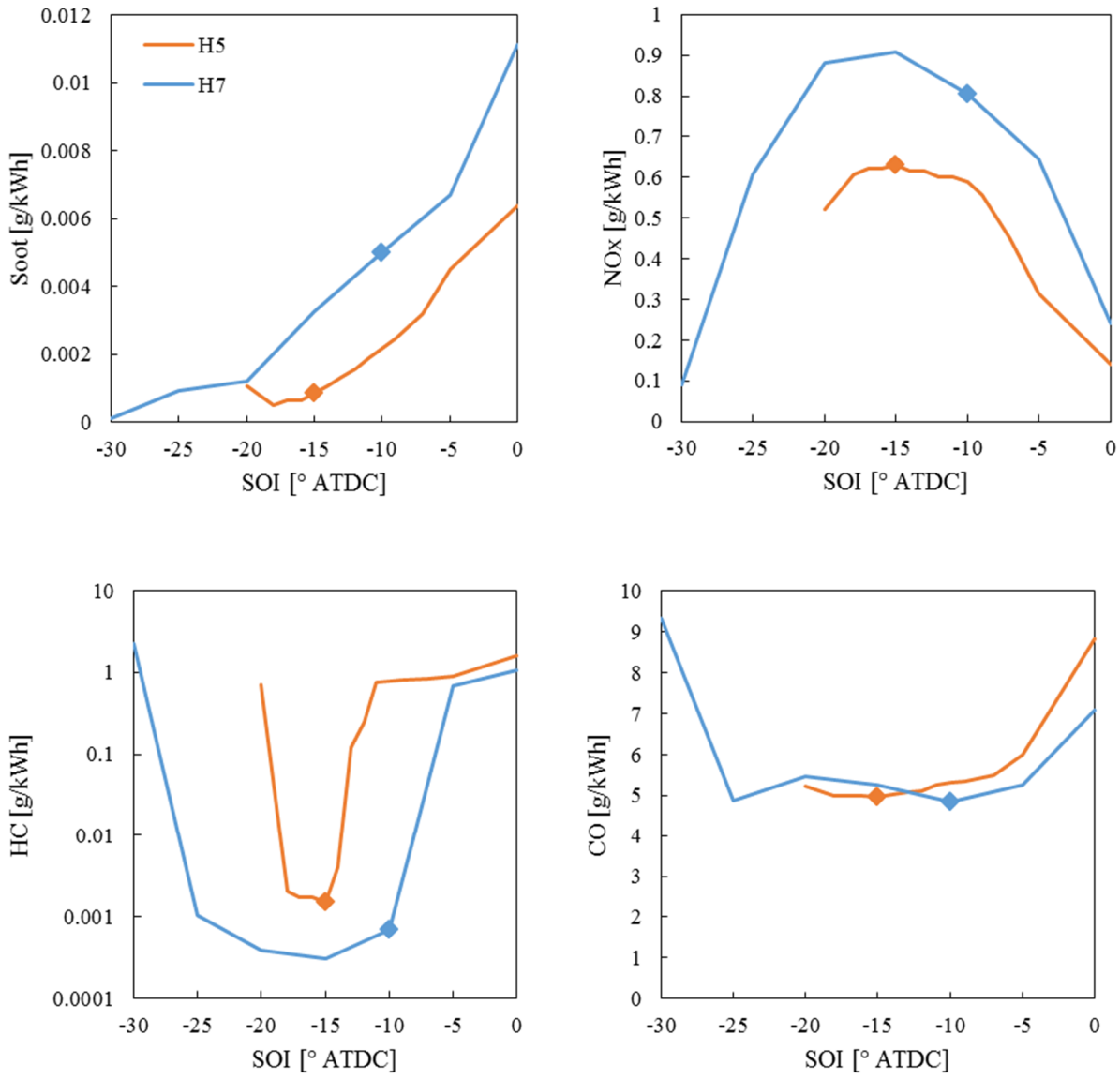

Figure 71. Specific Soot, NO_x, HC and CO emissions plotted versus SOI for the high load dual-fuel cases. Diamond symbols represent the optimized SOI values.

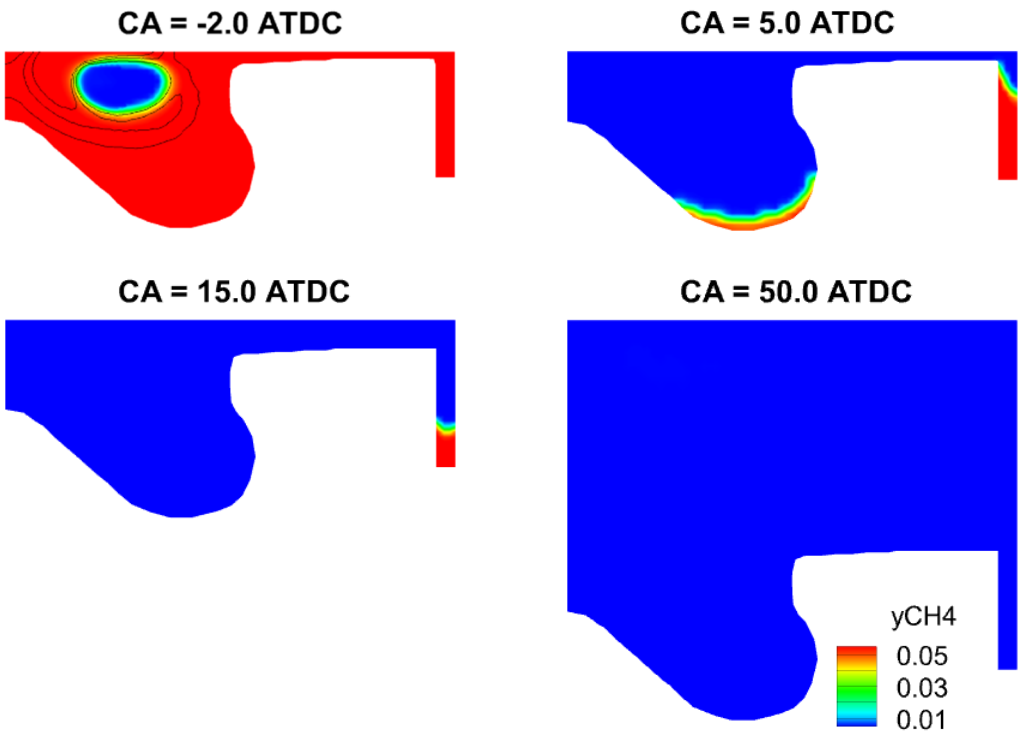

Figure 72. Methane mass fraction (from 0.01 to 0.05) contours at the center cut plane for the H5 case with SOI = -15°ATDC. Plots are shown at crank angles near ignition, during flame propagation, near the end of combustion, and near cycle end. Black lines at CA=-2°ATDC represent n-heptane vapor mass fraction contours.

7 CONCLUSION AND FUTURE WORK

7.1 EFFECT OF FUEL UNSATURATION

In the first part of the thesis, the effects of a double bond in the fuel molecular structure have been analyzed in 1-D counterflow laminar flames and 3-D turbulent spray flames. Partially premixed flames (PPFs) burning n-heptane and 1-heptene fuels in a counterflow configuration have been simulated in order to examine the hypothesis that the increased NO_x from the combustion of biodiesel fuel components and increased soot from unsaturated long chain hydrocarbons can be related to the presence of the double bond in the fuel molecular structure. The 1-D computational model has been validated using previously reported measurements of PPFs and NPFs. The NO emission for the two fuels is characterized in terms of the emission index for different levels of partial premixing. Soot formation processes considered in the model include nucleation, surface growth, oxidation, and coagulation, based on the Frenklach method of moments approach. The important conclusions are as follow:

(1) For both fuels, the global flame structure is characterized by a rich premixed reaction zone (RPZ) on the fuel side and a nonpremixed reaction zone (NPZ) located close to the stagnation plane or on the oxidizer side. The fuel is completely pyrolyzed/oxidized to produce CO, H_2, and hydrocarbon species (including C_2H_2) in the RPZ, while the NPZ is characterized by the oxidation of CO and H_2. PAH species are formed mainly in the region between RPZ and stagnation plane. The soot formation zone is also located in this region, in which the nucleation is initiated through pyrene formation, and then the particle diameter, soot number density and

volume fraction increase continuously to their peak values. The soot oxidation mainly occurs downstream of the stagnation plane.

The β scission and oxidation reactions related to the double C=C bond lead to higher amount of acetylene and thus increased NO through the prompt mechanism in 1-heptene flames compared to that in n-heptane flames. However, differences in the amount of NO formed for the two fuels generally become less pronounced as the level of partial premixing is reduced, or the equivalence ratio is increased towards the diffusion flame limit ($\phi=\infty$).

(2) Results also indicate that the NO emission index decreases monotonically with the increase in ϕ. Analysis of the various NO production pathways indicate that the total NO formed is mainly due to the prompt and intermediate N_2O mechanisms, followed by the NNH and thermal NO mechanisms.

(3) The presence of double bond results in significantly higher PAH and soot emissions in 1-heptene flames compared to that in n-heptane flames. This is related to the increased production of C_2H_2 and C_6H_6 as a direct consequence of β scission reactions due to the presence of double bond in 1-heptene.

(4) The PAHs and soot emissions are also strongly influenced by the level of premixing and strain rate. As the premixing level is reduced, or as ϕ is increased, the RPZ becomes weaker compared to NPZ, and move closer to the stagnation plane, while the NPZ moves away from the stagnation plane toward the oxidizer nozzle. Thus the spatial separation between the two reaction zones decreases. However, the concentrations of C_2H_2 and PAH species increase, and, consequently, the amount of soot increases, while soot oxidation decreases, with the increase

in ϕ. The effect of fuel unsaturation on PAH and soot emissions becomes more pronounced as the level of premixing and/or the strain rate is reduced.

(5) The reaction path analysis indicates two major routes for benzene formation in the RPZ. The main route is through the recombination reaction of propargyl radicals, which are mostly formed from allyl radicals. The other route is through the reaction of vinyl with butadiene. The presence of double bond leads to the increased concentrations of propargyl and butadiene, and thereby significantly more benzene in 1-heptene flames than in n-heptane flames. The presence of double bond increases the amount of C_2H_2 in 1-heptene flames, since C_2H_2 is produced mainly from C_2H_4 and C_4H_5, and C_4H_5 concentration is noticeably higher in 1-heptene flames. C_2H_2 and C_6H_6 are major precursors for pyrene, while C_2H_2 also plays an important role in soot surface growth through the HACA mechanism. Thus the presence of double bond promotes β scission reactions leading to the increased production of C_2H_2, C_6H_6, and $C_{16}H_{10}$, and thereby higher soot emission in 1-heptene flames.

The 3-D CFD software CONVERGE has been used to examine the effects of fuel unsaturation on NO_x and PAH formation of n-heptane and 1-heptene spray flames at diesel engine conditions. The directed relation graph with error propagation and sensitivity analysis has been employed to develop a reduced kinetic mechanism (with 207 species and 4094 reactions), starting from the detailed CRECK mechanism containing 482 species and 19072 reactions. The mechanism and spray models have been validated against the shock tube ignition data and high-fidelity spray data in a constant-volume combustion vessel from the Engine Combustion Network (ECN). Important observations are as follows.

(1) Validation of the reduced mechanism for the ignition of n-heptane/air and 1-heptene/air mixtures indicates fairly good agreement between the predictions and measurements. The

mechanism also shows good agreement with other detailed or reduced mechanisms, and reproduces the experimentally observed negative temperature coefficient (NTC) behavior for n-heptane/air mixtures. In addition, results indicate that at moderate temperatures (800<T<1100), ignition delays for 1-heptene are significantly higher than those for n-heptane, but similar at high temperatures. Validations of the 3-D simulations against the ECN data for n-heptane sprays also show good agreement between the predicted and measured spray penetration lengths, ignition delays, flame lift-off lengths, and global flame structure.

(2) Simulation results for n-heptane and 1-heptene spray flames indicate that the combustion under diesel engine conditions is characterized by a double-flame structure with a rich premixed reaction zone (RPZ) near the flame stabilization region and a non-premixed reaction zone (NPZ) further downstream. The RPZ and NPZ are characterized, respectively, by the high concentrations of C_2H_2 and OH species.

(3) The scatter plots in ϕ-T space are used to identify the dominant NO_x and PAH formation regions in spray flames. For the conditions investigated, most of NO_x is formed via thermal NO route in the NPZ, while PAH species are mainly formed in the RPZ. Relatively small amount of NO is also formed via prompt route in the RPZ, and via N_2O intermediate route in the fuel-lean region outside NPZ, and via NNH intermediate route in the region between RPZ and NPZ.

(4) The presence of a double bond results in β scission reactions e.g. reactions $C_7H_{14}+OH=>CH_2CHCH_2+C_4H_8+H_2O$ and $C_7H_{14}=>CH_2CHCH_2+C_4H_9$, to form allyl radicals (CH_2CHCH_2), which produce the heat in a short period of time. Thus the increased temperature due to the presence of the double bond leads to higher amount of NO in 1-heptene flame than that in n-heptane flame.

(5) The presence of double bond also leads to the significantly higher amounts of PAH species, implying higher soot emission in 1-heptene flame compared to that in n-heptane flame. Reaction path analysis indicates that this can be attributed to β scission reactions due to the presence of double bond, which lead to the significantly higher amounts of 1,3-butadiene and allene formed in 1-heptene compared to those in n-heptane. Moreover, the presence of the double bond in 1-heptene opens an additional route for allene formation through 1,3-butadiene (C_4H_6) and 3-butenal (C_3H_5CHO) species.

The results from 1D counterflow flame simulations and 3D CFD spray flame calculations both conclude that 1-heptene produces higher amounts NO_x and PAH compared to n-heptane. Although the flow characteristics and geometry for the two types of flames are different, the presence of the double bond implies higher probability of β scission reactions, which results in the observed behavior discussed above. Therefore, an important result from this research is that unsaturated fuels can produce higher amounts of NO_x and soot than saturated fuels. It is thus recommended to reduce the amount of unsaturation in the fuel molecular structure to reduce NO_x and soot emissions in diesel engine applications.

7.2 DUAL-FUEL DIESEL ENGINE COMBUSTION

The second part of the thesis focuses on a numerical investigation on the effects of gaseous fuel on the ignition, combustion, and emission characteristics in a dual-fuel diesel engine. Methane and n-heptane are considered as surrogates for CNG and diesel fuels, respectively. Methane mixed with air is introduced into the cylinder through the intake valve, while n-heptane is injected directly and compression ignited. Engine CFD simulations are performed using CONVERGE and a reduced mechanism containing 42 species and 168 for a 1/7th sector of the cylinder of a 1.9L GM diesel engine. The effects of methane on the first- and second-stage ignition processes, and on the

modification of dominant combustion modes in a diesel engine are analyzed. A guideline for the dual-fuel engine development and optimization is provided through a sweep over a range of of pilot fuel injection and injection timing. Important observations are as follows.

(1) The first- and second-stage ignition processes in diesel sprays are characterized by analyzing the spatial and temporal evolution of alkyl hydroperoxy (QOOH) and OH radicals. Results indicate a spatially wide ignition kernel for both the single- and dual-fuel cases. The first-stage ignition occurs near the fuel injector over a narrow temperature range ($T\approx850$-$900K$), but a wide range of equivalence ratio ($\phi\approx0.3$-0.8). In contrast, the second-stage ignition occurs in the tip region of the fuel jet with $T\approx1050$-$1100K$, and $\phi=1.0$-4.0.

(2) The two-stage ignition behavior associated with n-heptane remains qualitatively the same even at high molar fractions of methane. While the presence of methane increases both the first- and second-stage ignition delays, the effect is more pronounced on the latter. The increase in first ignition delay is due to the reduced O_2 concentration resulting from the addition of methane, while that in second ignition delay is attributable to both the lower O_2 concentration and the chemical effect of methane. The latter is mainly due to reaction $CH_4 + OH = CH_3 + H_2O$, which depletes OH.

(3) As expected, the addition of methane has a significant effect on engine combustion. For the single-fuel (n-heptane) case, the heat release occurs through a hybrid combustion mode involving rich premixed combustion and diffusion combustion. On the other hand, the heat release in a dual-fuel engine also involves lean premixed combustion with a propagating flame. Based on the simulation results, a modified heat release rate diagram is constructed, illustrating the three combustion modes with respect to crank angle.

(4) The effect of methane on engine performance and emissions depends on the operating conditions. Results indicate that the dual-fuel operation at high load conditions can provide significant reduction in soot and CO soot emissions (g/kwh). The thermal efficiency is also slightly improved, but NO_x emission increases due to high temperatures in the diffusion combustion region. The dual fuel strategy does not seem to be effective at low load due to the incomplete combustion of methane, resulting in lower thermal efficiency and higher UHC and CO emissions.

The minimum amounts of pilot fuel (in terms of energy content) required for stable engine operation are found to be 7% and 5% at medium load and high load, respectively. For a given pilot injection, the optimum point to achieve the maximum thermal efficiency is also determined. As the amount of liquid fuel is decreased, the SOI should be advanced to achieve high efficiency and low emissions. In particular, the SOIs of -11° at medium load and -15° ATDC at high load yield the lowest soot emission, while the NO_x, UHC and CO emissions are also relatively low. Considering both efficiency and emissions, the optimum SOI and minimum amount of liquid fuel are two important factors in searching for the best operating condition for the dual-fuel engine.

7.3 FUTURE WORK

Although the results here demonstrated the major effects of the fuel unsaturation and the optimization of dual-fuel diesel engine strategy, the topics could be further expanded in various ways.

First, the study on the unsaturation in the fuel molecular structure has only been focused on n-heptane and 1-heptene fuels. It would be necessary to study the effects of unsaturation for shorter or longer hydrocarbon chain species. The hypothesis that the unsaturation results in

increased NO_x and soot might still be true for longer hydrocarbon chains but may become invalid as the hydrocarbon chain becomes too short.

Moreover, this work demonstrated how NO_x and soot are formed and proposed the possible way to reduce NO_x and soot emissions by reducing the degree of unsaturation. However, a practical approach to reduce the unsaturation in bio-derived fuels would be an essential research topic as bio-fuels become more and more popular.

Thirdly, the soot formation in this study only focuses on the formation of the primary particles. To further expand the capability of the soot emission prediction, it would be necessary to study and include the aggregation process in the soot formation model. Also the reduced mechanism developed during this study has the capability of predicting PAH up to pyrene, which is essential to the method of moments soot formation model or section model through pyrene in 3D CFD simulations. So an interesting future work topic would be to calibrate the PM models in Converge using the reduced mechanism and analyze the soot formation process in engine simulations.

Last but not the least, for the dual-fuel engine operation, one important optimization approach is the exhaust gas recirculation (EGR). It would be a very effective approach to bring down the cylinder peak temperature and reduce NO_x emissions. Combining the strategy developed in this work to reduce PM emissions, the dual-fuel engine would become a promising alternative for the future transportation industry.

8 REFERENCE

1. Assessment of Fuel Economy Technologies for Light-Duty Vehicles, National Research Council, 2011, ISBN 978-0-309-15607-3.
2. Graboski, M. S., McCormick, R. L.. Prog. Energy Combust. Sci. 1998, 24, 125–164.
3. McCormick, R. L., Graboski, M. S., Alleman, T. L., Herring, A. M. Environ. Sci. Technol. 2001, 35, 1742–1747.
4. National Renewable Energy Laboratory (NREL). Biodiesel Handling and User Guide; NREL: Golden, CO, 2009; NREL/TP-540-43672.
5. Mueller, C., Cheng, E., Boehman, A. An introduction to biodiesel. SNL CRF News 2006, 28 (May/June), 3.
6. Stotler, R., Human, D. Transient Emission Evaluation of Biodiesel Fuel Blend in a 1987 Cummins L-10 and DDC 6V-92-TA, National Biodiesel Board: Jefferson City, MO, Nov 30, 1995, ETS Report ETS-95-128.
7. Sharp, C. A. Transient Emissions Testing of Biodiesel in a 6V-92TA DDEC Engine, National Biodiesel Board: Jefferson City, MO, Oct 1994, Southwest Research Institute Report 6602 and 6673.
8. Graboski, M. S., McCormick, R. L., Alleman, T. L. The Effect of Biodiesel Composition on Engine Emissions from a DDC Series 60 Diesel Engine, National Renewable Energy Laboratory (NREL): Golden, CO, 2003, NREL/SR-520-31461.
9. Fu, X., Garner, S., Aggarwal, S., Brezinsky, K. Energy and Fuels. 2012, 26, 879–888.
10. Fu, X., Han, X., Brezinsky, K., Aggarwal, S. Energy and Fuels. 2013, 27, 6262–6272.
11. Lapuerta, M., Herreros, J. M., Lyons, L. L., García-Contreras, R., Briceño, Y. Fuel. 2008, 87, 3161−3169.
12. Schönborn, A., Ladommatos, N., Williams, J., Allan, R., Rogerson, J. Combust. Flame 2009, 156, 1396−1412.
13. Puhan, S., Saravanan, N., Nagarajan, G., Vedaraman, N. Biomass Bioenergy 2010, 34, 1079−1088.
14. Benjumea, P., Agudelo, J. R., Agudelo, A. F. Energy Fuels 2011, 25, 77−85.
15. Fisher, E. M., Pitz, W. J., Curran, H. J., Westbrook., C. K. Proc. Combust. Inst. 2000, 28, 1579−1586.
16. Marchese, A. J., Angioletti, M., Dryer, F. L. Flow reactor studies of surrogate biodiesel fuels. Proceedings of the 30th International Symposium on Combustion, Chicago, IL, July 2004.
17. Metcalfe, W., Dooley, W., Curran, H., Simmie, J. An experimental and chemical kinetic modeling study of surrogate diesel fuels. Proceedings of the 6th International Chemical Kinetics Conference, National Institute of Standards and Technology (NIST), Gaithersburg, MD, July 2005, Paper H2.
18. Sarathy, S. M., Gail, S., Thomson, M. J., Dagaut, P. Proc. Combust. Inst. 2007, 31, 1015−1022.
19. Garner, S., Sivaramakrishnan, R., Brezinsky, K. Proc. Combust. Inst. 2009, 32, 461−467.
20. Naha, S., Aggarwal, S. K. Combust. Flame 2004, 139, 90−105.
21. Frenklach, M., Wang, H. Proc. Combust. Inst. 1991, 23, 1559.
22. Frenklach, M. Phys. Chem. Chem. Phys. 2002, 4, 2028−2037.
23. Cho, H. M., He, B-Q. Spark ignition natural gas engines—A review. Energy Conversion & Management. 2007, 48 (2), 608 –618.
24. Felipe, O., González, C., Mahkamov, K., Silva Lora, E. E., Andrade, R. V., Jaen, R. L. Prediction by mathematical modeling of the behavior of an internal combustion engine to be fed with gas from biomass, in comparison to the same engine fueled with gasoline or methane. Renewable Energy. 2013, 60, 427–432.
25. Chandra, R., Vijay, V. K., Subbarao, P.M.V., Khura, T. K. Performance evaluation of a constant speed IC engine on CNG, methane enriched biogas and biogas. Applied Energy. 2011, 88, 3969–3977.

26. Hansen, A.C., Zhang, Q., Lyne, P.W.L. Ethanol–diesel fuel blends—a review Bioresource Technology. 2005, 96, 277–285.
27. Changwei, J., Shuofeng, W. Effect of hydrogen addition on the idle performance of a spark ignited gasoline engine at stoichiometric condition. Int. J. Hydrogen Energy 2009, 34, 3546 –3556.
28. Ma, F., Wang, Y., Liu, H., Li, Y., Wang, J., Zhao, S. Experimental study on thermal efficiency and emission characteristics of a lean burn hydrogen enriched natural gas engine. Int. J. Hydrogen Energy. 2007, 32, 5067–5075.
29. Wang, J., Chen, H., Liu, B., Huang, Z. Study of cycle-by-cycle variations of a spark ignition engine fueled with natural gas–hydrogen blends. Int. J. Hydrogen Energy. 2008, 33, 4876–4883.
30. Das, L. M., Gulati, R., Gupta, P. K. A comparative evaluation of the performance characteristics of a spark ignition engine using hydrogen and compressed natural gas as alternative fuels. Int. J. Hydrogen Energy. 2000, 25, 783–793.
31. Kahraman, N., Ceper, B., Akansu, S. O., Aydin, K. Investigation of combustion characteristics and emissions in a spark-ignition engine fuelled with natural gas–hydrogen blends. Int. J. Hydrogen Energy. 2009, 34(2), 1026–1034.
32. Dimopoulos, P., Bach, C., Soltic, P., Boulouchos, K. Hydrogen–natural gas blends fuelling passenger car engines: Combustion, emissions and well-to-wheels assessment. Int. J. Hydrogen Energy. 2008, 33, 7224–7236.
33. Morrone, B., Andrea, U. Numerical investigation on the effects of natural gas and hydrogen blends on engine combustion. Int. J. Hydrogen Energy. 2009, 34, 4626–4634.
34. Bauer, C. G., Forest, T. W. Effect of hydrogen addition on the performance of methane-fueled vehicles. Part I: effect on SI engine performance, Int. J. Hydrogen Energy. 2001, 26, 55–70.
35. Bauer, C. G., Forest, T. W. Effect of hydrogen addition on performance of methane-fueled vehicles. Part II: driving cycle simulation. Int. J. Hydrogen Energy. 2001, 26, 71–90.
36. Shirk, M. G., McGuire, T. P., Neal, G. L., Haworth, D. C. Investigation of a hydrogen-assisted combustion system for a light-duty diesel vehicle. Int. J. Hydrogen Energy. 2008, 33, 7237–7244.
37. Sahoo, B. B., Sahoo, N., Saha, U. K. Effect of H2:CO ratio in syngas on the performance of a dual fuel diesel engine operation. Applied Thermal Engineering. 2012, 49, 139–146.
38. Boehman, A. L., Corre, O. L. Combustion of syngas in internal combustion engines. Combust. Sci. and Tech. 2008, 180,1193–1206.
39. Duc, P. M., Wattanavichien, K. Study on biogas premixed charge diesel dual fuelled engine. Energy Conversion and Management. 2007, 48, 2286–2308.
40. Ryu, K. Effects of pilot injection timing on the combustion and emissions characteristics in a diesel engine using biodiesel–CNG dual fuel. Applied Energy. 2013, 111, 721–730.
41. Naber, J. D., Siebers, D. L., Di Julio, S. S., Westbrook, C. K. Effects of natural gas composition on ignition delay under diesel conditions. Combustion and Flame. 1994, 99, 192–200.
42. Liu, J., Yang, F., Wanga, H., Ouyang, M., Hao, S. Effects of pilot fuel quantity on the emissions characteristics of a CNG/diesel dual fuel engine with optimized pilot injection timing. Applied Energy. 2013, 110, 201–206.
43. Liu, S., Zhou, L., Wang, Z., Ren, J. Combustion characteristics of compressed natural gas/diesel dual-fuel turbocharged compressed ignition engine. Proceedings of the Institution of Mechanical Engineers, Part D: Journal of Automobile Engineering. 2003, 217–833.
44. Shah, A., Thipse, S. S., Tyagi, A., Rairikar, S. D., Kavthekar, K. P. Literature review and simulation of dual fuel diesel-CNG engines. SAE Paper 2011-26-0001.
45. Sahoo, B. B., Sahoo, N., Saha, U. K. Effect of engine parameters and type of gaseous fuel on the performance of dual-fuel gas diesel engines – a critical review. Renew. Sust. Energy Rev. 2009, 13, 1151–1184.
46. Chatlatanagulchai, W., Yaovaja, K., Rhienprayoon, S., Wannatong, K. Air–fuel ratio regulation with optimum throttle opening in diesel-dual-fuel engine. SAE paper 2010-01-1574, 2010.

47. Chatlatanagulchai, W., Rhienprayoon, S., Yaovaja, K., Wannatong, K. Air/Fuel ratio control in diesel-dual-fuel engine by varying throttle, EGR valve, and total fuel. SAE paper 2010-01-2200, 2010.
48. Tomita, E., Harada, Y., Kawahara, N., Sakane, A. Effect of EGR on combustion and exhaust emissions in supercharged dual-fuel natural gas engine ignited with diesel fuel. SAE paper 2009-01-1832, 2009.
49. Singh, S., Liang, L., Reitz, R. D., Int. J. of Engine Research, 2006, 7(1), 65-75.
50. Dec, J.E. SAE Paper 970873, 1997.
51. Som, S., Aggarwal, S.K., Combustion and Flame. 2010, 157, 1179–1193.
52. Lutz, A. E., Kee, R. J., Grcar, J. F., Rupley, F. M. OPPDIF: a FORTRAN program for computing opposed flow diffusion flames. Technical Report SAND 96-8243, UC-1404, 1997.
53. Berta, P. Numerical and experimental investigation of n-heptane combustion in a counterflow configuration. Ph.D. Thesis, University of Illinois at Chicago, USA, 2005.
54. Senecal, P. K., Pomraning, E., Richards, K. J. Multi-dimensional modeling of direct injection diesel spray liquid length and flame lift-off length using CFD and parallel detailed chemistry. SAE Paper No. 2003-01-0243.
55. Senecal, P. K., Richards, K. J., Pomraning, E., Yang, T., Dai, M. Z., McDavid, R. M., Patterson, M. A., Hou, S., Sethaji, T. A new parallel cut-cell Cartesian CFD code for rapid grid generation applied to in-cylinder diesel engine simulations. SAE Paper No.2007-01-0159.
56. S. K. Aggarwal and D. E. Longman. A Computational Study on the Effects of Pre-Ignition Processes on Diesel Engine Combustion and Emissions. ASME/JSME 2011. Paper No. AJTEC2011-44202, pp. T20083-T20083-11
57. Liu, A.B., Mather, D.K., and Reitz, R.D. Modeling the effects of drop drag and breakup on Fuel sprays. SAE Paper No. 930072, 1993.
58. Liu, A. B., Mather, D. K., Reitz, R. D. Modeling the effects of drop drag and breakup on fuel sprays. SAE Paper 1993-93007.
59. Patterson, M.A., Reitz, R. D. Modeling the effects of fuel spray characteristics on diesel engine combustion and emission. SAE Technical Paper 1998-98-0131.
60. Reitz, R. D., Bracco, F. V. Mechanisms of Breakup of Round Liquid Jets. Encyclopedia of Fluid Mechanics, Gulf Pub., Houston, TX, p. 233, 1986.
61. Schmidt, D. P., Rutland, C. J. A new droplet collision algorithm. J. of Computational Physics 2000, 164, 62–80.
62. Poster, S. L., Abraham, J. Modeling collision and coalescence in diesel spray. Int. J. Multiphase Flow. 2002, 28, 997–1019.
63. Som Sibendu. Development and validation of spray models for investigating diesel engine combustion and emissions. Thesis University of Illinois at Chicago 2009.
64. Chiang, C. H., Raju, M. S., Sirignano, W. A. Numerical analysis of a convecting, vaporizing fuel droplet with variable properties, Int. J. Heat Mass Transfer. 1992, 35, 1307.
65. Senecal, P., Pomraning, E., Richards, K., Briggs, T. et al., "Multi-Dimensional Modeling of Direct-Injection Diesel Spray Liquid Length and Flame Lift-off Length using CFD and Parallel Detailed Chemistry," SAE Technical Paper 2003-01-1043, 2003, doi:10.4271/2003-01-1043.
66. Kee, R. J, Rupley, F. M, Miller, J. A, "Chemkin-II: A Fortran Chemical Kinetics Package for the Analysis of Gas Phase Chemical Kinetics," 1989.
67. Pomraning E, Richards K, Senecal P. Modeling turbulent combustion using a RANS model, detailed chemistry, and adaptive mesh refinement. SAE Technical Paper 2014-01-1116.
68. Pomraning E, Richards K, Senecal P. Modeling turbulent combustion using a RANS model, detailed chemistry, and adaptive mesh refinement. SAE Technical Paper 2014-01-1116.
69. Raju, M., Wang, M., Dai, M., Piggott, W. et al., "Acceleration of Detailed Chemical Kinetics Using Multi-zone Modeling for CFD in Internal Combustion Engine Simulations," SAE Technical Paper 2012-01-0135, 2012, doi:10.4271/2012-01-0135.

70. Richards, K. J., Senecal, P. K., Pomraning, E. CONVERGE (Version 2.1.0), Convergent Science, Inc., Middleton, WI. 2013.
71. Ranzi, E., Dente, M., Goldaniga, A., Bozzano, G., Faravelli, T. Prog. Energy Combust. Sci. 2001 27, 99.
72. Goldaniga, Faravelli, T., Ranzi, E. Combust. Flame 2000122, 350–358.
73. Zeldovich, J. Acta Physicochimica, U.R.S.S. 21:577–628, 1946.
74. Glarborg, P., Jensen, A. D., Johnsson, J. E. Progress in Energy and Combustion Science 29:89–113, 2003.
75. Malte, P., Pratt, D. T. Proceedings of the Combustion Institute 15:1061–1070, 1974.
76. Guo, H., Smallwood, G. J. Combustion Theory and Modeling, 2007, 11, 5, pp. 741–753.
77. Guo, H., Smallwood, G. J. Int. J. Thermal Sciences 2007, 46, 936–943.
78. Shimizu, T., Williams, F. A., Frassoldati, A. 43rd AIAA Aerospace Sciences Meeting and Exhibit AIAA-2005-0144 (2005).
79. Frassoldati, A., Ranzi, E., Faravelli, T. XXVIII Event of Italian Section of Combustion Institute IV-6, 2005.
80. Johnsson J., Olofsson N. , Bladh H., Bengtsson P. Lund University. http://www.forbrf.lth.se/english/research/measurement_methods/laser_induced_incandescence_lii/ (accessed Jan 24, 2013).
81. Smoluchowski M.V., Phys Z. Chem. 1917, 92: 129–139.
82. Appel, J., Bockhorn, H., Frenklach, M. Combust. Flame. 2000, 121, 122–136.
83. Frenklach M. and Harris S. J. J. of Colloid and Interface Sci. 1987, 118: 252–261.
84. Appel, J.; Bockhorn, H.; Frenklach, M. Combust. Flame 2000, 121, 122−136.
85. Smoluchowski, M. V., Z. Phys. Chem. 92:129 (1917).
86. H. El-Asrag, T. Lu, C.K. Law, S. Menon. Simulation of soot formation in turbulent premixed flames. Combustion and Flame, Volume 150, Issues 1–2, July 2007, Pages 108–126.
87. Frenklach, M.; Harris, S. J. J. Colloid Interface Sci. 1987, 118, 252−261.
88. E. Ranzi, A. Frassoldati, R. Grana, A. Cuoci, T. Faravelli, A.P. Kelley, C.K. Law, Hierarchical and comparative kinetic modeling of laminar flame speeds of hydrocarbon and oxygenated fuels, Progress in Energy and Combustion Science, 38 (4), pp. 468-501 (2012), DOI: 10.1016/j.pecs.2012.03.004
89. A. Cuoci, A. Frassoldati, T. Faravelli, E. Ranzi, Formation of soot and nitrogen oxides in unsteady counterflow diffusion flames, Combustion and Flame 156 (10), pp. 2010-2022 (2009), doi:10.1016/j.combustflame.2009.06.023
90. A. Frassoldati, T. Faravelli and E. Ranzi, Kinetic modeling of the interactions between NO and hydrocarbons at high temperature, Combustion and Flame 135, pp. 97-112 (2003), doi:10.1016/S0010-2180(03)00152-4
91. T. Faravelli, A.Frassoldati and E. Ranzi, Kinetic modeling of the interactions between NO and hydrocarbons in the oxidation of hydrocarbons at low temperatures, Combustion and Flame, 132(1-2), pp. 188 - 207 (2003), doi:10.1016/S0010-2180(02)00437-6
92. http://creckmodeling.chem.polimi.it/index.php/current-version-kinetic-mechanisms/low-and-high-temperature-complete-mechanism. Accessed on July 2014.
93. Lu, T. F., and Law, C. K., A Directed Relation Graph Method for Mechanism Reduction, Proceedings of the Combustion Institute, 30(1), 2005, pp. 1333-1341.
94. Gauthier BM, Davidson DF, Hanson RK. Shock tube determination of ignition delay times in full-blend and surrogate fuel mixtures. Combust. Flame. 2004; 139: 300–311.
95. http://www.tfd.chalmers.se/~valeri/MECH.html.
96. Tao F, Reitz RD, Foster DE. Revisit of diesel reference fuel (n-heptane) mechanism applied to multidimensional diesel ignition and combustion simulations. Proceedings of International Multidimensional Engine Modeling User's Group Meeting, Detroit, MI, April 15, 2007.

97. E. Ranzi, A. Frassoldati, R. Grana, A. Cuoci, T. Faravelli, A.P. Kelley, C.K. Law, Hierarchical and comparative kinetic modeling of laminar flame speeds of hydrocarbon and oxygenated fuels, Progress in Energy and Combustion Science, 38 (4), pp. 468-501 (2012), DOI: 10.1016/j.pecs.2012.03.004
98. http://creckmodeling.chem.polimi.it/index.php/current-version-kinetic-mechanisms/low-and-high-temperature-complete-mechanism. Accessed on July 2014.
99. Curran HJ, Gaffuri P, Pitz W J, Westbrook C K. A comprehensive modeling study of n-heptane oxidation. Combust. Flame 1998; 114: 149–177.
100. Garner S, Brezinsky K. Biologically derived diesel fuel and NO formation: An experimental and chemical kinetic study, Part 1. Combust. Flame. 2011; 158: 2289–2301.
101. http://www.tfd.chalmers.se/~valeri/MECH.html.
102. Tao, F., Reitz, R. D., Foster, D. E. Revisit of Diesel Reference Fuel (n-Heptane) Mechanism Applied to Multidimensional Diesel Ignition and Combustion Simulations. Seventeenth International Multidimensional Engine Modeling User's Group Meeting at the SAE Congress, April 15, 2007, Detroit, Michigan.
103. Lu TF, Law CK, A criterion based on computational singular perturbation for the identification of quasi steady state species: A reduced mechanism for methane oxidation with NO chemistry. Combustion and Flame, Vol.154 No.4 pp.761–774, 2008.
104. Metcalfe WK, Burke SM, Ahmed SS, Curran HJ. A Hierarchical and Comparative Kinetic Modeling Study of C1−C2 Hydrocarbon and Oxygenated Fuels. International Journal of Chemical Kinetics. Volume 45, Issue 10, pages 638–675, October 2013
105. Gregory P. Smith, David M. Golden, Michael Frenklach, Nigel W. Moriarty, Boris Eiteneer, Mikhail Goldenberg, C. Thomas Bowman, Ronald K. Hanson, Soonho Song, William C. Gardiner, Jr., Vitali V. Lissianski, and Zhiwei Qin http://www.me.berkeley.edu/gri_mech/
106. Huang J, Bushe WK, Hill PG, Munshi SR. Experimental and kinetic study of shock initiated ignition in homogeneous methane–hydrogen–air mixtures at engine-relevant conditions. Int J Chem Kinet 2006;38:221–33.
107. Hwang, J. Y., Chung, S. H. Combust. Flame. 2001, 125, 752–62.
108. Vandsburger U., Kennedy I., Glassman I. Combustion Science and Technology. 1984, 39: 263–85.
109. Liu F., Guo H., Smallwood G., Hafi M. Journal of Quantitative Spectroscopy & Radiative Transfer. 2004, 84: 501–511.
110. Germano, M., Piomelli, U., Moin, P., Cabot, W. (1991). "A dynamic subgrid-scale eddy viscosity model". Physics of Fluids A 3 (7): 1760–1765.
111. Som, S, D'Errico, G, Longman, D, and Lucchini, T. Comparison and standardization of numerical approaches for the prediction of non-reacting and reacting diesel sprays. SAE Technical Paper 2012-01-1263.
112. Xue Q, Som S, Senecal P K, Pomraning E. Large eddy simulation of fuel-spray under non-reacting ic engine conditions. Atomization and Sprays, 2013; 23: 925–955.
113. Hiroyasu, H. and Kadota, T., “Models for Combustion and Formation of Nitric Oxide and Soot in DI Diesel Engines,” SAE Paper No. 760129, 1976.
114. Siebers D.L., Higgins B. (2001) "Flame lift-off on direct-injection diesel sprays under quiescent conditions." SAE Paper 2001-01-0530.
115. Higgins B., Siebers D.L. (2001) "Measurement of the flame lift-off location on DI diesel sprays using OH chemiluminescence." SAE Paper 2001-01-0918.
116. Higgins B., Siebers D.L. (2000) "Diesel-spray ignition and premixed burn behavior." SAE Paper 2000-01-0940.
117. Siebers DL, Higgins B. Flame lift-off on direct-injection diesel sprays under quiescent conditions. SAE Paper 2001-01-0530.
118. Higgins B, Siebers DL. Measurement of the flame lift-off location on DI diesel sprays using OH chemiluminescence. SAE Paper 2001-01-0918.

119. Fu X, Aggarwal S K. Two-stage ignition and NTC phenomenon in diesel engines. Fuel, 2015; 144: 188–196.
120. Ciatti, S., Subramanian, S. N. An Experimental Investigation of Low-Octane Gasoline in Diesel Engines. J. of Engineering for Gas Turbines and Power. 2011, 133, 092802-1/11.
121. Garner, S. Biologically Derived Diesel Fuel and NOx Formation: An Experimental and Kinetic Modeling Study of Saturated and Unsaturated C8 Fatty Acid Methyl Esters. PhD Thesis, University of Illinois at Chicago, 2011.
122. Garner, S., Brezinsky, K. Combust. Flame. DOI: 10.1016/j. 2011.04.014,.
123. Miller, J. A., Bowman, C. T. Prog. Energy Combust. Sci. 1989, 15: 287.
124. Turanyi, T. Kinalc (http://www.chem.leeds.ac.uk/Combustion/kinalc.html).
125. Xue, H., Aggarwal, S. K. Combust. and Flame, 2003, 132, 723–741.
126. Naha, S.; Aggarwal, S.K. Fuel effects on NOx emissions in partially premixed flames. Combust. Flame 139 2004 90 - 105
127. Han, X.; Aggarwal, S. K.; Brezinsky, K. Energy Fuels. 2012, 26, 879-888.
128. Miller, J.A.; Melius, C.F. Combust. Flame 1992, 91, 21-39.
129. Zhang, R.H.; Eddings, E.G.; Sarofim. A.F. Energy Fuels 2008, 22 (2), 945-953.
130. Zhang, R.H.; Eddings, E.G.; Sarofim. A.F. Energy Fuels 2007, 21 (2), 677-685.
131. Fu X, Han X, Brezinsky K, Aggarwal S. Effect of fuel molecular structure and premixing on soot emissions from n-heptane and 1-heptene flames. Energy Fuels, 2013; 27: 6262–6272.
132. Curran, H. J., Pitz, W. J., Westbrook, C. K., Callahan, C. V., Dryer, F. L. Proc. Combust. Inst. 1998, 27, 379–387.
133. Schnaubelt, S., Moriue, O., Coordes, T., Eigenbrod, C., Rath, H. J. Proc. Combust. Inst. 2000, 28, 953–960.
134. Cuoci, A., Mehl, M., Buzzi-Ferraris, G., Faravelli, T., Manca, D., Ranzi, E. Combust. Flame. 2005, 143, 211–226.
135. Boehman, A. L., Corre, O. L. Combust. Sci. and Tech. 2008, 180, 1193–1206.
136. Azzoni, R., Ratti, S., Aggarwal, S. K., Puri, I. K. The Structure of Triple Flames Stabilized on a Slot Burner, Combustion and Flame. 1999, 119, 23–40.
137. Aggarwal, S. K. Extinction of Laminar Partially Premixed Flames, Progress in Energy & Combustion Science, 2009, 35, 528–570.

9 APPENDIX

Appendix A. Governing Equations for RANS turbulence model

Turbulent reacting flow can be described by conservation equations for the mixture mass, momentum, energy, and mass of individual species. They can be written in 3-D form for a Newtonian fluid:

Continuity:

$$\frac{\partial \rho}{\partial t} + \frac{\partial \rho u_i}{\partial x_i} = \dot{\rho}_s \tag{89}$$

Species:

$$\frac{\partial \rho Y_m}{\partial t} + \frac{\partial \rho u_i Y_m}{\partial x_i} = \frac{\partial}{\partial x_i}\left(\rho D_m \frac{\partial Y_m}{\partial x_i} \right) + \dot{\rho}_{m,s} + \dot{\rho}_{m,ch} \tag{90}$$

Momentum:

$$\frac{\partial \rho u_i}{\partial t} + \frac{\partial \rho u_i u_j}{\partial x_i} = -\frac{\partial p}{\partial x_i} + \frac{\partial \sigma_{ij}}{\partial x_i} + \rho g + F_s \tag{91}$$

Energy:

$$\frac{\partial \rho e}{\partial t} + \frac{\partial \rho u_i e}{\partial x_i} = -p\frac{\partial u_i}{\partial x_i} + \sigma_{ij}\frac{\partial u_i}{\partial x_j} + \frac{\partial}{\partial x_i}\left(K \frac{\partial T}{\partial x_i} \right) + \frac{\partial}{\partial x_i}\left(\rho D \sum_m h_m \frac{\partial Y_m}{\partial x_i} \right) + \dot{Q}_{ch} + \dot{Q}_s \tag{92}$$

Equation (89) represents the conservation of mixture. Here ρ is mixture density. u is the instantaneous velocity, and $\dot{\rho}_s$ represents the source term due to droplet evaporation. In Eq. (90), Y_m is the mass fraction of species m, and D is the mass diffusion coefficient. The first term on the

right hand side is the diffusive flux, and $\dot{\rho}_{m,s}$ and $\dot{\rho}_{m,ch}$ represent source terms due to droplet evaporation and chemical reactions, respectively. In Eq. (91), σ is the viscous stress tensor:

$$\sigma_{ij} = \mu\left[2S_{ij} - \frac{2}{3}\delta_{ij}\frac{\partial u_i}{\partial x_i}\right] \tag{93}$$

$$S_{ij} = \frac{1}{2}\left(\frac{\partial u_i}{\partial x_j} + \frac{\partial u_j}{\partial u_i}\right) \tag{94}$$

S is the strain rate tensor, and μ is the dynamic viscosity. Here δ is the tensorial Kronecker symbol δ_{ij} ($\delta_{ij} = 1$ for $i = j$ and $\delta_{ij} = 0$ for $i \neq j$). The terms on the left-hand side of the Eq. (91) represent the local rate of change and convection of momentum, respectively, while the terms on the right-hand side represent, respectively, the pressure force, viscous force (molecular transport of momentum), and the forces due to gravity. F_s respresents the source term due to the force applied to the gas phase through droplet drag and momentum exchange due to evaporation. Finally, in Eq. (92), e is specific internal energy, K is thermal conductivity. D is diffusivity, h_m is the species enthalpy of species m, and $\dot{Q}_{ch}$ and $\dot{Q}_s$ represent source terms due to chemical reactions and droplet evaporation respectively.

For RANS models. the flow variables (e.g., velocity) are decomposed into an ensemble mean and a fluctuating term as follows:

$$u_i = \overline{u}_i + u_i' \tag{95}$$

where u_i is the instantaneous velocity, $\overline{u}_i$ the ensemble mean velocity, and u_i' the fluctuating term. In turbulent flows the pdf of any stochastic variable depends, in principle, on the position x and on time t. These functional dependence is expressed as:

$$P\left(u;x,t\right) \tag{96}$$

The semicolon here indicates that P is a probability density and is a function of x and t. Note that in stationary turbulent flows it does not depend on t, while in homogeneous turbulent fields it does not depend on x. Then the ensemble mean of u or the expectation of u can be expressed as

$$\overline{u}\left(x,t\right)=\int_{-\infty}^{+\infty}uP\left(u;x,t\right)du \tag{97}$$

For flows with large density changes as occur in combustion, it is often convenient to introduce a density-weighted average $\tilde{u}$, called Favre average, by splitting u into:

$$u=\tilde{u}+u'' \tag{98}$$

This averaging procedure is defined by requiring that the average of the product of u'' with the density ρ vanishes:

$$\overline{\rho u''}=0 \tag{99}$$

The definition for $\tilde{u}$ can be derived by multiplying Eq. (98) by the density and averaging:

$$\overline{\rho u}=\overline{\rho\tilde{u}}+\overline{\rho u''}=\overline{\rho}\tilde{u} \tag{100}$$

Here the average of the product $\rho\tilde{u}$ is equal to the product of the averages $\overline{\rho}$ and $\tilde{u}$, since $\tilde{u}$ is already an average defined by

$$\tilde{u}=\frac{\int_T\rho u dt}{\int_T\rho dt}=\frac{\overline{\rho u}}{\overline{\rho}} \tag{101}$$

Using Favre averaging on Eq. (89), the continuity equation becomes:

$$\frac{\partial \overline{\rho}}{\partial t} + \frac{\partial \overline{\rho} \widetilde{u}_i}{\partial x_i} = \dot{\rho}_s \tag{102}$$

According to the following derivation:

$$\overline{\rho u_i u_j} = \overline{\rho}\overline{u}_i\overline{u}_j + \overline{\rho}\overline{u_i' u_j'} + \overline{\rho' u_i'}\overline{u}_j + \overline{\rho' u_j'}\overline{u}_i + \overline{\rho' u_i' u_j'}$$

$$\begin{aligned} \rho u_i u_j &= \rho\left(\tilde{u}_i + u_i''\right)\left(\tilde{u}_j + u_j''\right) \\ &= \rho\tilde{u}_i\tilde{u}_j + \rho u_i''\tilde{u}_j + \rho\tilde{u}_i u_j'' + \rho u_i'' u_j'' \end{aligned} \tag{103}$$

$$\overline{\rho u_i u_j} = \overline{\rho}\tilde{u}_i\tilde{u}_j + \overline{\rho}\widetilde{u_i'' u_j''}$$

Using Eqs. (101) and (103) in Eq. (90), the momentum equation becomes:

$$\frac{\partial \overline{\rho}\tilde{u}_i}{\partial t} + \frac{\partial}{\partial x_j}\left(\overline{\rho}\tilde{u}_i\tilde{u}_j\right) = -\frac{\partial \overline{p}}{\partial x_i} + \frac{\partial}{\partial x_j}\left[\overline{\sigma}_{ji} - \overline{\rho}\widetilde{u_i'' u_j''}\right] + F_s + \overline{\rho}g \tag{104}$$

The stress tensor can be derived as:

$$\overline{\sigma}_{ij} = \mu\left(\frac{\partial \tilde{u}_i}{\partial x_j} + \frac{\partial \tilde{u}_j}{\partial x_i}\right) - \frac{2}{3}\delta_{ij}\mu\frac{\partial \tilde{u}_k}{\partial x_k} \tag{105}$$

Similarly, the species equation (Eq. (90)) can be derived as

$$\frac{\partial \overline{\rho}\tilde{Y}_m}{\partial t} + \frac{\partial \overline{\rho}\tilde{Y}_m\tilde{u}_j}{\partial x_j} = \frac{\partial}{\partial x_j}\left(\overline{\rho}D_m\frac{\partial \tilde{Y}_m}{\partial x_j} - \overline{\rho}\widetilde{Y_m'' u_j''}\right) + \dot{\overline{\rho}}_{m,s} + \dot{\overline{\rho}}_{m,ch} \tag{106}$$

And the energy equation (Eq. (92)) can be derived as

$$\frac{\partial \bar{\rho}\tilde{e}}{\partial t}+\frac{\partial \bar{\rho}\tilde{e}\tilde{u}_i}{\partial x_i}=-\bar{p}\frac{\partial \tilde{u}_i}{\partial x_i}+\tilde{\sigma}_{ij}\frac{\partial \tilde{u}_i}{\partial x_i}+\frac{\partial}{\partial x_i}\left(K\frac{\partial \tilde{T}}{\partial x_i}-\bar{\rho}\widetilde{e''u_i''}\right)+ \frac{\partial}{\partial x_i}\left(\bar{\rho}D\sum_m \bar{h}_m\frac{\partial \tilde{Y}_m}{\partial x_i}-\sum_m \bar{h}_m\bar{\rho}\widetilde{Y_m''u_i''}\right)+\bar{\dot{Q}}_{ch}+\dot{Q}_S \tag{107}$$

The correlation of $-\bar{\rho}\widetilde{u_i''u_j''}$ is defined as the Reynolds stress tensor, and introduces the first closure problem in turbulent modeling. Using a Reynolds stress model, it is possible to derive equations for the six components of this stress tensor. However, several terms in these equations are unclosed, and therefore, approaches based on Reynolds stress models are not yet widely used in turbulent combustion. Many industrial codes still rely on the k–ε model, which, by using an eddy viscosity, introduces the assumption of isotropy. It is known that turbulence becomes isotropic at the small scales, but this does not necessarily apply to the large scales at which the averaged quantities are defined. The k–ε model is based on equations where the turbulent transport is diffusive and therefore is more easily handled by numerical methods than the Reynolds stress equations. This is probably the main reason for its wide use in many commercial codes.

Using the Boussinesq approximation, the effect of turbulence on momentum transport in the momentum equation can be represented as an increased viscosity known as the turbulent eddy viscosity:

$$\mu_t=C_\mu\bar{\rho}\frac{k^2}{\varepsilon} \tag{108}$$

The turbulent dynamic eddy viscosity is related to the turbulent kinematic eddy viscosity:

$$\mu_t=\bar{\rho}\nu_t \tag{109}$$

The turbulent kinetic energy k is defined as

$$k = \frac{1}{2}\widetilde{u_j'' u_i''} \tag{110}$$

An important simplification is obtained using the eddy viscosity, which leads to the following expression of the Reynolds stress term:

$$-\bar{\rho}\widetilde{u_i'' u_j''} = \bar{\rho}\nu_t\left[2\tilde{S}_{ij} - \frac{2}{3}\delta_{ij}\frac{\partial \tilde{u}_i}{\partial x_i}\right] - \frac{2}{3}\delta_{ij}\bar{\rho}k \tag{111}$$

Similarly, for the $-\bar{\rho}\widetilde{y_m'' u_i''}$ and $-\bar{\rho}\widetilde{e'' u_i''}$ terms, the turbulent diffusivity and turbulent conductivity can be defined to account for the enhanced species transport and energy transport due to turbulence.

$$D_m = \frac{\nu}{Sc} \tag{112}$$

Sc is the Schmidt number.

In this study, the diffusivity for each species are set to be equal to the diffusivity of air.

$$-\rho\widetilde{Y_m'' u_i''} = \bar{\rho}D_{m,t}\frac{\partial \tilde{Y}_m}{\partial x_i} \tag{113}$$

where

$$D_{m,t} = \frac{\nu_t}{Sc_t} \tag{114}$$

and Sc_t is the turbulent Schmidt number.

Note that the turbulent heat flux is estimated as:

$$-\bar{\rho}\widetilde{e''u_i''} = K_t \frac{\partial \tilde{T}}{\partial x_i} \tag{115}$$

where the turbulent eddy conductivity is

$$K_t = c_p \frac{\mu_t}{\mathrm{Pr}_t} \tag{116}$$

For the standard k-ε and the RNG k-ε models, additional transport equations are needed for both k and ε, and thus obtain the turbulent viscosity given by Eq. (108). The RNG model was developed using Re-Normalisation Group (RNG) methods to renormalise the Navier-Stokes equations, to account for the effects of smaller scales of motion. In the standard k-ε model the eddy viscosity is determined from a single turbulence length scale, so the calculated turbulent diffusion is that which occurs only at the specified scale, whereas in reality all scales of motion will contribute to the turbulent diffusion. The RNG approach, which is a mathematical technique that can be used to derive a turbulence model similar to the k-ε, results in a modified form of the ε equation which attempts to account for the different scales of motion through changes to the production term. For the turbulent kinetic energy k, the equation is

$$\frac{\partial \bar{\rho} k}{\partial t} + \frac{\partial \bar{\rho} \tilde{u}_i k}{\partial x_i} = \bar{\sigma}_{ij} \frac{\partial \tilde{u}_i}{\partial x_j} + \frac{\partial}{\partial x_j}\left(\frac{\mu_t}{\mathrm{Pr}_t}\frac{\partial k}{\partial x_j}\right) - \bar{\rho}\varepsilon + \dot{W}_s \tag{117}$$

On the left-hand side, the two terms represent the local rate of change and convection of k, respectively. On the right-hand side, the first three terms represent the production, diffusive transport, and dissipation of turbulent energy, respectively, and $\dot{W}_s$ represents the source term due to interaction of turbulence with spray droplets.

Transport equation for turbulent dissipation rate is:

$$\frac{\partial \bar{\rho}\varepsilon}{\partial t}+\frac{\partial \bar{\rho}\varepsilon\tilde{u}_i}{\partial x_i}=\frac{\partial}{\partial x_j}\left(\frac{\mu_t}{\mathrm{Pr}_\varepsilon}\frac{\partial \varepsilon}{\partial x_j}\right)-C_{\varepsilon 3}\bar{\rho}\varepsilon\frac{\partial \tilde{u}_i}{\partial x_i}+\left(C_{\varepsilon 1}\frac{\partial \tilde{u}_i}{\partial x_j}\bar{\sigma}_{ij}-C_{\varepsilon 2}\bar{\rho}\varepsilon+C_S S_S\right)\frac{\varepsilon}{k}-\rho R \tag{118}$$

Similar to the turbulent kinetic energy, the two terms on the left-hand side represent the local rate of change and convection of ε, respectively. Similarly, the first three terms on the right-hand side represent the diffusive transport, dissipation, and production of ε. The source term S_S is included to account for the interactions of turbulence with the discrete phase. This term is calculated as

$$S_S=-\frac{\sum_P N_P\left(F'_{drag,i}u'_i\right)_P}{V} \tag{119}$$

where the summation is over all parcels in the cell. N_P is the number of the drops in a parcel. V is the cell volume. And

$$F'_{drag,i}=\frac{F_{drag,i}}{\left(\bar{u}_i+u'_i-v_i\right)}u'_i \tag{120}$$

where $F_{drag,i}$ is the drag force on a droplet in cell i. $\bar{u}_i$ is the mean component of the gas phase velocity. u'_i is the fluctuating component of the gas-phase velocity. v_i is the droplet velocity in cell i. There is special treatments for u'_i as described in the Converge Theory Manual.

The R is defined based on three types of the k-ε models. For the standard k-ε model, R=0. For the RNG k-ε model,

$$R=\frac{C_\mu\eta^3\left(1-\eta/\eta_0\right)}{\left(1+\beta\eta^3\right)}\frac{\varepsilon^2}{k} \tag{121}$$

where

$$\eta = \frac{k}{\varepsilon}\left|S_{ij}\right| = \frac{k}{\varepsilon}\sqrt{2S_{ij}S_{ij}} \tag{122}$$

The mean strain rate tensor derived from Eq. (94)

$$S_{ij} = \frac{1}{2}\left(\frac{\partial \tilde{u}_i}{\partial x_j} + \frac{\partial \tilde{u}_j}{\partial x_i}\right) \tag{123}$$

And the Rapid Distortion RNG k-ε model uses the transport equation for ε given by

$$\begin{aligned}\frac{\partial \bar{\rho}\varepsilon}{\partial t} + \frac{\partial \bar{\rho}\tilde{u}_i\varepsilon}{\partial x_i} = \frac{\partial}{\partial x_j}\left(\frac{\mu}{\mathrm{Pr}_\varepsilon}\frac{\partial \varepsilon}{\partial x_j}\right) - \left[\frac{2}{3}C_{\varepsilon 1} - C_{\varepsilon 3} + \frac{2}{3}C_\mu C_\eta \frac{k}{\varepsilon}\frac{\partial \tilde{u}_k}{\partial x_k}\right]\bar{\rho}\varepsilon\frac{\partial \tilde{u}_i}{\partial x_i} \\ \left(\left(C_{\varepsilon 1} - C_\eta\right)\frac{\partial \tilde{u}_i}{\partial x_j}\sigma^*_{ij} - C_{\varepsilon 2}\bar{\rho}\varepsilon + C_S S_S\right)\frac{\varepsilon}{k}\end{aligned} \tag{124}$$

where

$$C_\eta = \frac{\eta\left(1-\eta/\eta_0\right)}{1+\beta\eta^3} \tag{125}$$

$$\sigma^*_{ij} = \bar{\sigma}_{ij} - \frac{1}{3}\delta_{ij}\bar{\sigma}_{kk} = 2\mu_t\left(S_{ij} - \frac{1}{3}\delta_{ij}\frac{\partial \tilde{u}_k}{\partial x_k}\right) \tag{126}$$

The Rapid Distortion RNG k-ε model is used in this work since it is modified based on the RNG k-ε model through an isotropic rapid distortion analysis to account for the flow compressibility in variable-density engine flows.

The pressure is obtained from the Redlich-Kwong cubic equation of state:

$$p = Z\rho RT / MW \tag{127}$$

where R is the universal gas constant, Z is the compressibility factor, MW is the molecular weight, Z can be represented as

$$Z = \frac{1}{1-h} - \frac{A^2}{B}\frac{h}{1+h} \tag{128}$$

where

$$\begin{aligned} A^2 &= \frac{a}{R^2 T^{2.5}} = \frac{0.4278 T_c^{2.5}}{p_c T^{2.5}} \\ B &= \frac{b}{RT} = \frac{0.0867 T_c}{p_c T} \\ h &= \frac{Bp}{Z} = \frac{b}{v} \end{aligned} \tag{129}$$

where v is the molar volume $v = V/n$, T_c is the critical temperature, p_c is the critical pressure.

For the source terms, $\dot{\rho}_s$, $\dot{\rho}_{m,s}$, F_s, $\dot{Q}_s$ and $\dot{W}_s$ are related to the spray model. Function of probable number of droplets per unit volume, droplet radius, temperature, velocity, droplet collision and break up. For momentum and energy, turbulence dispersion model is using O'Rourke model. And $\dot{\rho}_{m,ch}$ and $\dot{Q}_{ch}$ are related to the chemistry.

Appendix B. Turbulence – Chemistry Interaction Model

The turbulent chemistry interaction models can be identified as two classes, Topological Models and the reactor models. Topological models assume that the flame is a surface that can be tracked by the solver. The location of this surface may be associated with a resolution of a particular field (for instance, an iso-surface of a reaction progress variable in premixed combustion, or an iso-surface of the mixture fraction field in non-premixed equation). In terms of flame-turbulence interaction, they may cover the whole spectrum and treat the flame surface considering the laminar structure of this latter is conserved (this is the case for a flamelet model) or not (for instance, G-equation models with a turbulent flame speed containing correlations for flames at high Ka). There are two common models, Flamelet Model and Flame Surface Density Model.

The reactor model considers infinitely fast chemistry or finite rate chemistry. For premixed combustion, it includes Eddy Break-Up Model and Bray-Moss-Libby Model as turbulent flame speed models. For non-premixed combustion, it includes Conserved Scalar Equilibrium Model. For finite rate chemistry, the premixed combustion has Coherent flame model and Flamelets based on G-equation model. For non-premixed combustion, it includes Flamelets based on conserved scalar model. There are also two unsteady flamelets models namely Intrinsic Low Dimensional Manifolds method and Conditional Moment Closure method.

For LES turbulence model, Linear Eddy Model and PDF transport models are available. The PDF transport equation can be solved in two ways: through a Lagrangian approach using stochastic methods or in an Eulerian way using stochastic fields.

In Converge CFD code, the well-mixed approach is available and used in this work. The following description regarding this approach is adopted from SAE 2014-01-1116, 2014, by Eric Pomraning, Keith Richards, and P. K. Senecal.

Commonly, a RANS turbulence model is used to account for the enhanced mixing of turbulence in CFD simulations. These types of models typically account for the enhanced mixing of turbulence by introducing turbulent diffusion coefficients for momentum, species, and energy. The introduction of turbulent diffusion coefficients not only enhances mixing but it fundamentally changes the length scales in the flow simulation. The enhanced diffusion coefficients eliminate the smaller scales in the simulation leaving only larger scales. A significant advantage of a simulation using a RANS turbulence model is that coarser meshes than required by DNS can be used. The reason for this is that the smallest length scales in a RANS simulation are significantly larger than the smallest length scales in a DNS simulation. In a DNS simulation all length scales need to be resolved for the simulation to be accurate. In a similar manner to a DNS simulation, for a RANS simulation, all RANS length scales should also be resolved. Unfortunately, due to computational constraints, it is common for RANS simulations to be under-resolved. This under-resolution may create significant sub-grid terms that may have an impact on the simulation results.

The sub-grid effects resulting from insufficient resolution are shown to result in significant errors. In fact, the sub-grid terms are frequently significantly more important than the Turbulent Chemistry Interaction (TCI) effects. Unfortunately, many researchers incorrectly conflate the sub-grid effects with TCI effects. In many cases, due to insufficient resolution, a TCI model is erroneously used that is actually accounting for sub-grid effects. It is shown that if sufficient mesh resolution is used, accurate turbulent combustion results can be obtained directly using a RANS model, AMR, and detailed chemistry directly without the need for a TCI model.

Combustion is modeled directly using the SAGE detailed chemistry solver. The solver reads in CHEMKIN formatted chemical reaction mechanisms. At the beginning of each time-step, the chemical reactions are solved in each cell based on the temperature, pressure, and species mass fractions. Based on the reaction rates, the species mass fractions are then updated accordingly. In the present work, no additional models are included for the turbulent chemistry interaction (TCI). To reduce chemistry computational time, the multi-zone method is employed.

This type of modeling approach is often referred to as a "well mixed" model. The name would seem to imply that mixing is not accounted for in the model. This is incorrect. The mixing effects critical to accurately modeling combustion are accounted for via the solution of the RANS conservation equations for species, energy, and momentum. As will be shown, if the mesh resolution is under-resolved it would be correct to imply that mixing is not accounted for properly (i.e., sub-grid terms would need to be modeled for mixing) but for a well resolved RANS computational field the effects of mixing are accounted for in the RANS turbulence model.

It is well known that turbulence is critical in correctly predicting turbulent combustion. The role of turbulence is to enhance mixing via the small scales present in a highly turbulent field. The RNG k-epsilon model accounts for this enhanced mixing of turbulence by adding turbulent viscosity, turbulent conductivity, and turbulent species diffusion terms. The inclusion of turbulent diffusion coefficients fundamentally changes the flow field. In addition to enhancing mixing, the smaller length scales in the flow field are removed as a consequence of the larger turbulent diffusion coefficients.

In a turbulent flow, the small scales present wrinkle the momentum field which results in an increase of surface area of disparate momentum regions. This increase in surface area results in an increase in mixing via molecular diffusion. It is important to note that this increase in surface

area and the associated molecular diffusion is solely responsible for the increased mixing of momentum in a turbulent field. In order to accurately model this effect (without a turbulence model) all scales in the flow field would need to be resolved. The smallest scales in a flow field are the Kolmogorov scales which are given by

$$\eta = \left(\frac{\nu^3}{\varepsilon} \right)^{1/4} \tag{130}$$

For a typical engine simulation, the smallest scales are of order 10^{-6} to 10^{-5} meters. Thus, to simulate the enhanced mixing directly (i.e., DNS) would require a cell size of approximately 10^{-6} meters. Given the computational power of modern computers this is not practical for internal combustion engine simulations. If a simulation with DNS resolution could be run, no additional models would be required for turbulence or combustion. Thus, for practical mesh resolutions, a turbulence model is required to account for the enhanced mixing. The most common type of turbulence model used in engine simulations is a RANS turbulence model.

The role of the turbulent viscosity as described in Appendix A is to increase the mixing via diffusion in the larger scales present in a RANS simulation. It is important to note that the turbulent viscosity eliminates the smallest scales in the field. In fact, there are many unsteady RANS simulations that do not converge to the ensemble average flow. The consequence of this is that in many RANS simulations, the modeled ensemble average may not be accurate. In this case, the fluctuating term cannot be accurately derived from the turbulence model. With a turbulent viscosity, the smallest RANS scales can be approximated from

$$\eta_t = \left(\frac{\nu_t^3}{\varepsilon} \right)^{1/4} = C_\mu^{3/4} \frac{k^{3/2}}{\varepsilon} \tag{131}$$

The length scale shown in above equation is approximately the integral length scale. For a typical engine simulation with a RANS turbulence model, the smallest scales are now of order 10^{-4} to 10^{-3} meters. This implies that in order to resolve all scales in a RANS engine simulation, the mesh resolution should be of order 10^{-4} to 10^{-3} meters. It is interesting to note that for a RANS simulation increasing resolution beyond approximately 10^{-4} meters will not improve the accuracy as there are no more scales to resolve. It is also interesting to note that most current engine simulations are run with mesh resolutions of approximately 10^{-3} meters and larger. Evidently, these simulations are likely under-resolved even in the context of a RANS simulation.

Using concepts from Large Eddy Simulations (LES), the RANS ensemble average can be decomposed into a resolved and sub-grid as

$$\tilde{u}_i = \hat{\tilde{u}}_i + \tilde{u}_i'' \tag{132}$$

where $\hat{\tilde{u}}_i$ is the resolved field and $\tilde{u}_i''$ is the sub-grid field. It is important to note that the RANS field sub-grid velocity $\tilde{u}_i$" is not related to the RANS fluctuating velocity (u_i'). In a well resolved simulation, the RANS sub-grid velocity is small but the fluctuating velocity is not small. Conversely, for a simulation with a relatively coarse mesh the sub-grid velocity is not small and it may be larger than the fluctuating velocity. Applying the decomposition gives the following resolved RANS field momentum equation:

$$\frac{\partial \hat{\bar{\rho}} \hat{\tilde{u}}_i}{\partial t} + \frac{\partial \hat{\bar{\rho}} \hat{\tilde{u}}_i \hat{\tilde{u}}_j}{\partial x_j} = -\frac{\partial \tilde{p}}{\partial x_i} + \frac{\partial \hat{\bar{\sigma}}_{t,ij}}{\partial x_j} - \frac{\partial \tau_{ij}}{\partial x_j} \tag{133}$$

where

$$\tau_{ij} = \bar{\bar{\rho}}\left(\widetilde{\tilde{u}_i \tilde{u}_j} - \tilde{\bar{u}}_i \tilde{\bar{u}}_j\right) \tag{134}$$

Equation above is the RANS sub-grid stress tensor. Again, for a well resolved RANS field this term goes to zero. However, for simulations with a coarse mesh, the RANS sub-grid stress tensor is not zero and it may be significant (possibly more significant than the unclosed stress tensor. Most coarse RANS simulations (typical of engine simulations) do not account for this term directly.

Similar approaches can be applied to turbulent energy transport and turbulent species transport. As is the case with momentum, the small scales present in a turbulent field act to wrinkle the energy (temperature) field. This wrinkling increases the surface area of disparate temperature regions. The increase in surface area results in an increase in mixing via molecular conductivity. It is important to note that this increase in surface area and the associated molecular conductivity is solely responsible for the increased mixing of energy in a turbulent flow.

The RANS energy field can be decomposed into a resolved and sub-grid field given by

$$\tilde{e} = \tilde{\bar{e}} + \tilde{e}'' \tag{135}$$

where $\tilde{\bar{e}}$ is the resolved energy RANS field and $\tilde{e}''$ is the sub-grid energy RANS field. Apply this decomposition to turbulent energy transport equation, gives

$$\frac{\partial \bar{\bar{\rho}}\tilde{\bar{e}}}{\partial t} + \frac{\partial \bar{\bar{\rho}}\tilde{\bar{u}}_j \tilde{\bar{e}}}{\partial x_j} = -p\frac{\partial \tilde{\bar{u}}_j}{\partial x_j} + \tilde{\bar{\sigma}}_{ij}\frac{\partial \tilde{\bar{u}}_i}{\partial x_j} + \frac{\partial \tau_{e\_j}}{\partial x_j} + \frac{\partial}{\partial x_j}\left(K_t \frac{\partial \tilde{\bar{T}}}{\partial x_j}\right) + \frac{\partial}{\partial x_j}\left(\tilde{\bar{\rho}} D_t \sum_m \tilde{\bar{h}}_m \left(\frac{\partial \tilde{\bar{Y}}_m}{\partial x_j}\right)\right) + S \tag{136}$$

where

$$\tau_{e,j} = \bar{\bar{\rho}}\left(\widetilde{\tilde{u}_j \tilde{e}} - \tilde{\bar{u}}_j \tilde{\bar{e}}\right) \tag{137}$$

is the RANS sub-grid energy closure term that should be modeled if the mesh resolution is too coarse.

As is the case with energy and momentum, the small scales present in a turbulent field act to wrinkle the species fields. This wrinkling increases the surface area of disparate species regions. The increase in surface area results in an increase in mixing via molecular diffusion. It is important to note that this increase in surface area and the associated molecular diffusion is solely responsible for the increased mixing of species in a turbulent flow. The RANS species fields can be decomposed into a sub-grid and resolved field as

$$\tilde{Y}_m = \tilde{\bar{Y}}_m + \tilde{Y}_m'' \tag{138}$$

Using this decomposition, the resolved species equation is given as

$$\frac{\partial \bar{\bar{\rho}} \tilde{\bar{Y}}_m}{\partial t} + \frac{\partial \bar{\bar{\rho}} \tilde{\bar{u}}_j \tilde{\bar{Y}}_m}{\partial x_j} = \frac{\partial}{\partial x_j}\left(\bar{\bar{\rho}} D_t \frac{\partial \tilde{\bar{Y}}_m}{\partial x_j}\right) + \tilde{\bar{\dot{\omega}}} + \frac{\partial \tau_{Y,j}}{\partial x_j} \tag{139}$$

where

$$\tau_{Y,j} = \bar{\bar{\rho}}\left(\widetilde{\tilde{u}_j \tilde{Y}_m} - \tilde{\bar{u}}_j \tilde{\bar{Y}}_m\right) \tag{140}$$

Equation above is the RANS sub-grid species closure term that should be modeled if the mesh resolution is too coarse. The following two quations are the chemical source terms given as

$$\widetilde{\dot{\omega}\left(Y_m, T\right)} = \widetilde{\dot{\omega}_m\left(\hat{Y}_m, \hat{T}\right)} = \widetilde{\dot{\omega}_m\left(Y_m, T\right)}? \tag{141}$$

$$\widetilde{\dot{\omega}_m\left(Y_m,T\right)} \approx \dot{\omega}_m\left(\tilde{Y}_m,\tilde{T}\right)? \tag{142}$$

A question that commonly arises is the commutation of the spatial filtering operation and the ensemble averaging. For a well resolved field (Eq. (141)) the filtering operation will commute if the sub-grid term is small. If the sub-grid term is small, the resolved RANS field is equal to the actual RANS field. For a coarse field, the filtering will not commute. Similarly, the ensemble averaging operation (Eq. (142)) will commute if the fluctuating terms are small and it will not commute if the fluctuating terms are large. This error will be addressed in more detail later in the paper. The use of turbulent diffusion coefficients significantly increases the size of the smallest scales present in the simulation (typically 0.1 mm to 2.0 mm for an engine simulation). With a RANS turbulence model, increasing the grid resolution beyond these RANS smallest scales will not result in more scales being resolved and is therefore unnecessary. However, if the RANS field is under-resolved, additional sub-models may be required (typical of traditional engine simulations). If the flow field is well resolved, no additional model is required for enhanced mixing.

There are only two phenomena that govern combustion: mixing (transport of species, energy, and momentum) and chemical reactions. In the case of non-premixed turbulent combustion, the fuel and oxidizer are not mixed prior to the combustion event. This type of combustion is typical of a diesel engine. For non-premixed combustion, the mixing of the fuel and oxidizer is usually the key phenomenon that governs most of the combustion event (i.e., the mixing time is typically larger than the chemical time).

As shown before, a RANS turbulence model accounts for the enhanced mixing of a turbulent field. It will be shown that if a RANS field is under-resolved there are significant sub-grid terms that must be modeled. However, if a RANS turbulence model is used and the scales are

well resolved no additional sub-models are required to account for the turbulent mixing. The enhanced mixing has already been accounted for in the turbulent viscosity (μ_t), turbulent diffusivity (D_t), and turbulent conductivity (K_t). Any additional models to account for mixing for a well-resolved RANS field would be double counting the effects of turbulence. As discussed above, traditional engine simulations are usually under-resolved (even for a RANS simulation) and the effects of the sub-grid need to be modeled. The effect of sub-grid on non-premixed combustion can be nicely evaluated in mixture fraction space. For this work, the mixture fraction will be defined as

$$Z = \frac{m_{fuel}}{m_{fuel} + m_{air}} \tag{143}$$

Since we are using a RANS turbulence model, the transformation to mixture fraction space will start with the Reynolds averaged modeled species equation. It is important to understand by using a RANS model we have accepted the assumption that the enhanced mixing due to turbulence is accounted for in the RANS equations via the model. If we start the analysis from the un-averaged equations we have implicitly rejected the RANS assumptions. If this assumption is rejected than a RANS framework should not be used for building combustion sub-models. The RANS species equation (139) can be written in mixture fraction space as

$$\bar{\rho}\frac{\partial \tilde{\psi}}{\partial t} = \bar{\rho} D_t \frac{\partial \tilde{Z}}{\partial x_k}\frac{\partial \tilde{Z}}{\partial x_k}\frac{\partial^2 \tilde{\psi}}{\partial \tilde{Z}^2} + \tilde{\dot{\omega}}_m \tag{144}$$

where ψ is the species mass fraction in mixture fraction space. Equation (144) is the well known RANS unsteady flamelet equation. Equation (144) can be further simplified by defining a RANS scalar dissipation rate given by

$$\tilde{\chi} = 2D_t \frac{\partial \tilde{Z}}{\partial x_k} \frac{\partial \tilde{Z}}{\partial x_k} \tag{145}$$

Equation (145) can be substituted into the RANS flamelet equation (Eq. (144)) yielding the typical form of the RANS flamelet equation,

$$\overline{\rho} \frac{\partial \tilde{\psi}_m}{\partial t} = \overline{\rho} \frac{\tilde{\chi}}{2} \frac{\partial^2 \tilde{\psi}_m}{\partial Z^2} + \tilde{\dot{\omega}}_m \tag{146}$$

where the first term at the right hand side in Eq. (146) is the mixing related term, the $\tilde{\dot{\omega}}_m$ is the chemical source term. This form of the species transport equation is convenient for examining the effects of grid resolution on both mixing and chemical reactions. It is important to note that the only assumptions needed to derive the above equation are the original RANS assumptions and the mixture fraction assumption. With these assumptions, the species equation can be rewritten in mixture fraction space. It also is important to note that the mixing term in Eq. (146) does not need to be modeled if all of the scales are resolved. The flamelet equation is simply a transformation of the RANS species equation into mixture fraction space. However, if all of the scales are not resolved, sub-grid models need to be included.

To examine the effect of grid resolution, the mixture fraction can be decomposed into a resolved and sub-grid RANS field as

$$\tilde{Z} = \tilde{\hat{Z}} + \tilde{Z}'' \tag{147}$$

Substituting Eq. (61) into Eq (59) yields

$$\tilde{\chi} = 2D_t \left(\frac{\partial \tilde{\hat{Z}}}{\partial x_k} \frac{\partial \tilde{\hat{Z}}}{\partial x_k} + 2 \frac{\partial \tilde{Z}''}{\partial x_k} \frac{\partial \tilde{\hat{Z}}}{\partial x_k} + \frac{\partial \tilde{\hat{Z}}''}{\partial x_k} \frac{\partial \tilde{\hat{Z}}''}{\partial x_k} \right) \tag{148}$$

It is instructive to examine Eq. (146) in terms of an under-resolved field and a well resolved field. For an under-resolved simulation, the resolved field gradient of the mixture fraction will tend to be under-predicted (i.e., the sub-grid terms are significant). For a well resolved field, the resolved gradient of mixture fraction is accurate (i.e., the sub-grid terms are not significant). Thus, in general for an under-resolved field the actual RANS scalar dissipation is larger than the RANS resolved scalar dissipation:

$$\tilde{\chi} > 2D_t \frac{\partial \tilde{\bar{Z}}}{\partial x_k} \frac{\partial \tilde{\bar{Z}}}{\partial x_k}, (under-resolved) \tag{149}$$

and for a well-resolved field the actual RANS scalar dissipation is equal to the resolved field RANS scalar dissipation:

$$\tilde{\chi} = 2D_t \frac{\partial \tilde{\bar{Z}}}{\partial x_k} \frac{\partial \tilde{\bar{Z}}}{\partial x_k} = 2D_t \frac{\partial \tilde{Z}}{\partial x_k} \frac{\partial \tilde{Z}}{\partial x_k}, (resolved) \tag{150}$$

If only the resolved field were used to calculate the scalar dissipation for an under-resolved simulation, the calculated scalar dissipation would in general be too low. This underestimating of the scalar dissipation would in general lead to combustion that underestimates the effects of the mixing term. This can be understood in the following example. Consider a case where the mixture fraction in a cell is 0.063 (stoichiometric) which is progressing to products and we want to calculate the rate of change of carbon dioxide. This would be governed by the following flamelet equation:

$$\bar{\rho} \frac{\partial \tilde{\psi}_{CO2}}{\partial t} = \bar{\rho} \frac{\tilde{\chi}}{2} \frac{\partial^2 \tilde{\psi}_{CO2}}{\partial Z^2} + \tilde{\dot{\omega}}_{CO2} \tag{151}$$

In Eq. (151) above, as combustion proceeds towards products, the chemical source term $\tilde{\dot{\omega}}_{CO2}$ is positive and $\partial^2 \tilde{\psi}_{CO2} / \partial Z^2$ is negative (see Fig. 1) for a mixture fraction of 0.062. Figure 1

presents the rate of the change of CO_2 versus mixture fraction Z for three scalar dissipation $\tilde{\chi}$ from 10 to 1000. The case with $\tilde{\chi} = 10$ represents the under-resolved case, while the one with 1000 being the resolved case. Thus, clearly as the scalar dissipation is increased the rate of change of carbon dioxide is decreased. Under-resolving the scalar dissipation would result in that combustion is too fast. Conversely, for a mixture fraction of 0.1, under-resolving the scalar would result in that combustion is too slow.

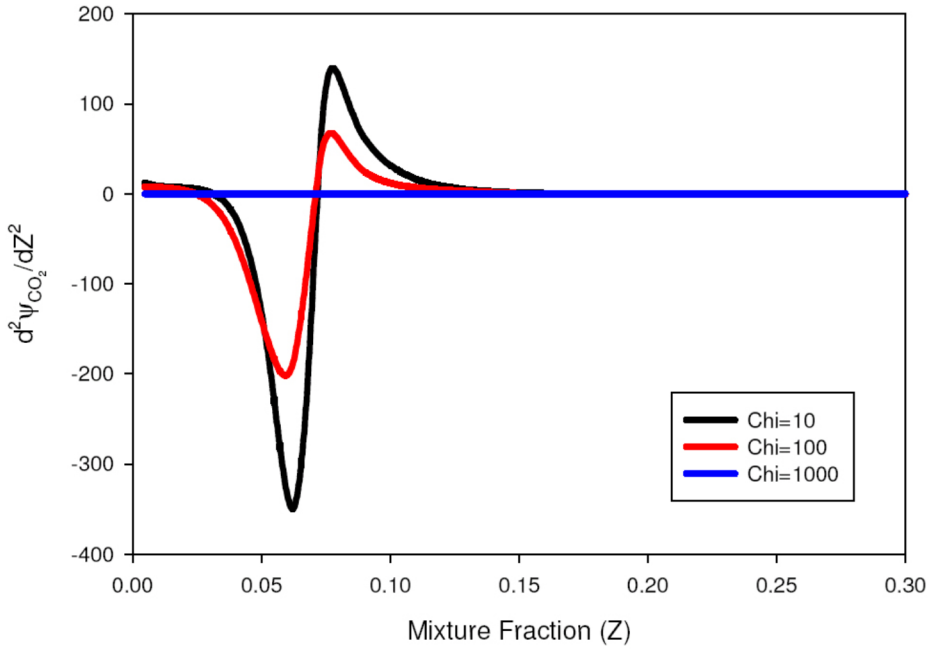

Figure 1. Plot of the second derivative of CO_2 mass fraction in mixture fraction space for n-heptane.

A common model for the scalar dissipation rate is given as:

$$\tilde{\chi} \approx c_\chi \widetilde{Z''^2} \frac{\varepsilon}{k} \tag{152}$$

A significant problem with this type of model is that the scalar dissipation should be modeled as a sub-grid term that diminishes with increased resolution. However, the modeled terms

do not diminish or vanish for a well resolved field. If a RANS field is well resolved the sub-grid terms are negligible but the turbulent terms are not negligible. In the case of a well resolved field, the model would incorrectly predict a significant term. A second problem with this type of model is that for an under-resolved field, the RANS terms (k and ε) have not converged. Thus, with increasing resolution the modeled scalar dissipation will change. These two modeling issues will require tuning of the model constants from case to case.

Any simulation that requires modeling the sub-grid terms of Eq. (148) should be viewed with some skepticism as this an indication that the simulation is under-resolved.

In order to determine the grid resolution where the sub-grid terms are significant, a grid convergence study can be undertaken. Non-premixed combustion simulations can be run with differing grid resolutions. When the combustion results no longer change significantly with increasing grid resolution, the case can be considered grid convergent. At this point, it is evident that the sub-grid terms are small.

Appendix C. Mach number sample calculation

For the base case, 1000K ambient temperature, injection pressure 150MPa,

Assuming density to be 780kg/m^3. From velocity estimation:

$$u = \sqrt{2\frac{\Delta p}{\rho}} \tag{153}$$

The peak injection velocity is about 620m/s.

At 1000K ambient temperature, the speed of sound in dry air is

$$c = \sqrt{\frac{\gamma RT}{M}} \tag{154}$$

where

$\frac{R}{M} = 28$ J/kg/K , $\gamma = 1.4$,

$c = 634$ m/s

Mach number $M = u / c = 620 / 634 < 1$

Hence it is not in supersonic flow region.

Take constant volume reactor as example. Consider

$$c = \sqrt{\frac{\gamma RT}{M}} = \sqrt{\frac{\gamma p}{\rho}} \tag{155}$$

Then Mach number in a cell is

$$M = \frac{u}{c} = \frac{u}{\sqrt{\gamma p / \rho}} \tag{156}$$

where u is velocity magnitude, γ is taken as 1.4. p and ρ are cell pressure and density.

Fig. 2 presents the Mach number versus velocity magnitude for two cases, (a) 1000K and (b) 1300K. For both the case, the Mach number is below 1. Also notice, as temperature is increased, the Mach number is decreased.

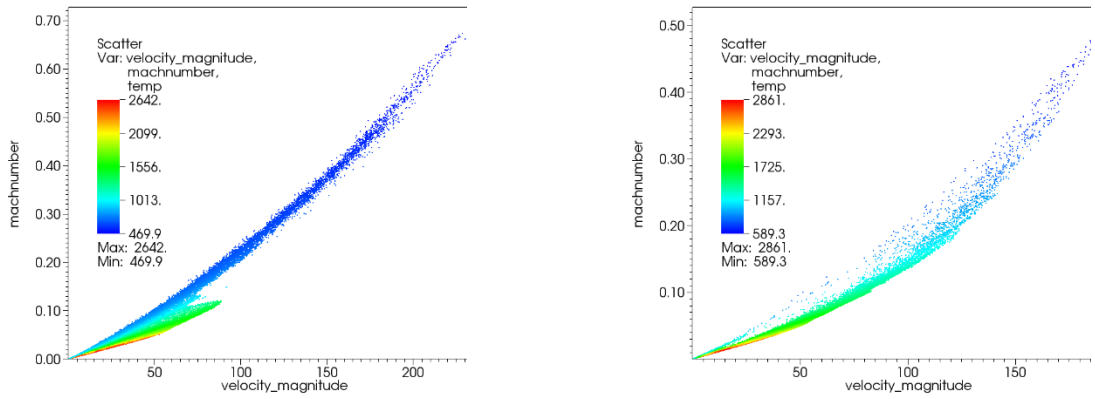

(a) (b)

Figure 2: Mach number vs velocity magnitude of each computational cell as dots for initial T = 1000K at 0.6ms (a) and T = 1300K at 1.5ms (b). The color indicates the temperature from minimum temperature to maximum temperature for each case.

Appendix D. Permission from Journal Publisher

1. Energy and Fuel, ACS Thesis/Dissertation Policy and the ACS Journal Publishing Agreement:

"Reuse/Republication of the Entire Work in Theses or Collections: Authors may reuse all or part of the Submitted, Accepted or Published Work in a thesis or dissertation that the author writes and is required to submit to satisfy the criteria of degree-granting institutions. Such reuse is permitted subject to the ACS' "Ethical Guidelines to Publication of Chemical Research" (http://pubs.acs.org/page/policy/ethics/index.html); the author should secure written confirmation (via letter or email) from the respective ACS journal editor(s) to avoid potential conflicts with journal prior publication*/embargo policies. Appropriate citation of the Published Work must be made. If the thesis or dissertation to be published is in electronic format, a direct link to the Published Work must also be included using the ACS Articles on Request author-directed link − see http://pubs.acs.org/page/policy/articlesonrequest/index.html"

2. Fuel, ELSEVIER Copyright Permissions

"As a general rule, permission should be sought from the rights holder to reproduce any substantial part of a copyrighted work. This includes any text, illustrations, charts, tables,

photographs, or other material from previously published sources. Obtaining permission to re-use content published by Elsevier is simple. Follow the guide below for a quick and easy route to permission.

Can I include/use my article in my thesis/dissertation?

Yes. Authors can include their articles in full or in part in a thesis or dissertation for non-commercial purposes."

10 VITA

Name: Xiao Fu

Education: B.A., Automotive Engineering, Tsinghua University, Beijing, China, 2008

Ph.D., Mechanical Engineering, University of Illinois at Chicago, Chicago, Illinois, 2015

Professional Membership:

American Institute of Aeronautics and Astronautics

The Combustion Institute

Publications: Xiao Fu, Stephen Garner, Suresh Aggarwal, Kenneth Brezinsky, "Numerical Study of NOx Emissions from n-Heptane and 1-Heptene Counterflow Flames", Energy & Fuels, 26(2), 01/2012, 879-888.

Xiao Fu, Xu Han, Kenneth Brezinsky, and Suresh Aggarwal, "Effect of Fuel Molecular Structure and Premixing on Soot Emissions from n-Heptane and 1-Heptene Flames", Energy & Fuels, 27(10), 09/2013, 6262-6272.

Suresh K. Aggarwal, Xiao Fu, Sameera Wijeyakulasuriya, "Effects of Fuel Reactivity and Injection Timing on Diesel Engine Combustion and Emissions" International Journal of Green Energy, 10/2014.

Xiao Fu, Suresh Aggarwal, "Two-stage ignition and NTC phenomenon in diesel engines", Fuel, 144, 2015, 188-196.

Xiao Fu, Suresh Aggarwal, "Fuel unsaturation effects on NOx and PAH formation in spray flames", Fuel, 160, 2015, 1-15.

Conference: Xiao Fu, Suresh Aggarwal, Kenneth Brezinsky, Stephen Garner, "Study of Acetylene and NO Emissions from N-heptane and 1-heptene Counterflow Flames", The 7th International Conference on Chemical Kinetics, US. 07/2011.

Xiao Fu, Kenneth Brezinsky and Suresh Aggarwal, "NOx and PAH Emissions from n-Heptane and 1-Heptene Partially Premixed Flames", 50th AIAA Aerospace Sciences Meeting including the New Horizons Forum and Aerospace Exposition, US, 01/2012.

Xiao Fu, Kenneth Brezinsky, Suresh Aggarwal, 'Effect of Strain and Partial Premixing on NOx and PAH Emissions in n-Heptane and 1-Heptene Flames", Spring Technical Meeting of the Central States Section of the Combustion Institute, 04/2012.

Xiao Fu, Xu Han, Suresh Aggarwal, "Effect of Unsaturated Bond on PAH and Soot Formation in n-Heptane and 1-Heptene Partially Premixed Flames" 8th U. S. National Combustion Meeting Organized by the Western States Section of the Combustion Institute, US, 05/2013.

Xiao Fu and Suresh Aggarwal, "Two-Stage Ignition and NTC Phenomenon in a Dual Fuel Diesel Engine", Spring Technical Meeting of the Central States Section of the Combustion Institute, US. 03/2014.

Xiao Fu and Suresh Aggarwal, "Fuel Unsaturation Effects on NOx and PAH Formation in Spray Flames" 9th U. S. National Combustion Meeting Organized by the Central States Section of the Combustion Institute, US. 05/2015.